



AMERICAN UNIVERSITY OF BEIRUT

CO-ADSORPTION OF COMPLEMENTARY PYRIDYL AND  
CARBOXYLIC ACID BASED DYES IN DYE-SENSITIZED  
SOLAR CELLS

by  
MELISSA ANTOINE EL BITAR NEHME

A thesis  
submitted in partial fulfillment of the requirements  
for the degree of Master of Science  
to the Department of Chemistry  
of the Faculty of Arts and Sciences  
at the American University of Beirut

Beirut, Lebanon  
March, 2019

AMERICAN UNIVERSITY OF BEIRUT


CO-ADSORPTION OF COMPLEMENTARY PYRIDYL AND  
CARBOXYLIC ACID BASED DYES IN DYE-SENSITIZED  
SOLAR CELLS

by  
MELISSA ANTOINE EL BITAR NEHME

Approved by:

---

Dr. Tarek Ghaddar, Professor  
Department of Chemistry

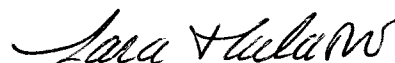


Advisor

---

Dr. Lara Halaoui, Professor  
Department of Chemistry

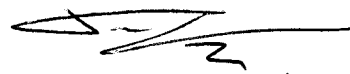
Member of Committee



---

Dr. Pierre Karam, Assistant Professor  
Department of Chemistry

Member of Committee



Date of thesis defense: March 20, 2019

# AMERICAN UNIVERSITY OF BEIRUT

## THESIS, DISSERTATION, PROJECT RELEASE FORM

Student Name:

El Bitar Nehme                      Melissa                      \_\_\_\_\_  
Last    First    Middle

Master's Thesis                       Master's Project                       Doctoral Dissertation

I authorize the American University of Beirut to: (a) reproduce hard or electronic copies of my thesis, dissertation, or project; (b) include such copies in the archives and digital repositories of the University; and (c) make freely available such copies to third parties for research or educational purposes.

I authorize the American University of Beirut, to: (a) reproduce hard or electronic copies of it; (b) include such copies in the archives and digital repositories of the University; and (c) make freely available such copies to third parties for research or educational purposes

after : **One ---- year from the date of submission of my thesis, dissertation, or project.**

**Two ---- years from the date of submission of my thesis, dissertation, or project.**

**Three----years from the date of submission of my thesis, dissertation, or project.**

Signature Melissa N.

Date 29/03/2019

## ACKNOWLEDGMENTS

First and foremost, I would like to sincerely thank my thesis advisor Prof. Tarek Ghaddar for his patience, motivation, and enthusiasm throughout my research work at AUB. The door to Prof. Ghaddar's office was always open for questions and inquiries, and even though he constantly allowed this thesis to be my own work, he made sure to steer me in the right direction when he thought I needed it. Thank you for introducing me to the beautiful world of Dye-Sensitized Solar Cells.

I would also like to thank my committee members, Prof. Lara Halaoui and Dr. Pierre Karam, for their insightful comments, encouragement, and hard questions.

A special thank you goes out to my fellow lab mates and friends at AUB. I will never forget our stimulating discussions, the panic-induced nights we had before any deadlines, and our shenanigans in the Graduate Room. A special thanks goes out to my best friend Lea Njeim for tolerating me, supporting me, and always being there for me.

Furthermore, I must also express my profound gratitude to my parents for providing me with unfailing support, unconditional love, and irrevocable affection. This thesis would not have been possible without them. I am forever grateful for their love.

To my wonderful twin sister, Vanessa. Thank you for letting me be me, and for always being there to catch me if I fall. I am nothing without you, and will always be there for you should you ever need me. I wouldn't be here if it wasn't for you.

## AN ABSTRACT OF THE THESIS OF

Melissa Antoine El Bitar Nehme for Master of Science  
Major: Chemistry

Title: Co-adsorption of Complementary Pyridyl and Carboxylic Acid Based Dyes in Dye-Sensitized Solar Cells

The harnessing of sunlight to convert it to electrical energy is the basic idea of a solar cell, and has been a subject of interest to scientists for decades. One of the so-called third generation solar cells, is what is commonly known as the dye sensitized solar cell (DSSC), is based on a thin film of mesoporous TiO<sub>2</sub> that is sensitized with either an organic or inorganic dye.

Our line of research has focused mainly on the synthesis of dyes and the study of the structure-function relationship and their effects on the DSSC's efficiency. Many attempts were made to improve the performance of organic based DSSCs, by either changing the anchoring group of the dye, the dye molecular structure (such as with different middle electron-acceptor groups), electrolyte system, counter electrode, etc.

We are currently working on the synthesis of three novel organic dyes of the form donor- $\pi$ -acceptor- $\pi$ - with a pyridine moiety as the terminal anchoring group. The middle acceptor group will be varied, in order to shift the dyes' absorption more towards the red depending on its electron-accepting ability and hence increase their light harvesting efficiencies. In addition, we will study the effect of co-sensitization of the above mentioned dyes with complementary carboxylic-acid based ones, where both classes of dyes adsorb at different sites of titania, in order to enhance the overall efficiencies of the cells in particular the photo-current.

# CONTENTS

ACKNOWLEDGEMENTS.....	v
ABSTRACT.....	vi
LIST OF ILLUSTRATIONS.....	xi
LIST OF TABLES.....	xv

## Chapter

1. INTRODUCTION.....	1
1.1. Solar Energy, Solar Cells, and Photovoltaics .....	1
1.2. Dye-Sensitized Solar Cells .....	3
1.2.1. Brief Overview.....	3
1.2.2. Structure and Operation Principle .....	4
1.2.3. Electron Transfer Process.....	7
1.3. Key Parameters for DSSC Performance.....	10
1.3.1. Incident Photon to Current Conversion Efficiency (IPCE).....	10
1.3.2. Open-Circuit Photovoltage ( $V_{OC}$ ) .....	11
1.3.3. Short-Circuit Photocurrent ( $J_{SC}$ ) .....	12
1.3.4. Fill Factor (FF).....	12

1.3.5. Overall Power Conversion Efficiency ( $\eta$ ) .....	13
1.3.6. Electrochemical Impedance Spectroscopy (EIS).....	13
1.4. Basic Components of a DSSC .....	15
1.4.1. The Mesoporous Titanium Dioxide Semiconductor .....	15
1.4.2. The Electrolyte System .....	17
1.4.2.1.Redox Mediators.....	17
1.4.2.2.Organic Solvent .....	20
1.4.2.3.Additives and Cations .....	22
1.4.3. The Counter Electrode .....	24
1.4.4. The Dye Sensitizer .....	25
1.4.4.1.Anchoring Groups and Sites .....	29
1.5.Co-adsorption of Nitrogen-Containing Organic Dyes .....	33
1.5.1. Literature Review .....	33
1.6.Objective of Work .....	38
<b>2. EXPERIMENTAL MATERIALS AND INSTRUMENTATION .....</b>	<b>39</b>
2.1. Materials .....	39
2.2. Instrumentation.....	39
2.3. Computational Methods.....	40
2.4. Solar Cell Fabrication .....	40
2.5.Synthesis of Three Novel Dyes .....	41
2.5.1. Preparation of T200.....	41
2.5.1.1. Synthesis of 4,7-dithien-2-yl-2,1,3-benzothiadiazole .....	41
2.5.1.2.Synthesis of 4,4'-dihydroxybenzil .....	42
2.5.1.3.Synthesis of 4,4'-diethylhexylbenzil.....	42
2.5.1.4.Synthesis of 2,3-bis[4-[(2-ethylhexyl)oxy]phenyl]-5,8-di- 2-thienyl-quinoxaline.....	43



2.5.1.5.Synthesis of 5,8-bis(5-bromo-2-thienyl)-2,3-bis[4-[(2-ethylhexyl)oxy]phenyl]-quinoxaline .....	44
2.5.1.6.Synthesis of T200 .....	44
2.5.2. Preparation of T201 .....	45
2.5.2.1.Synthesis of 3,6-Di(thiophen-2-yl)pyridazine .....	45
2.5.2.2. Synthesis of 3,6-Bis(5-bromo-2-thienyl)pyridazine .....	46
2.5.2.3.Synthesis of T201 .....	46
2.5.3. Preparation of T202.....	47
2.5.3.1.Synthesis of 4,7-Bis(2-bromo-5-thienyl)-2,1,3-benzothiadiazole .....	47
2.5.3.2.Synthesis of T202 .....	48
<b>3. RESULTS AND DISCUSSION .....</b>	<b>50</b>
3.1.Synthesis and Characterization of Dyes .....	50
3.2. Characterization and Cell Assembly .....	56
3.2.1. Optical and Electrochemical Properties .....	56
3.2.2. Computational Methods .....	62
3.3. Photovoltaic Performance and IPCE Spectra.....	68
3.3.1. Individual Dyes.....	68
3.4. Co-adsorption of Complementary Dyes .....	70
3.4.1. Co-sensitization of T202 with DB and YD2 .....	70
3.4.1.1.Dye Loading Measurements .....	71
3.4.1.2.Effect of Dye Size on Co-adsorption.....	75
3.4.2. Co-sensitization of T201 with Ruthenium (II) Dyes.....	78
3.4.2.1.Dye Loading Measurements .....	81
3.4.2.2.Sequential Deposition vs One-Step Co-adsorption Method .....	87
3.4.3. Photovoltaic Performance and IPCE Spectra .....	89
3.4.3.1.Co-adsorption of T202 with DB and YD2 .....	89
3.4.3.2.Co-adsorption of T201 with N719 .....	93
3.4.4. Electrochemical Impedance Spectroscopy .....	96
3.4.4.1.Measurements for Co-adsorption of T202 with YD2 versus DB.....	97

3.4.4.2. Measurements for Co-adsorption of T201 with N719 .....	102
4. CONCLUSION .....	105
5. SUPPORTING INFORMATION.....	107
6. REFERENCES .....	121

## ILLUSTRATIONS

Figure		Page
1.	Schematic diagram of a dye-sensitized solar cell.....	5
2.	Electron transfer process of a DSSC with a liquid electrolyte via energy levels.....	7
3.	Typical timescale for the various electron transfer processes in a DSSC.....	10
4.	Typical Nyquist plot with their equivalent circuits of a DSC.....	14
5.	Binding modes for carboxylic acids and amines on the metal oxide.....	31
6.	The absorbance spectra of T200, T201, and T202 dyes in THF.....	57
7.	The emission spectra of T200, T201, and T202 dyes recorded in THF.....	59
8.	Differential pulse voltammograms of T200, T201, and T202 in DMF in 0.1 M TBAPF <sub>6</sub> recorded at a scan rate of 100 mV.s <sup>-1</sup> .....	61
9.	The frontier molecular orbital energies of the dyes T200, T201, and T202 .....	64
10.	Isodensity plots of the frontier orbitals of the dyes T200, T201, and T202.....	65
11.	Photocurrent–voltage characteristics of DSSCs sensitized with T200, T201, and T202, and the corresponding dark currents.....	68
12.	IPCE % spectra of DSSCs sensitized with T200, T201, and T202...	69
13.	The absorbance spectra of T202, YD2, and T202-YD2 on TiO <sub>2</sub> films.....	71
14.	The absorbance spectra of TiO <sub>2</sub> desorbed films of YD2, YD2-T202, and T202 as a function of wavelength.....	72
15.	The absorbance spectra of T202, DB, and T202-DB on TiO <sub>2</sub> films.....	73
16.	The absorbance spectra of TiO <sub>2</sub> desorbed films of DB, DB-T202, and T202 as a function of wavelength.....	74

17.	The absorbance spectra of a)T201, T169, and T201-T169 b) T201, T65, and T201-T65 c) T201, T135, and T201-T135 d) T201, N719, and T201-N719 on TiO <sub>2</sub> films.....	83
18.	The absorbance spectra of TiO <sub>2</sub> desorbed films of a)T201, T169, and T201-T169 b) T201, T65, and T201-T65 c) T201, T135, and T201-T135 d) T201, N719, and T201-N719 as a function of wavelength.....	85
19.	The absorbance spectra of a)T201 deposition followed by T65 b) T65 deposition followed by T201 on TiO <sub>2</sub> films.....	88
20.	(a) Photocurrent-voltage characteristics under 1000 W m <sup>-2</sup> AM1.5 G illumination of DSSCs sensitized with T202 and YD2 and co-sensitized with T202-YD2 (lines) and in darkness (dotted lines); (b) Corresponding IPCE % spectra.....	90
21.	(a) Photocurrent-voltage characteristics under 1000 W m <sup>-2</sup> AM1.5 G illumination of DSSCs sensitized with T202 and DB and co-sensitized with T202-DB (lines) and in darkness (dotted lines); (b) Corresponding IPCE % spectra.....	92
22.	(a) Photocurrent-voltage characteristics under 1000 W m <sup>-2</sup> AM1.5 G illumination of DSSCs sensitized with T201 and N719 and co-sensitized with T201-N719 (lines) and in darkness (dotted lines); (b) Corresponding IPCE % spectra.....	95
23.	Charge transfer resistance values extracted from EIS measurements of T202, YD2, and co-sensitized T202-YD2 DSSCs.....	97
24.	Chemical capacitance values extracted from EIS measurements of T202, YD2, and co-sensitized T202-YD2 DSSCs.....	98
25.	Electron lifetime values extracted from EIS Measurements of T202, YD2, and co-sensitized T202-YD2 DSSCs.....	98
26.	Charge transfer resistance values extracted from EIS measurements of T202, DB, and co-sensitized T202-DB DSSCs.....	100
27.	Chemical capacitance values extracted from EIS measurements of T202, DB, and co-sensitized T202-DB DSSCs.....	101
28.	Electron lifetime values extracted from EIS measurements of T202, DB, and co-sensitized T202-DB DSSCs.....	101
29.	Charge transfer resistance values extracted from EIS measurements of T201, N719, and co-sensitized T201-N719 DSSCs.....	103

30.	Chemical capacitance values extracted from EIS measurements of T201, N719, and co-sensitized T201-N719 DSSCs.....	103
31.	Electron lifetime values Extracted from EIS measurements of T201, N719, and co-sensitized T201-N719 DSSCs.....	104
32S.	<sup>1</sup> HNMR of 4,7-dithien-2-yl-2,1,3-benzothiadiazole in CDCl <sub>3</sub> at 500 MHz.....	107
33S.	<sup>1</sup> HNMR of 4,7-Bis(2-bromo-5-thienyl)-2,1,3-benzothiadiazole in DMSO-d <sub>6</sub> at 500 MHz.....	108
34S.	<sup>1</sup> HNMR of 4,4'-dihydroxybenzil in DMSO-d <sub>6</sub> at 500 MHz.....	109
35S.	<sup>1</sup> HNMR of 4,4'-diethylhexylbenzil in CDCl <sub>3</sub> at 500 MHz.....	110
36S.	<sup>1</sup> HNMR of 2,3-bis[4-[(2-ethylhexyl)oxy]phenyl]-5,8-di-2-thienyl-quinoxaline in CDCl <sub>3</sub> at 500 MHz.....	111
37S.	<sup>1</sup> HNMR of 5,8-bis(5-bromo-2-thienyl)-2,3-bis[4-[(2-ethylhexyl)oxy]phenyl]-quinoxaline in CDCl <sub>3</sub> at 500 MHz.....	112
38S.	<sup>1</sup> HNMR of T200 in C <sub>6</sub> D <sub>6</sub> at 500 MHz.....	113
39S.	<sup>1</sup> HNMR of 3,6-Di(thiophen-2-yl)pyridazine in CDCl <sub>3</sub> 500 MHz...	114
40S.	<sup>1</sup> HNMR of 3,6-Bis(5-bromo-2-thienyl)pyridazine in CDCl <sub>3</sub> 500 MHz.....	115
41S.	<sup>1</sup> HNMR of T201 in acetone-d <sub>6</sub> at 500 MHz.....	116
42S.	<sup>1</sup> HNMR of T202 in benzene-d <sub>6</sub> at 500 MHz.....	117
43S.	Mass spectrometry of T200.....	118
44S.	Mass spectrometry of T201.....	119
45S.	Mass spectrometry of T202.....	120

Scheme	Page
1. Molecular structures of N3 and Black Dye .....	4
2. Molecular structures of N719.....	27
3. Molecular structures of D35 and TPA dyes .....	29
4. Molecular structures of YD2- <i>o</i> -C8 .....	32
5. Molecular structures of Y123 .....	35
6. Molecular structures of SAT-1, NI-6, and YNI-2.....	35
7. Molecular structure of YM-2.....	37
8. Molecular structures of JA1, JA2, and TTR2 .....	37
9. Synthetic scheme of T200 where a) 4-pyridinyl boronic acid, C <sub>52</sub> H <sub>66</sub> BNO <sub>2</sub> , PPh <sub>3</sub> , K <sub>2</sub> CO <sub>3</sub> , palladium acetate, dioxane: THF: H <sub>2</sub> O....	53
10. Synthetic scheme of T201 where a) 4-pyridinyl boronic acid, C <sub>52</sub> H <sub>66</sub> BNO <sub>2</sub> , PPh <sub>3</sub> , K <sub>2</sub> CO <sub>3</sub> , palladium acetate, dioxane: THF: H <sub>2</sub> O....	54
11. Synthetic scheme of T202 where a) 4-pyridinyl boronic acid, C <sub>52</sub> H <sub>66</sub> BNO <sub>2</sub> , PPh <sub>3</sub> , K <sub>2</sub> CO <sub>3</sub> , palladium acetate, dioxane: THF: H <sub>2</sub> O....	55
12. The molecular structures of YD2 and DB dyes.....	70
13. Calculated relative sizes of the geometry optimized T202, T181, and DB dyes.....	76
14. Calculated relative sizes of the eometry optimized T202 and YD2 dyes.....	77
15. Molecular structure of Z907 dye.....	79
16. Molecular structures of the chosen Ru (II) dyes .....	80

## TABLES

Table		Page
1.	Optical and electrochemical properties of T200, T201, and T202.....	62
2.	Computed excitation energies, assignments, and oscillator strengths for the dye T200 .....	66
3.	Computed excitation energies, assignments, and oscillator strengths for the dye T201 .....	67
4.	Computed excitation energies, assignments, and oscillator strengths for the dye T202 .....	67
5.	Photovoltaic parameters of T200, T201, and T202.....	69
6.	The dye loading of T202 and YD2 for pure and co-adsorbed TiO <sub>2</sub> films.....	72
7.	The dye loading of T202 and DB for pure and co-adsorbed TiO <sub>2</sub> films.....	74
8.	The dye loading of a) T201 and T169 b) T201 and T65 c) T201 and T135 d) T201 and N719 for pure and co-adsorbed TiO <sub>2</sub> films.....	86
9.	Photovoltaic performance of the T202 and YD2 DSSCs and co-sensitized T202-YD2.....	90
10.	Photovoltaic performance of the T202 and DB DSSCs and co-sensitized T202-DB.....	93
11.	Photovoltaic performance of the T201 and N719 DSSCs and co-sensitized T201-N719.....	95

# CHAPTER I

## INTRODUCTION

### **1.1 Solar energy, solar cells, and photovoltaics**

With the ongoing depletion of fossil fuels, increase in global energy consumption, escalating CO<sub>2</sub> emissions and global warming, attaining a sustainable society by supplying clean, renewable, and environmentally friendly energy resources has been one of the most challenging tasks for scientists in the 21<sup>st</sup> century.<sup>1</sup> Even though conventional energy resources (coal, natural gas, oil etc...) have met energy demands, their rapid exhaustion and non-renewability has provided limitations for future growth in the energy sector.<sup>2</sup> An aid to this dilemma would be shifting to renewable energy resources, which are naturally replenished, and their integration in efficient energy management plans would meet global energy demands.<sup>3</sup> The advantages of the implementation of renewable energy resources vary from a decrease in greenhouse gas emissions and external energy dependence,<sup>4</sup> to minimizing waste and extreme environmental and climate impacts.<sup>2,5</sup> Of the various renewable energy sources, solar energy is considered the most abundant and exploitable resource, producing around 173,000 TW, of which 120,000 TW strike the Earth's surface.<sup>6</sup> Renewable energy technologies aim at converting such resources into usable forms of energy such as electricity and heat.



The harnessing of solar energy and its efficient conversion to electrical power is the core focus of solar photovoltaic systems.<sup>7</sup> French physicist Alexander Becquerel first discovered the photovoltaic effect in 1839 and since then, the field of photovoltaics has been rapidly growing. This phenomenon was applied in 1954, when the first practical solar cell was created at Bell Labs with an efficiency of 6 %.<sup>8</sup> The operation principle of a PV solar cell is based on a semiconductor material that converts the absorbed photons into electron-hole pairs.

The most recognized solar PV technologies are based on silicon, and are known as the first-generation solar cells. With silicon being the second most abundant element in nature, and its availability in large quantities, monocrystalline and polycrystalline silicon solar cells have dominated the PV market so far, reaching a power conversion efficiency of around 25%.<sup>9</sup> However, a large barrier preventing their industrial and commercial application is the expensive materials, high cost of manufacture, and environmental cost.<sup>10</sup> As a consequence, thin-film solar cells have emerged, which cut material and production costs by eliminating the silicon wafers.<sup>11</sup> These second-generation solar cells are based on amorphous silicon, gallium arsenide GaAs, cadmium telluride CdTe, copper indium gallium selenide CIGS, etc.,<sup>12</sup> and like the formerly mentioned cells, are based on single junction devices. Aside from providing a comparable performance to the silicon-based cells, second-generation solar cells are also characterized by flexibility and versatility, which allow their proper tailoring to improve the device performance.<sup>13</sup> Nonetheless, drawbacks such as toxicity and scarce materials have encouraged a further 20 years of research, and thus the development of the third-generation hybrid film solar cells. This third class of solar cells is based on organic, inorganic, and hybrid semiconductors, and examples

include dye-sensitized solar cells, quantum dot solar cells, perovskite solar cells, tandem cells, etc.<sup>14</sup>, which acquire the use of low-cost, abundant, and non-toxic materials.

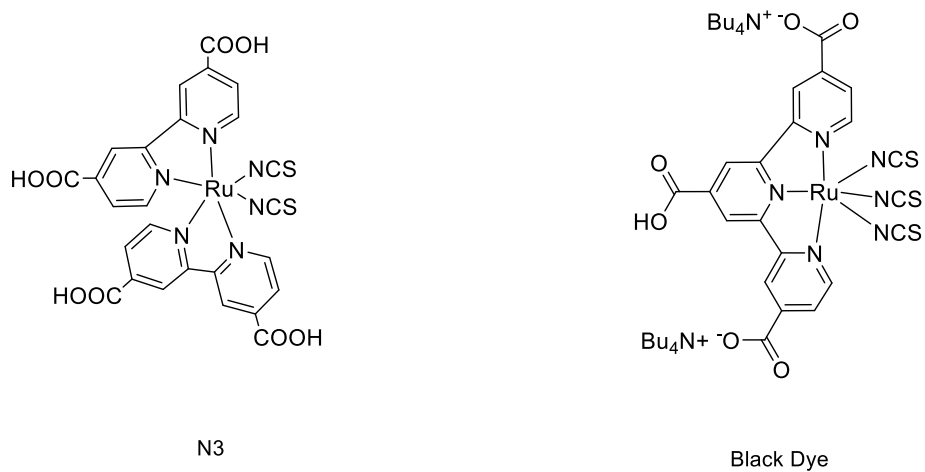
Among the third-generation solar cells, Dye-sensitized solar cells, also known as Grätzel cells, have emerged as promising potential candidates for cost-effective photovoltaic devices, offering attractive selling points such as flexibility, tunable aesthetic properties, environmental benignity, and easy fabrication.<sup>15</sup>

## 1.2 Dye-Sensitized Solar Cells

### 1.2.1 *Brief Overview*

In 1991, Grätzel and O'Regan achieved a breakthrough by the creation of a dye-sensitized titania based solar cell reaching a power conversion efficiency of 7.12% under full sunlight irradiation.<sup>16</sup> This photovoltaic device mimics the photosynthetic process in plants i.e. absorption of photons, however, the processes of light absorption and charge carrier transport are separate.<sup>17</sup> The sensitizer of choice, which constitutes the heart of the DSC and is responsible for photon absorption and charge injection, was a trimeric ruthenium complex  $\text{RuL}_2(\mu\text{-CN})\text{Ru}(\text{CN})(\text{L}')_2$  where  $\text{L} = 2,2'$ -bipyridine-4, 4'-dicarboxylic acid and  $\text{L}' = 2,2'$ -bipyridine.<sup>16</sup> In 1993, a remarkable enhancement in the overall efficiency was observed using the N3 dye as a sensitizer<sup>18</sup> and later on by the introduction of the panchromatic black dye N-749 in 2001 (Scheme 1).<sup>19,20</sup> Due to these encouraging results, industrial interest in DSC has increased, whereby companies have begun manufacturing DSC modules for electronic and residential installations.<sup>21</sup> Recently, a record efficiency of 14%<sup>22</sup> was obtained by Kenji and coworkers by co-sensitizing two

complementary dyes: an alkoxy-silyl anchor dye ADEKA-1 and a carboxy-anchor organic dye LEG4.



**Scheme 1.** Molecular structures of N3 and Black Dye

### 1.2.2 Structure and Operation Principle

A schematic representation of the interior of a conventional liquid DSC is shown in Figure 1. This configuration is a sandwich arrangement of two transparent conducting oxide (TCO) electrodes covered with a conductive indium-doped tin oxide (ITO) or fluoride-doped tin oxide (FTO) layer.<sup>23,24,25,26,27</sup> The working electrode, or the anode, is coated with a mesoporous nanocrystalline semiconductor oxide layer used for electron transfer. Titanium dioxide (TiO<sub>2</sub>) has been the most frequently used material, however, other wide bandgap semiconductors such as ZnO, SnO<sub>2</sub>, and Nb<sub>2</sub>O<sub>5</sub> have also been investigated. Ideally, the film thickness is around 10 μm with a porosity ranging between

50-60%. Adsorbed on the surface of the nanocrystalline film is a monolayer of the sensitizing dye, which harvests the incident light. The counter (TCO) electrode, composed of an ITO or an FTO conductive glass sheet, is coated with a layer of fine platinum nanoparticles, which, aside from catalyzing the redox regeneration reaction, is also useful for electron collection. Between the electrodes resides an organic electrolyte containing a redox mediator, most commonly the iodide/triiodide redox couple, in an organic solvent.

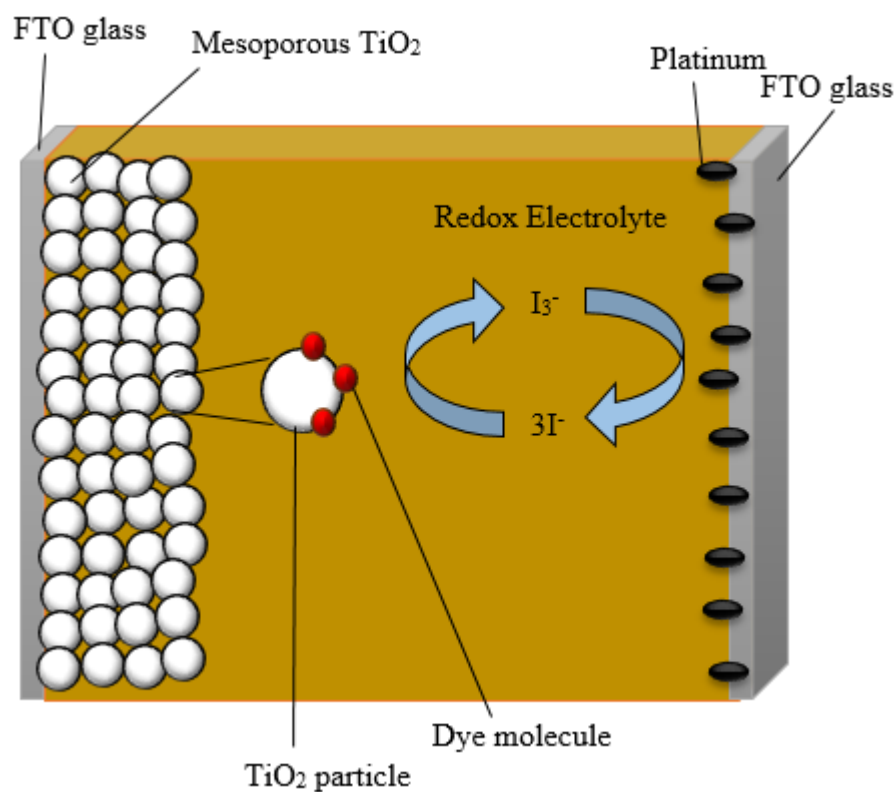


**Figure 1.** Schematic diagram of a dye-sensitized solar cell

The sequence of electron transfer in a DSSC is as follows: the dye molecules (D) absorb visible light once the cell is illuminated, which leads to the formation of an excited state ( $D^*$ ) (eq 1). The excited dye molecules will in turn inject electrons into the conduction band of the semiconductor, which leaves the dye in the oxidized state ( $D^+$ ) (eq 2). The injected electrons travel through the  $TiO_2$  nanoparticles and are transported towards the external circuit. The oxidized sensitizer is regenerated by the iodide in the electrolyte which in turn will get oxidized to  $I_3^-$  (eq 3). The electrons in the external circuit reduce the  $I_3^-$  to  $I^-$ , thus completing the regenerative cycle (eq 4). However, two opposing, detrimental processes might occur simultaneously with the desired reactions, resulting in cell efficiency losses and no photocurrent detection. The reactions include the recombination of the electrons in the  $TiO_2$  semiconductor with the oxidized dye (eq 5), or with the oxidized redox couple (eq 6). A schematic representation is shown in Figure 2.<sup>28,29</sup>



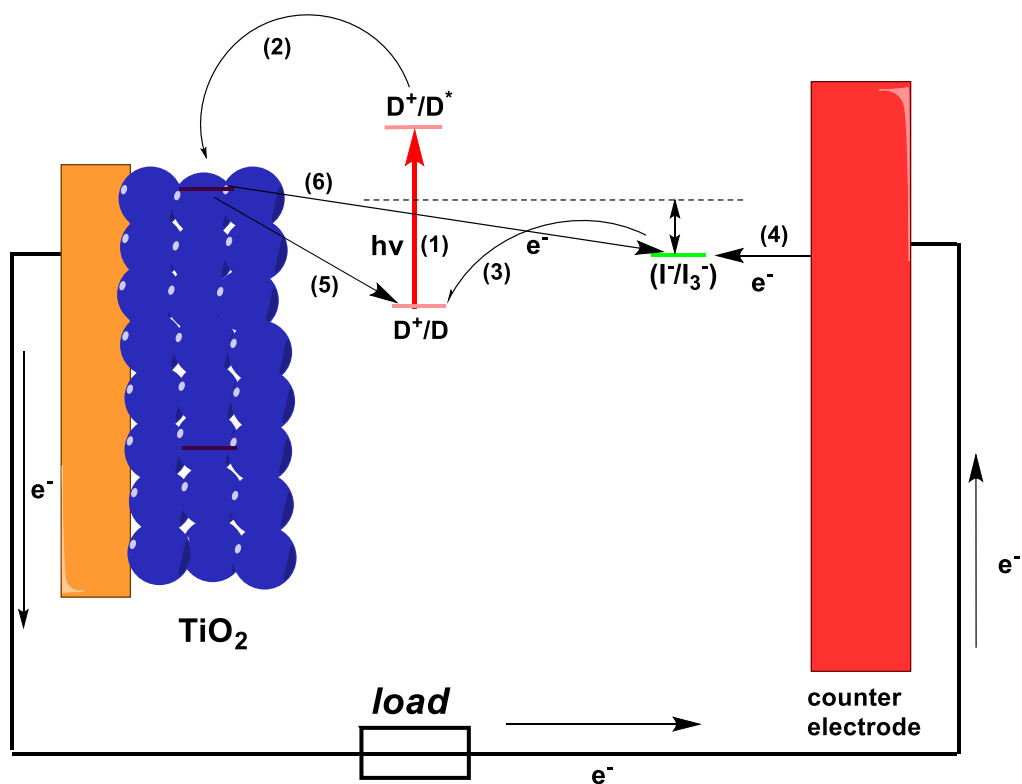


**Figure 2.** Electron transfer process of a DSSC with a liquid electrolyte via energy levels

### 1.2.3 Electron Transfer Process

Because the processes of light absorption, charge transfer, and charge collection are carried out by distinct components in a DSC, the kinetics of the different electron transfer processes taking place at the TiO<sub>2</sub>/dye/electrolyte interface have been closely investigated by various researchers (Figure 3).

In the late '60s, Marcus and Gerischer described the excited state injection of an electron into a wide bandgap semiconductor.<sup>30,31</sup> For an efficient DSC performance, an astoundingly fast electron injection from the excited dye state to the Fermi level of the semiconductor is of superior importance, commonly ranging between the femtosecond and

picosecond scale.<sup>32</sup> In order to achieve these desired results, a strong electronic coupling is required between the LUMO orbital of the dye and the conduction band level of the semiconductor.<sup>29</sup> It is also important to mention that the rate of electron injection process must be compared to the excited state decay to ground state, which usually varies between picoseconds and nanoseconds.<sup>33</sup>

Following the injection process, the electrons will migrate by diffusion inside the mesoporous semiconductor. This transport route involves trapping and de-trapping of electrons,<sup>34</sup> and in turn is dependent on the incident light intensity.<sup>35</sup> The traps that are not involved in electron transport are mainly due to surface/crystal defects such as oxygen vacancies.<sup>36</sup> On the other hand, deep traps involved in the electron transport process are located at the TiO<sub>2</sub>/ electrolyte interface, at the bulk of the semiconductor, or at grain boundaries.<sup>26</sup>

To achieve long-term stability, fast regeneration of the oxidized dye is crucial. This is accomplished when the dye accepts electrons from the redox mediator I<sup>-</sup> present in the electrolyte within microseconds,<sup>26</sup> prior to back electron recombination. Consequently, effective dye regeneration is realized when the oxidation potential of the photosensitizer is more positive than the redox potential of the mediator. In 2013, Hagfeldt and coworkers applied Marcus theory to investigate the regeneration of oxidized dye molecules by cobalt complexes.<sup>37</sup> It was determined that the driving force for regeneration, estimated from the difference between the oxidation potential of the dye and the formal potential of the redox couple, increased with an increase in the regeneration rate constant.<sup>37</sup> The kinetics for dye regeneration is also influenced by the iodide concentration, wherein an impedance in regeneration is observed by using viscous electrolytes.<sup>38</sup> Furthermore, faster regeneration

was observed when the cation of the iodide salt was adequately small such as  $\text{Li}^+$  or  $\text{Mg}^{2+}$  in comparison to bulky tert-butylammonium  $\text{TBA}^+$  ions.<sup>39</sup>

The timescale for the recombination reaction between the hole in the dye HOMO level and the injected electrons in the semiconductor ranges from microseconds to milliseconds, and therefore, competes with the dye regeneration process.<sup>40</sup> This back electron transfer process depends on the sensitizer, whereby a suitable localization of the dye cation HOMO from the metal oxide semiconductor is required to increase the electron barrier for recombination. The time constant for the recombination of the electrons in the mesoporous  $\text{TiO}_2$  with acceptors in the electrolyte is called the electron lifetime,<sup>41</sup> and occurs within a millisecond to second scale. This dark current detrimentally affects the open circuit voltage ( $V_{\text{OC}}$ ) of the photovoltaic solar cell and occurs at regions where no dye has adsorbed on the  $\text{TiO}_2$ /electrolyte interface.<sup>29</sup> In 2009, Li *et al.* employed organic and inorganic blocking layers to suppress the electron leakage current, which in turn resulted in a two-fold increase in the open circuit voltage.<sup>42</sup>



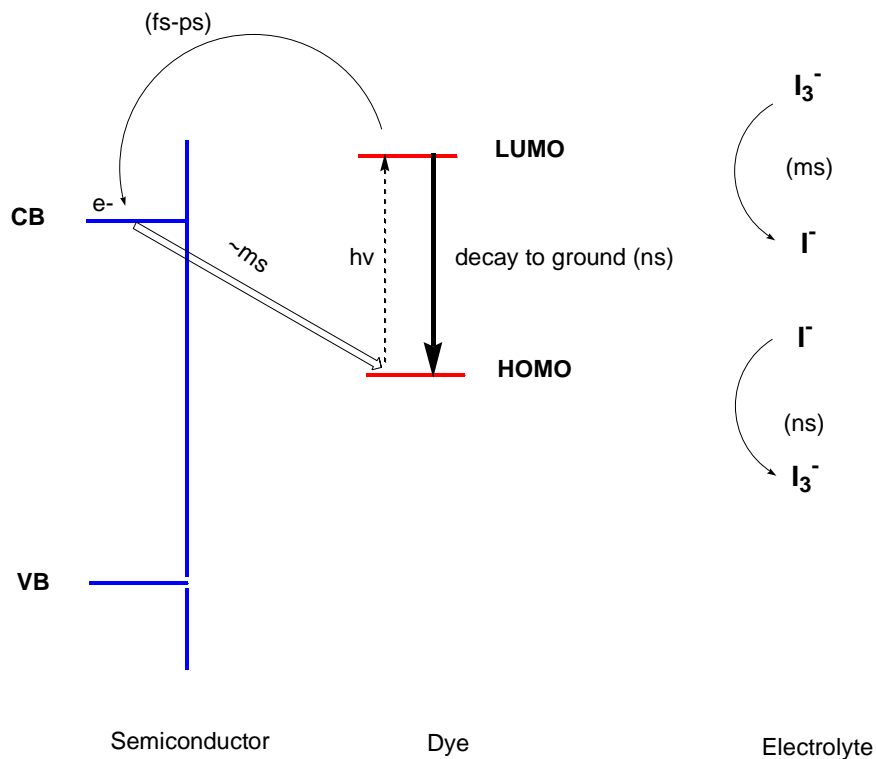


**Figure 3.** Typical timescale for the various electron transfer processes in a DSSC

### 1.3 Key Parameters for DSSC Performance

#### 1.3.1 Incident Photon to Current Conversion Efficiency (IPCE)

The incident photon to current conversion efficiency (IPCE) denotes the overall charge-injection collection process under monochromatic light conditions (single wavelength source). In other words, it measures the efficiency of the cell in converting the incoming photons to photocurrent at different wavelengths. The IPCE can be expressed by the product of the light-harvesting efficiency (LHE), the quantum yields for electron injection and dye regeneration  $\phi_{inj}$  and  $\phi_{reg}$ , and the charge collection efficiency  $\eta_{CC}$ :

$$IPCE(\lambda) = LHE(\lambda)\phi_{inj}(\lambda)\phi_{reg}\eta_{CC}(\lambda) \quad (1)$$

Also, it can be estimated from the quotient of the photocurrent density produced in the external circuit and the photon flux that reaches the cell:

$$\text{IPCE} = \frac{J_{\text{sc}}(\lambda)}{e\Phi(\lambda)} = 1240 \frac{J_{\text{sc}}(\lambda) [\text{A cm}^{-2}]}{\lambda [\text{nm}]\text{Pin}(\lambda)[\text{W cm}^{-2}]} \quad (2)$$

### 1.3.2 *Open-Circuit Photovoltage ( $V_{\text{OC}}$ )*

By definition, the open-circuit voltage denotes the difference in potential between two terminals of a cell when there is no external load i.e. the circuit is open:  $J=0$ , and  $V=V_{\text{OC}}$ . It is determined by the difference between the flatband potential of the semiconductor  $V_{\text{FB}}$ , and the standard reduction potential of the redox mediator  $V_{\text{red}}$  according to the following equation:

$$V_{\text{OC}} = |V_{\text{FB}} - V_{\text{red}}| \quad (3)$$

There are two different mechanisms to increase the  $V_{\text{OC}}$ : either shift the conduction band of the semiconductor towards a more negative potential whilst keeping the potential of the redox couple constant, or suppress recombination between the injected electrons in the semiconductor and the oxidized species in the electrolyte. The flatband potential of the  $\text{TiO}_2$  can be made more negative by adding nitrogen-containing heterocyclic compounds like 4-*tert*-butyl-pyridine (TBP) which increases the  $V_{\text{OC}}$  while keeping the other parameters constant.

### 1.3.3 Short-Circuit Photocurrent ( $J_{sc}$ )

The short-circuit current  $J_{sc}$  (photocurrent per unit area  $\text{mA}\cdot\text{cm}^{-2}$ ) is measured when there is no external voltage applied  $V=0$  upon short-circuiting the cell, hence the maximum current is generated by the cell. It can be obtained by integrating the IPCE spectrum:

$$J_{sc} = \int \text{IPCE}(\lambda) e \varphi_{ph}(\lambda) d\lambda \quad (4)$$

where  $e$  is the elementary charge, and  $\varphi_{ph}$  is the photon flux in AM 1.5 G, 100  $\text{mW}\cdot\text{cm}^{-2}$ . The photocurrent is influenced by several factors: (1) photon harvesting, (2) photoelectron injection, which means that the dye should have suitable energy levels with respect to the semiconductor, (3) dye regeneration, (4) dye loading without any aggregation, (5) light intensity, (6) the light-absorption coefficient of the dye. Based on the above two parameters, one can plot the I-V curve which evaluates the performance of a cell.

### 1.3.4 Fill Factor (FF)

The fill factor measures the squareness of the I-V curve, and takes a value between 0 and less than 1, whereby a high value indicates a more favorable rectangular shape. It is defined by the ratio of the maximum power obtained by the cell divided by the  $V_{oc}$  and  $J_{sc}$ :

$$FF = \frac{P_{max}}{J_{sc}V_{oc}} \quad (5)$$

The fill factor is related to the series resistance  $R_S$  and the shunt resistance  $R_{Sh}$  of the solar cell. The former is mainly an internal resistance of the contacts inside the cell, and is affected by charge transport. The latter, or the parallel resistance, is due to the leakage of currents inside the device. The best fill factor values are obtained when decreasing the series resistance and increasing the shunt resistance.

### **1.3.5 Overall Power Conversion Efficiency ( $\eta$ )**

The overall sunlight-to-electric-power conversion efficiency is given by the following formula:

$$\eta = \frac{P_{\max}}{P_{\text{in}}} = \frac{J_{\text{sc}}V_{\text{oc}}FF}{P_{\text{in}}} \quad (6)$$

where  $P_{\text{in}}$  is the power density of the incident light. Not only does the PCE reflect the performance of the solar cell, but also it depends on the intensity of the incident light, the sensitizer, and the electrolyte system, therefore, to obtain higher efficiency cells, optimization of  $V_{\text{OC}}$ ,  $J_{\text{SC}}$ , and FF values is essential.

### **1.3.6 Electrochemical Impedance Spectroscopy (EIS)**

Electrochemical Impedance Spectroscopy (EIS) is a valuable steady-state method that allows to probe deeper into the kinetics of electrochemical processes and the different components' resistance and capacitance. It is frequently used to evaluate the current response  $I(\omega, t)$  upon the application of an AC voltage  $V(\omega, t)$  as a function of frequency ( $f = \omega/2\pi$ ).<sup>43,44</sup> When measuring the impedance of a DSC, the imaginary frequency  $Z''$  is

plotted as a function of the real one  $Z'$ , giving rise to a Nyquist plot. In a standard Nyquist plot, half-circles will appear in the spectrum as depicted in Figure 4.

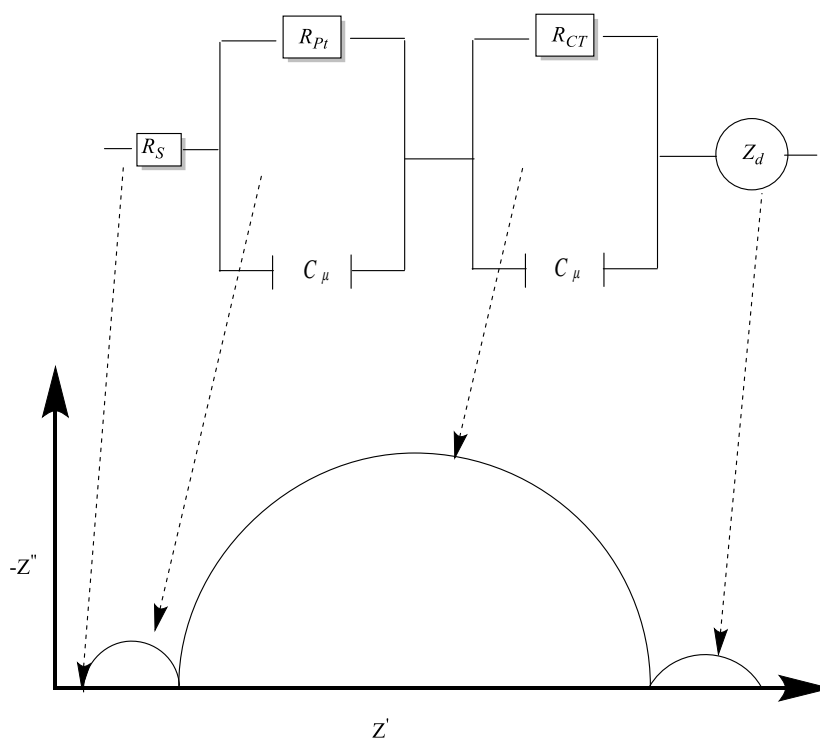


**Figure 4.** Typical Nyquist plot with their equivalent circuits of a DSC

Normal scans are completed from high frequency to low frequency, leading to the appearance of three semi-circles. The onset of the first semi-circle symbolizes the series resistance  $R_S$ , which denotes the resistances at the external wires and contacts, and the FTO glass. The high frequency semi-circle (left) is attributed to the charge transfer resistance  $R_{CE}$  at the counter electrode. This impedance contains both the double layer capacitance  $C_{\mu}$ , and the electron transfer resistance  $R_{Pt}$ . The second semicircle represents the  $\text{TiO}_2/\text{dye}/\text{electrolyte}$  interface. It is associated with the transport of electrons in the

semiconductor, and the electron recombination at the TiO<sub>2</sub>/electrolyte boundary. R<sub>CT</sub> represents the charge transfer resistance of electron recombination, and C<sub>μ</sub> denotes the chemical capacitance at the TiO<sub>2</sub> interface. An increase in R<sub>CT</sub> represents a decrease in the recombination processes of a DSC. The final circle at the lowest frequency region gives the diffusion of the redox species in the electrolyte Z<sub>d</sub>. Moreover, the following product can evaluate the electron lifetime  $\tau = R_{CT} \cdot C_{\mu}$ .

## **1.4 Basic Components of a DSSC**

### ***1.4.1 The Mesoporous Titanium Dioxide Semiconductor***

As mentioned previously, a DSSC requires a conducting glass substrate, which must be characterized by low sheet resistance, temperature independence, high visible light transmittance, and decent electrical conductivity. The most commonly used transparent conducting oxide (TCO) coated glass sheets are fluorine- and indium-doped tin oxide, whereby the former is preferred due to the poor thermal stability of the latter when sintering at high temperatures.

For an ideal semiconductor material, several factors must be taken into consideration such as chemical stability, inertness towards electrolyte species, its conduction band must be lower than the LUMO level of the dye for efficient electron injection, and it must possess a nanostructured geometry to enable high dye loading. It is also crucial that the nanostructured semiconductor should possess a mesoporous morphology to increase the surface area. Numerous wide-bandgap semiconductors fit these requirements, and have been investigated over the past few years, such as ZnO, SnO<sub>2</sub>, and

Nb<sub>2</sub>O<sub>5</sub>, however, titanium dioxide TiO<sub>2</sub> is considered the most versatile, providing the highest power conversion efficiency.

Apart from being a key ingredient in white paint, TiO<sub>2</sub> is highly abundant, nontoxic, and chemically stable. It exists in many crystalline forms including anatase, rutile, and brookite. Anatase is the favored structure for DSSC applications due to its wider bandgap, (3.2 eV compared to 3.0 for rutile) and higher conduction band edge which increases the open circuit voltage V<sub>OC</sub>. The optimal pore size of the TiO<sub>2</sub> nanoparticles is in the range of 15-30 nm with a layer thickness of 5 to 15 μm. For the deposition of the titania light-absorbing layer, screen-printing or doctor-blading techniques are most commonly used, affording a large surface area for sensitizer adsorption.<sup>45</sup> This step can be preceded by coating the FTO plate with a TiO<sub>2</sub> blocking layer to prevent electron recombination between the electrolyte species and the FTO.<sup>46</sup> After coating the titania on the glass substrate, sintering at 400-500 °C is required to remove any solvent or organic residues. This treatment also affords better interconnection between the individual TiO<sub>2</sub> nanoparticles which facilitates electron diffusion in the film. A light-scattering (photon-trapping) layer is then deposited on top of the titania layer bearing a thickness of ~ 3 μm with ~ 400 nm sized TiO<sub>2</sub> particles.<sup>47</sup> Treatments with TiCl<sub>4</sub> occur once before and once after the TiO<sub>2</sub> screen-printing. The former is necessary because it improves the contact between the FTO and the porous layer, hence preventing recombination between the FTO and the redox mediator present in the electrolyte. The latter provides an ultrathin coating of additional TiO<sub>2</sub> particles thus increasing the surface area for dye adsorption which in turn increases the photocurrent.<sup>48</sup> Efforts have been made over the past years to alter the morphology of TiO<sub>2</sub> through the formation of vertically oriented nanotube arrays which can be grown on

the FTO substrate, and are characterized by large surface area, vectorial charge transport along the nanotube, and fewer recombination losses.<sup>49</sup>

Another candidate for DSC semiconductor is ZnO, having similar bandgap and conduction band edge to TiO<sub>2</sub>. An additional advantage is that it possesses a higher electron mobility compared to that of TiO<sub>2</sub> which should favor electron transport, however, also results in higher recombination of the photogenerated electrons.<sup>50</sup> Furthermore, stability issues may also arise since ZnO is corrosive in acidic environment which would result in physical deformation of the nanoparticle layer.

## ***1.4.2 The Electrolyte System***

### ***1.4.2.1 Redox Mediators***

The electrolyte system is an essential feature for DSSC operation; not only does it allow internal charge transport between the working electrode and the counter electrode, but also it allows the regeneration of the oxidized dye after electron injection into the TiO<sub>2</sub> substrate. Therefore, the choice of the electrolyte must take into account the dye's oxidation potential, i.e its redox potential should be higher than that of the dye so that the dye cation can be efficiently reduced. Also, the rate of reduction of the oxidized dye must be greater than the rate of recombination of the dye cations with the electrons in the semiconductor. Another important feature in the electrolyte system is that it must not have significant absorption in the visible light region so as not to compete with the dye's absorption.<sup>23</sup> Electrolytes for dye-sensitized solar cells are divided into three groups: liquid electrolytes, quasi-solid state, and solid state conductors. The liquid electrolyte contains three basic



components: the redox mediator, an organic solvent, and additives. In 1991, O'Regan and Grätzel pioneered an efficient DSSC using a liquid electrolyte containing the redox couple iodide/triiodide dissolved in an organic solvent.<sup>16</sup> Since then, this couple has been the most frequently used redox mediator for DSSC applications for several distinguishing features: it provides fast dye regeneration and sluggish back recombination, passes high conductivity, as well as long-term stability, and ensures effective penetration into the mesoporous semiconductor.<sup>51</sup> Many researchers have considered alternative redox mediators to the (I<sup>-</sup>/I<sup>3-</sup>) paradigm because in addition to being corrosive towards certain metals, this couple exhibits significant absorbance in the visible region. Moreover, its consumption in high concentration might cause recombination with the injected electrons, which in turn unfavorably increases the dark current. The redox potential of an electrolyte  $E_{\text{redox}}$  should be less positive compared to the oxidation potential of the dye and is given by the Nernst equation (7):

$$E_{\text{redox}} = E' + \frac{RT}{2F} \ln \frac{[I_3^-]}{[I^-]^3} \quad (7)$$

Cobalt redox couples were identified as promising substitutes and have provided encouraging results, probably outperforming the typical iodide/triiodide electrolyte system. In fact, in 2011, Yella *et al.* improved the DSSC performance to a whopping 12.3 % by using a Co<sup>(II/III)</sup> tris(bipyridine) redox electrolyte in conjunction with a zinc porphyrin dye YD2-*o*-C8.<sup>52</sup> Compared to the (I<sup>-</sup>/I<sup>3-</sup>) electrolyte, the Co<sup>II</sup>/Co<sup>III</sup> redox couple exhibits weak visible light absorption, it is nonvolatile and less aggressive towards metals, and it has a higher redox potential (0.56 V *vs* NHE) than the previously mentioned couple, which can also be tuned through modifying its ligands. Hamann and coworkers described the

importance of the Co complex structure on the DSSC performance.<sup>53</sup> According to their results, the lifetime at the electrode was in the following order  $[\text{Co}(\text{dtb-bpy})_3]^{2+/3+} > [\text{Co}(\text{dm-bpy})_3]^{2+/3+} > [\text{Co}(\text{bpy})_3]^{2+/3+}$ , and the recombination rate decreased in the reverse direction. Feldt *et al.* generated an overall efficiency of 6.7 % for a solar cell sensitized with a TPA-based dye D35 using  $[\text{Co}(\text{bpy})_3]^{2+/3+}$  as a hole conductor, whereas cells employing the  $\text{I}^-/\text{I}_3^-$  redox couple gave only 5.5 % efficiency.<sup>54</sup> Lately, Mathew and Grätzel reported the molecular engineering of a porphyrin dye coded SM315 featuring a bulky bis (2',4'-bis (hexyloxy)-[1,1'-biphenyl]-4-yl) amine donor with a cobalt(II/III) redox shuttle.<sup>55</sup> This resulted in dye-sensitized solar cells having a high photovoltage  $V_{\text{OC}}$  of 0.91 V, an impressive short-circuit current density  $J_{\text{SC}}$  of  $18.1 \text{ mA}\cdot\text{cm}^{-2}$ , a fill factor FF of 0.78, and an efficiency of 13 %. Aside from the high efficiencies provided by this redox mediator, the greater size of this electrolyte has led to recombination losses and mass-transport limitations. In fact, the diffusion constant of a cobalt-based redox electrolyte ( $\text{Co}(\text{DTB}_3)^{2+/3+}$ ) was found to be significantly lower than that of the triiodide ions inside the  $\text{TiO}_2$  pores, implying that  $\text{TiO}_2$  films with larger porosity would be advantageous.<sup>56</sup> Correspondingly, high recombination rates are always a consequence for one-electron redox systems, therefore, extra measures must be taken in order to block the recombination between the FTO and the Co (III) species; this consists of depositing a compact  $\text{TiO}_2$  blocking layer on the TCO substrate.<sup>57,46</sup>

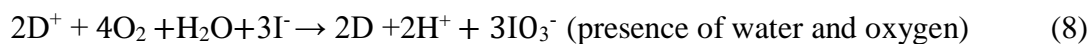
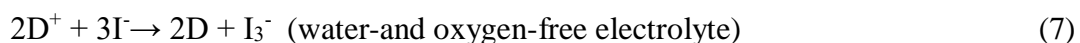
Other redox electrolytes such as  $\text{SCN}^-/(\text{SCN})_3^-$ ,  $\text{Ni(III)/Ni(IV)}$ , and  $\text{Cu(I)/Cu(II)}$  have also been investigated. Bai *et al.* assembled a solar cell with a conversion efficiency of 7 % with an organic dye as a sensitizer and bis(2,9-dimethyl-1,10

phenanthroline)copper(I/II) as electron mediator.<sup>58</sup> With the ferrocene/ferrocenium (Fc/Fc<sup>+</sup>) redox electrolyte (0.62 V) photovoltaic data of  $J_{SC} = 12.2 \text{ mA} \cdot \text{cm}^{-2}$ ,  $V_{OC} = 842 \text{ mV}$ ,  $FF = 0.73$ , and  $\eta = 7.5\%$  were obtained by Daeneke and colleagues.<sup>59</sup>

#### 1.4.2.2 Organic Solvent

An essential component for the dissolution of additives and redox mediators is the organic solvent, which in turn also affects the photovoltaic performance of a DSSC. Some basic requirements for an efficient solvent include: (1) low light absorption, (2) low viscosity to allow high diffusion rates of the electrolyte, (3) high dielectric constant to allow complete dissolving of the electrolyte salts, (4) a boiling point above 100 °C and a melting point below -20 °C to prevent the electrolyte's evaporation, (5) low toxicity and cost. The two main types of solvents that fulfill the above-mentioned criteria are polar organic solvents and ionic liquids. Typically, it is seldom to find a single solvent that fulfills all the desired conditions; for this purpose, mixed solvents are needed for optimal DSSC performance.<sup>60</sup>

Water is a common solvent, however not an ideal choice as an electrolyte solvent. In its presence, the regeneration of the oxidized sensitizer is affected, whereby oxidation of iodide to iodate (IO<sub>3</sub><sup>-</sup>) instead of triiodide takes place<sup>61</sup>, which cannot be further reduced at the counter electrode. This is detrimental to the cell's performance and stability.



Furthermore, the sensitivity of most organic dyes to hydrolysis is also an issue that discourages the use of water as an electrolyte solvent.

The flatband potential  $E_{fb}$  of the mesoporous semiconductor is sensitive to the solvent used. In the presence of a strong electron donating solvent such as dimethyl sulfoxide (DMSO), the conduction band edge of the metal oxide will shift negatively, which increases the open circuit voltage  $V_{OC}$ , however, reduces the short-circuit current  $J_{SC}$  due to the diminution of the driving force of the charge injection of electrons from the excited dye molecules to the semiconductor. Arakawa and Hara examined the photovoltaic performance of mercurochrome-sensitized solar cells with an iodine electrolyte in the presence of different organic solvents.<sup>62</sup> Open circuit voltages ranging between 0.80-0.85 V were obtained for basic solvents such as DMF, DMSO, and NMP, which were higher than any of the nitrile solvents, however lower  $J_{SC}$  were obtained consequently. The increase in  $V_{OC}$  was attributed to the suppression of the dark current arising from the recombination of the oxidized electrolyte with the electrons in the semiconductor. Also, due to the basic property of these solvents, the sensitizer was found to desorb from the surface of the semiconductor, while no desorption was observed for the nitrile solvents. Considering the above limitations, nitrile solvents such as acetonitrile, 3-methoxypropionitrile, valeronitrile, and propionitrile are usually the preferred solvents for DSSC operation owing to their electrochemical stability and suitable polarity when employed with the redox mediators. Even though acetonitrile has good solubilizing ability and low viscosity, its low boiling point is undesirable; an issue that can be solved by employing a mixture of nitriles to increase the boiling point, and minimize evaporation and cell-sealing problems. In 2005, Han and coworkers tried to enhance the low  $V_{OC}$  of N719-sensitized solar cells in

acetonitrile, by mixing it with strong electron donating solvents such as DMSO, THF, DMF etc.<sup>63</sup> As expected, it was found that for DMF/AcN, DMSO/AcN, NMP/AcN, and THF/AcN, the  $V_{OC}$  gradually improved with increasing the donor number (DN) of the other solvent (DMF, DMSO, THF, and NMP) with respect to acetonitrile. The donor number is a parameter that indicates the solvent's electron donating capacity. The observed  $J_{SC}$  trends were different: for THF, the photocurrent density did not change upon increasing its % volume in acetonitrile, however a drastic decrease in  $J_{SC}$  was observed for the other solvents. This can only mean that the THF molecules suppress the back-recombination without changing the conduction level of the semiconductor.

#### 1.4.2.3 Additives and Cations

For further improvement of the DSC performance, the incorporation of nitrogen-containing heterocyclic compounds as additives in the electrolyte has made drastic effects on the recombination kinetics, conduction band edge, and the photovoltaic parameters.

Grätzel first employed 4-tert-butylpyridine (TBP) as an additive in 1993, whereby electrodes dipped in TBP gave higher  $V_{OC}$  and FF compared to untreated ones.<sup>18</sup> The increase in  $V_{OC}$  is certainly due to a reduction in back electron recombination at the dyed- $TiO_2$ /electrolyte interface. The back electron transfer takes place on the surface of the semiconductor that is not covered with dye molecules, so triiodide ions will be adsorbed in their place. With the addition of the TBP, the pyridine units will adsorb on the bare  $TiO_2$  sites, thus preventing the invasion of the triiodide ions. Also, the smaller the size of the derivative, the more effective its adsorption on the  $TiO_2$  sites, and therefore the higher the  $V_{OC}$ . Huang *et al* found that the addition of pyridine derivatives lowered the back-electron

recombination rate constant by 1-2 orders of magnitude.<sup>64</sup> Similar effects were also obtained for other nitrogen-containing compounds like pyridine, benzimidazole, and pyrazole derivatives. Schlichthorl *et al.* explained that the increase in  $V_{OC}$  was also attributed to the negative shift of the conduction band edge of the  $TiO_2$  due to the adsorption of the basic additives.<sup>65</sup> The open-circuit voltage  $V_{OC}$  is given by the difference between the flatband potential of the semiconductor and the standard reduction potential of the electrolyte. If the latter remains constant upon the addition of additives, hence, as the former increases, the  $V_{OC}$  will increase.

Cell performance can also be improved by the addition of deoxycholic acid (DCA) as a co-adsorbent. DCA is used to prevent dye aggregation on the surface of the mesoporous semiconductor thus allowing favorable electron injection from the dye to the  $TiO_2$ . In 2007, Hara and Wang reported a remarkable enhancement in the overall efficiency from 5.0 % to 8.2 % upon the addition of DCA to the dye solution.<sup>66</sup> Even though the amount of adsorbed dye on the  $TiO_2$  surface decreased by  $\sim 50$  %, the  $J_{SC}$  was reportedly improved by 33 %.

Another class of additives contains cations such as  $Li^+$  or  $C(NH_2)_3^+$  as counter ions to the  $I^-$  and  $I_3^-$  in the electrolyte. Apart from ensuring electro-neutrality within the  $TiO_2$  film, the  $Li^+$  cation was found to positively shift the flatband potential of the semiconductor after its intercalation on the  $TiO_2$  surface, which results in an enhanced charge injection from the excited dye to the  $TiO_2$  conduction band, which in turn improves the photocurrent.<sup>67,68</sup> In fact, it was found that the  $J_{SC}$  decreases as the  $V_{OC}$  increases as function of cations in the order:  $Li^+ < Na^+ < K^+ < Rb^+ < Cs^+$ . This can be explained as follows: after the cations are intercalated on the surface of the semiconductor for charge

compensation, the flat band potential of the TiO<sub>2</sub> will move positively, however the potential drop depends on the size and density of the cation. A small-sized cation can easily adsorb on the surface of the metal oxide, resulting in a large potential drop. So as the cation radius increases, the CB edge shifts negatively, resulting in a higher photovoltage. However, a positive movement of the TiO<sub>2</sub> conduction band edge leads to an improved driving force for electron injection, which explains the higher photocurrent. Grätzel reported that the addition of guanidinium cation (G<sup>+</sup>) as a self-assembly facilitating additive reduced the dark current, and achieved an efficiency of 11 %.<sup>69</sup> Zhang *et al.* proved that the presence of the G<sup>+</sup> cations improved the J<sub>SC</sub> due to an enhanced electron injection efficiency.<sup>70</sup>

Even though the nitrogen-containing heterocyclic compounds gave opposite effects to the TiO<sub>2</sub> conduction band edge than the cation additives, the Durrant group proved that an electrolyte incorporating both Li<sup>+</sup> and TBP provided a cell with better performance than one with only one of the additives.<sup>71</sup>

### **1.4.3 The Counter Electrode**

The task of the counter electrode is to reduce the oxidized form of the redox mediator by using the electrons flowing through the external circuit. The material of choice has been platinum, owing to several properties mainly good electrocatalytic activity towards the I<sup>-</sup>/I<sub>3</sub><sup>-</sup> redox reaction, therefore, only a small amount of Pt is needed to be deposited on the TCO. This is advantageous because it cuts costs, given that platinum is considered the most expensive and scarce component of a DSC. Furthermore, because the Pt employed is transparent and thin, platinized counter electrodes can be used in cells that

require reverse lighting. Platinum is also characterized by chemical stability in the electrolyte, which prevents its dissolution overtime. In the absence of platinum, the FTO has a very high charge transfer resistance  $R_{CT}$ , exceeding  $10^6 \Omega \cdot \text{cm}^2$ .<sup>72</sup> To avoid electron loss in the counter electrode, the  $R_{CT}$  should be around  $1 \Omega \cdot \text{cm}^2$ .<sup>73</sup> Platinum can be deposited using several methods such as spray pyrolysis, thermal deposition, sputtering etc. Optimal performance and stability were obtained by thermal decomposition of platinum chloride to form nanoscale platinum clusters on the substrate.<sup>74</sup> Platinum nanoparticles have low  $R_{CT}$ , large surface area, high transmittance, and high electrical conductivity, providing a large number of active sites for the reduction of the triiodide ions.

To manufacture low-cost DSCs, the need to find cheap and abundant materials is essential. Carbon is an attractive option, given its availability, environmental friendliness, and exceptional catalytic activity towards redox species. Kay and Grätzel developed a counter electrode made from a mixture of graphite and carbon black.<sup>75</sup> The graphite provided good electrical conduction as well as catalytic activity, and the carbon offered a large surface area. The cell provided an overall efficiency of 6.7 %. Nazeeruddin reported that conductive polymers having the general formula poly(3,4-alkylthiophenes) gave higher efficiencies for a cobalt-based DSC than platinum.<sup>76</sup> Transition metal sulfides like CoS, MoS<sub>2</sub>, and WS<sub>2</sub> have also been investigated as potential candidates due to their cheap and available feedstock, catalytic activity, and good stability.<sup>77</sup>

#### ***1.4.4 The Dye Sensitizer***

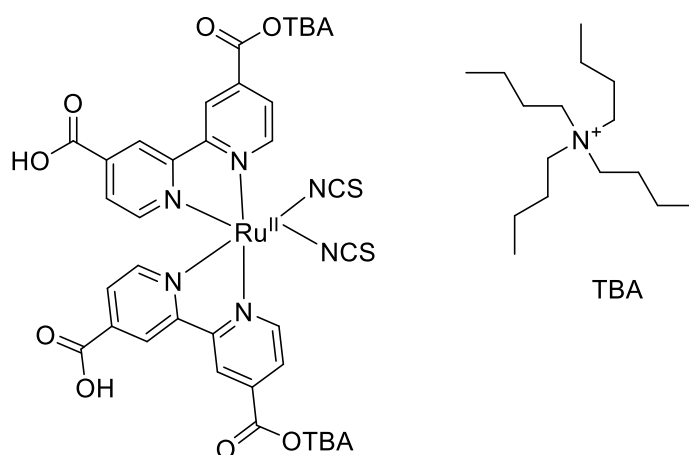
The photosensitizer, an indispensable part of a DSC, assumes the task of both light absorption upon illumination, and charge injection into the semiconductor. It must fulfill a



number of essential requirements for competent solar cell performance and light harvesting efficiency. A desirable property in a dye sensitizer is its ability to cover a wide range of the solar spectrum, even reaching the near-infrared (NIR) region. In addition, its molecular skeleton must be incorporated with anchoring groups such as carboxylate, phosphonate, or sulphonate for efficient grafting to the semiconductor surface. For successful electron injection into the mesoporous TiO<sub>2</sub>, it is crucial that the LUMO level of the excited dye be higher in energy than the conduction band of the semiconductor E<sub>CB</sub>. Correspondingly, for efficient dye regeneration, the oxidized state level (HOMO) of the dye must be sufficiently lower than the redox potential of the employed electrolyte. Also, thermal and chemical stability are key parameters for the dye's sustainability. With the following properties taken into consideration, various photosensitizers have been architected and employed in DSCs in the past decades.

Following Grätzel and O'Regan's revolutionary results in 1991,<sup>16</sup> metal-based dyes incorporating ruthenium (II) complexes have been extensively researched due to their electrochemical stability and broad absorption spectra through a metal to ligand charge transfer (MLCT) process. These metal complexes were designed to include a central metal ion with auxiliary ligands, whereby the latter can be modified to improve the dye's photophysical properties. Among famous Ru (II) polypyridyl complexes, the N3 dye, a thiocyanato derivative having the general formula *cis*-(SCN)<sub>2</sub>bis(2,2'-bipyridyl-4,4'-dicarboxylate)ruthenium(II), gave benchmark results, achieving a solar-to-electric energy conversion efficiency of 10%, and an absorption threshold of around 800 nm.<sup>18</sup> In order to study the effect of protonation, Nazeeruddin and coworkers created the N719 dye (Scheme

2), the doubly deprotonated form of the N3 dye. The study showed that the former dye exhibited superior photovoltaic performance and power conversion efficiency (PCE) compared to sensitizers carrying four or no protons.<sup>78</sup> Due to the fact that extending the sensitizer's spectral response into the near-IR region is advantageous, another reference dye for DSSCs is the renowned panchromatic sensitizer Black Dye N749. Utilizing this dye extended the IPCE spectrum into the near-IR region up to 920 nm, with an overall conversion efficiency of 10.4 %, an open circuit voltage  $V_{OC}$  of 0.72 V, and a short-circuit current  $J_{SC}$  of 20.5 mA/cm<sup>2</sup> under standard AM 1.5 sunlight.<sup>20</sup>



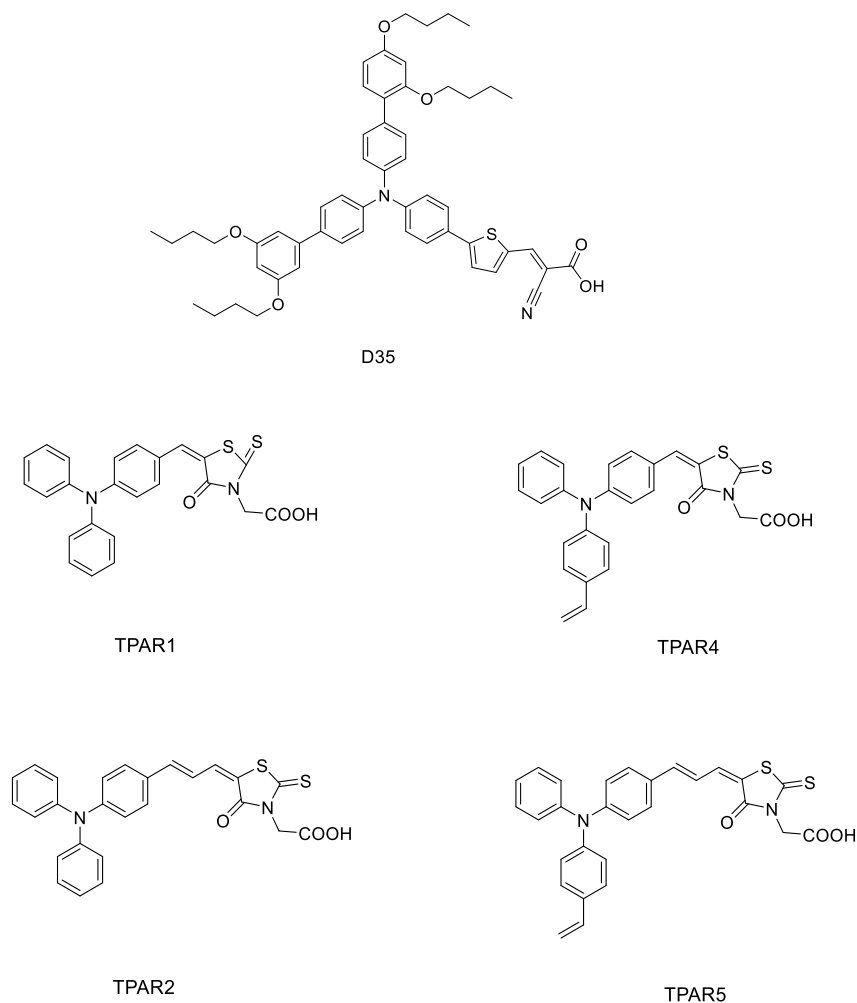
**Scheme 2.** Molecular structure of N719

Regardless of the high efficiency that is provided by the ruthenium complexes, they still possess several drawbacks such as low molar extinction coefficients in the near-IR region, scarce and expensive noble metals, as well as challenging synthetic and purification routes for ligands.<sup>79</sup> To address this dilemma, metal-free organic dyes have emerged as promising candidates to replace the Ru (II) based dyes.

Compared with the metal-based dyes, organic sensitizers display several advantages: (1) the molecular structure can be easily synthesized and tuned; (2) unlike noble metal complexes, organic dyes are cost effective and environmentally friendly; (3) they are characterized by high molar extinction coefficients, which is beneficial for thin film applications. Typically, the skeleton of most organic dyes contains essentially an electron-rich (donor) group and an electron-poor (acceptor) group connected through a conjugated  $\pi$  bridge, creating the typical Donor- $\pi$ -Acceptor molecular structure. The electron-poor section is functionalized with an anchoring group that binds the molecule to the semiconductor oxide surface. To date, considerable efforts have been made to alter the different components of the dye in order to achieve optimal performance.

Triarylamine dyes have been widely investigated by scientists not only due to their excellent electron donating ability, but also because this moiety suppresses aggregation, increases the molar extinction coefficient, and hinders charge recombination.<sup>80</sup> In 2009, Hagfeldt and coworkers reported the synthesis of a novel triphenyl amine (TPA) dye D35 functionalized with *p,o*-butoxy groups (Scheme 3). The study showed that the addition of the bulky butoxy chains prevented the electrons in the semiconductor to recombine with the redox mediator, thus increasing the  $V_{OC}$  to 0.75 V as well as the electron lifetime.<sup>81</sup> Furthermore, in 2007, Liang *et al.* studied the effect of extending the  $\pi$  conjugation bridge as well as enhancing the electron-donating ability of a TPA-based dye TPAR1, yielding three novel chromophores: TPAR2, TPAR4, TPAR5 (Scheme 3).<sup>82</sup> Results showed that the introduction of an alkene to the TPA improved the photovoltaic performance by increasing the electron-density donor moiety, and expansion of the  $\pi$  bridge by the addition of a

methine unit resulted in a red shift and broadening of the absorption spectrum. However, increasing the length of the methine unit resulted in a decrease in the incident photon-to-current conversion efficiency (IPCE). TPAR4-sensitized DSC provided the best photovoltaic performance with an overall efficiency  $\eta$  of 5.84 %.



**Scheme 3.** Molecular structure of D35, and TPA dyes

#### 1.4.4.1 Anchoring Groups and Sites

The molecular adsorption modes of dye molecules onto the surface of the semiconductor can be through several mechanisms including hydrogen bonding, van der

Waals interactions, electrostatic interactions, physical entrapment etc...<sup>83</sup> For this purpose, the dye must be functionalized with an anchoring group that will react spontaneously with the surface hydroxyl groups of the semiconductor, affording stable chemical bonds.

The prototypical anchoring group for sensitizers is the carboxylic acid group (-COOH); it binds to the TiO<sub>2</sub> Brønsted acid sites via a bidentate bridging linkage, a chelating linkage, or an ester bond (Figure 5). It is most commonly used in transition metal complexes that are governed by metal-to-ligand-charge-transfer (MLCT) processes. Cyanoacrylic acids have been used as anchoring groups in most organic dyes not only due to their favorable surface adsorption to the oxide, but also because they provide excellent electron withdrawing ability. Hence, intramolecular charge transfer proceeds from the donor group to the group adsorbed to the TiO<sub>2</sub>. Even though the use of cyanoacrylic acids has favorably red-shifted the absorption spectrum, Chen *et al.* reported in 2013 that such an anchor will cause dye degradation under prolonged illumination, whereby the cyanoacrylic unit will be converted into an aldehyde group in the presence of water.<sup>84</sup> Furthermore, Kloo and coworkers recounted a reversible trans–cis-photoisomerization process for a newly synthesized dye containing an exocyclic double bond as a linker to the triphenylamine donor and the cyanoacrylic acid acceptor.<sup>85</sup>

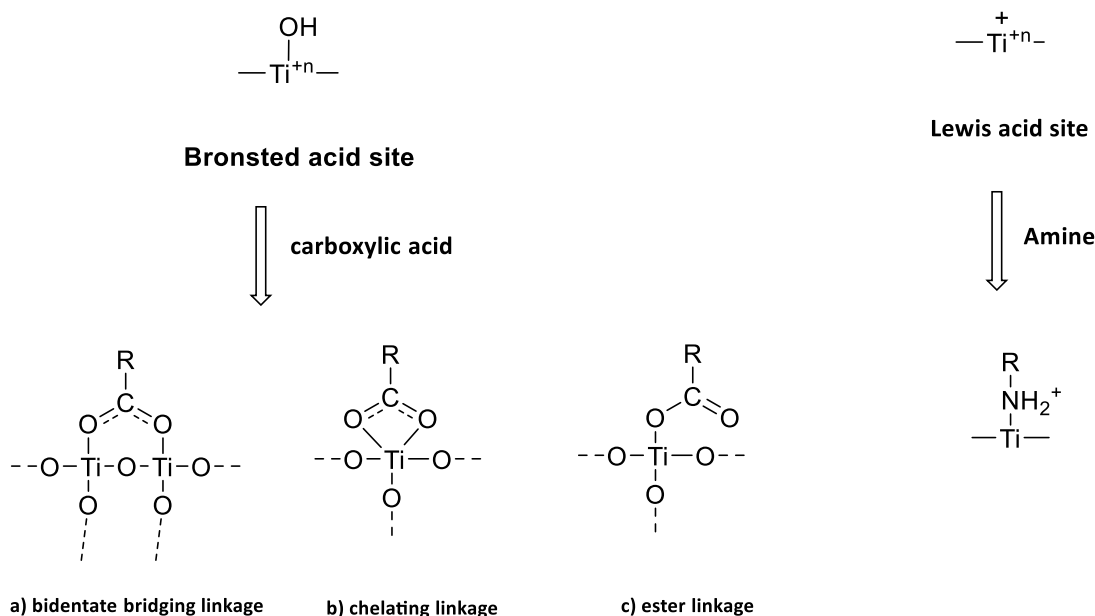
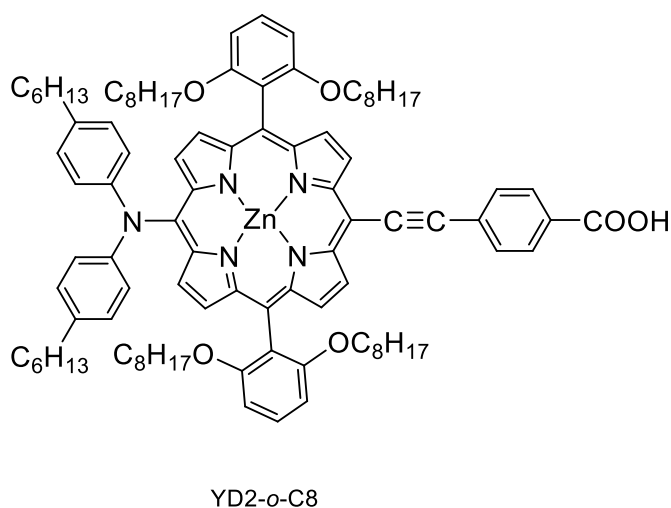


**Figure 5.** Binding modes for carboxylic acids and amines on the metal oxide

Recently, Ooyama *et al.* proposed the use of a pyridine ring as an anchor and electron-acceptor in a class of carbazole-based dyes.<sup>86</sup> It was demonstrated that the anchoring site for such dyes appears to be different from that of the carboxylic anchor; a coordination bond is formed between the lone pair of the pyridine nitrogen and the exposed  $\text{Ti}^{n+}$  Lewis acid sites of the  $\text{TiO}_2$  substrate (Figure 5). Following this discovery, the synthesis and characterization of two fluorescent dyes holding two pyridyl anchors was investigated.<sup>87</sup> Additionally, one of the dyes was engineered to extend the  $\pi$  conjugation by incorporating thiophene groups between the carbazole moiety and the pyridyl units. A bathochromic shift in the UV-vis spectrum and broadening of ICT band was observed, which in turn improved the molar extinction coefficient  $\epsilon$ . Based on the molecular structure of the famous dye YD2-*o*-C8 (Scheme 4), the Grätzel group synthesized in 2015 porphyrin

dyes MH1, MH2, and MH3 bearing 2-pyridinecarboxylic acid, 2-pyridone, and pyridine as anchoring groups.<sup>88</sup> Fully-assembled solar cells based on these dyes gave photovoltaic results comparable to the standard YD2-*o*-C8 sensitizer, whereby power conversion efficiencies ranging between 8.2-8.5 % were obtained for the three dyes.



**Scheme 4.** Molecular structure of YD2-*o*-C8

Phosphonic acid groups have also been investigated as potential anchors for DSSC purposes due to their excellent adsorption ability onto the metal oxide surface via P–O–M bonds.<sup>89</sup> Nevertheless, because of the tetrahedral geometry of the phosphorous center, the charge transfer rate of such anchors is mild, and thus unmatched to the benchmark carboxylic acid. Also, considerable work has been done using pyridine-N-oxide groups,<sup>90</sup> hydroxamate groups,<sup>91</sup> and sulfonic acids<sup>92</sup>, all of which gave considerable effects at the interface between the dye and the semiconductor. The search for novel anchors for DSSC

purposes is still ongoing, and their application in quantum dot solar cells and water splitting systems is further anticipated.

## **1.5 Co-adsorption using Nitrogen-Containing Organic dyes**

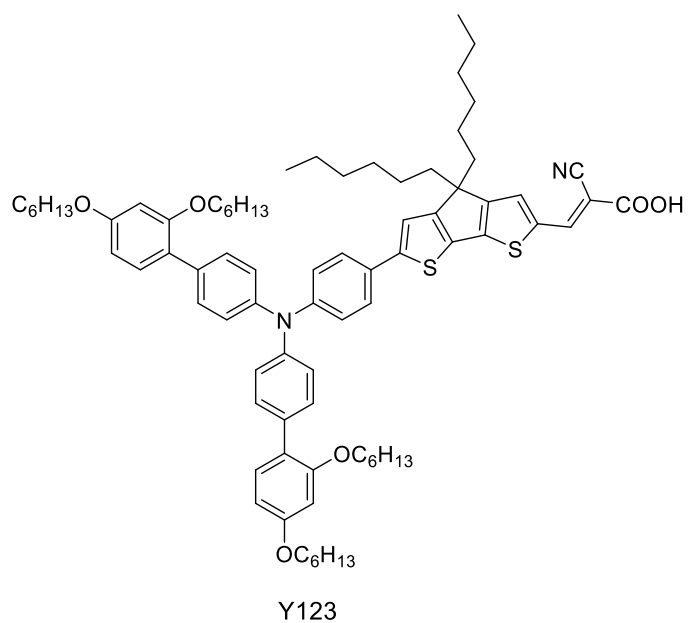
### ***1.5.1 Literature Review***

In an attempt to broaden the spectral response and improve conversion efficiencies, the combination of two dyes having complementary absorption properties was thoroughly investigated by numerous researchers.

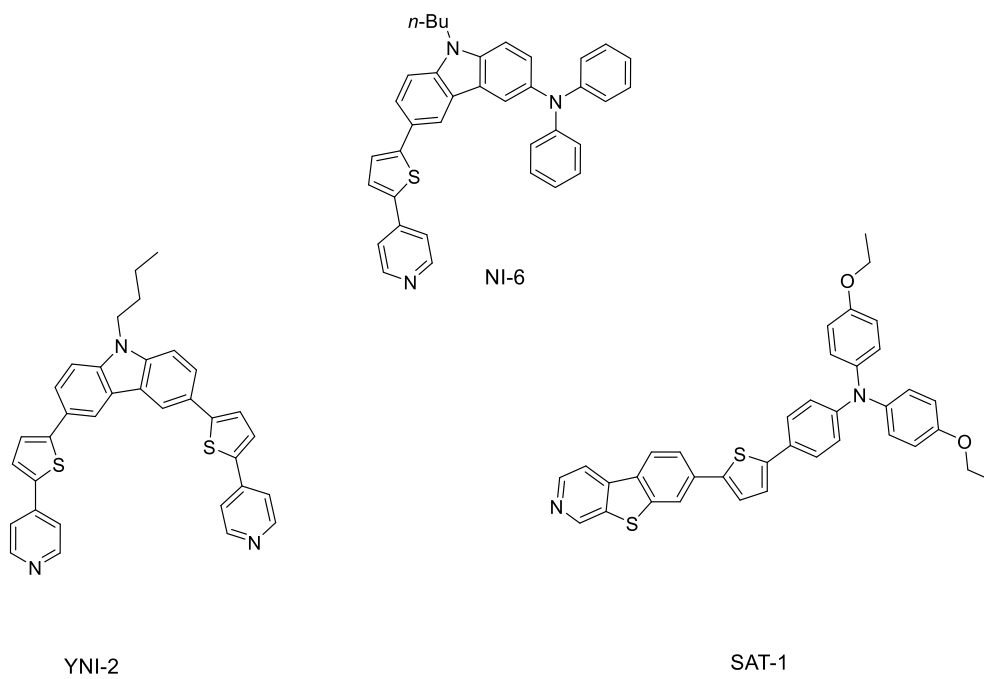
For example, the co-sensitization of zinc-porphyrin dye YD2-*o*-C8 with the organic dye coded Y123 (Scheme 5) yielded an overall power conversion efficiency of 12.3 % under AM 1.5 G irradiation.<sup>52</sup> However, this did not solve the problem of competitive dye adsorption. Noda and co-workers reported an 11 % efficiency of a DSC system made by combining Black Dye, and an organic indoline dye.<sup>93</sup> It was found that the organic dye acted as a dissociation agent similar to chenodeoxycholic acid used previously with Black Dye solely, which in turn improved the DSC efficiency. Recently, Arakawa and Ooyama made use of the TiO<sub>2</sub> Lewis acid sites by co-sensitizing Black dye with a pyridine-anchor dye.<sup>94</sup> It was demonstrated in this study that site-selective adsorption on the surface of the titania took place without any competitive dye adsorption due to the fact that the carboxyl-anchor Black dye coordinates to the Brønsted acid sites of the TiO<sub>2</sub> via dehydration reactions, whereas the pyridyl-anchor one favorably binds to the TiO<sub>2</sub> Lewis acid sites. Also, given that the two sensitizers have complementary absorption properties, the performance of the Black Dye was moderately improved upon mixing it with the pyridine-



anchor dye. Nonetheless, no significant change in  $V_{OC}$  and FF was observed upon co-sensitization, and the slight increase in  $J_{SC}$  accounted for the 0.3-0.5 % increase in power conversion efficiency. Also, upon mixing these two dyes, a ligand exchange reaction might occur which may decrease the amount of dye adsorbed on the  $TiO_2$  electrode. In addition, a stepwise adsorption method is required between the carboxyl anchor dye and the pyridine anchor dye to prevent NCS ligand substitution with the pyridine group. To overcome these disadvantages, Ooyama *et al.* reported in 2015, that a D- $\pi$ -A dye SAT-1 (Scheme 6) with a thiophene-fused pyridine ring, predominantly adsorbed on the  $TiO_2$  Brønsted acid sites.<sup>95</sup> To further prove the innovative effect of co-sensitization in DSCs, the group carried on to form dye cocktails of SAT-1 and two different pyridyl-anchor dyes (NI-6 or YNI-2) whereby the latter dyes favorably adsorb on the exposed Lewis acid sites of the metal oxide. Subsequently, the best photovoltaic performance for co-sensitized DSCs was obtained by a one-step co-adsorption method. This site-selection adsorption behavior remarkably increased the photovoltaic parameters in both combinations with respect to SAT-1 sensitized solar cells. Conversely, it was noticed that both the photocurrent density and the overall efficiency of co-sensitized SAT-1/NI-6 and SAT-1/YNI-2 are lower or equivalent to the DSC devices based on NI-6 and YNI-2 alone. These results were attributed to the poor complementary absorption properties of the respective dyes, which led to a decrease in the electron injection efficiency.

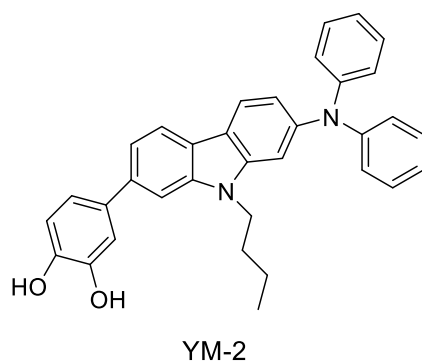


**Scheme 5.** Molecular structure of Y123

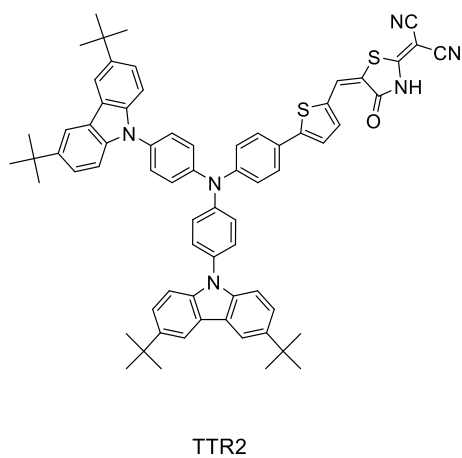
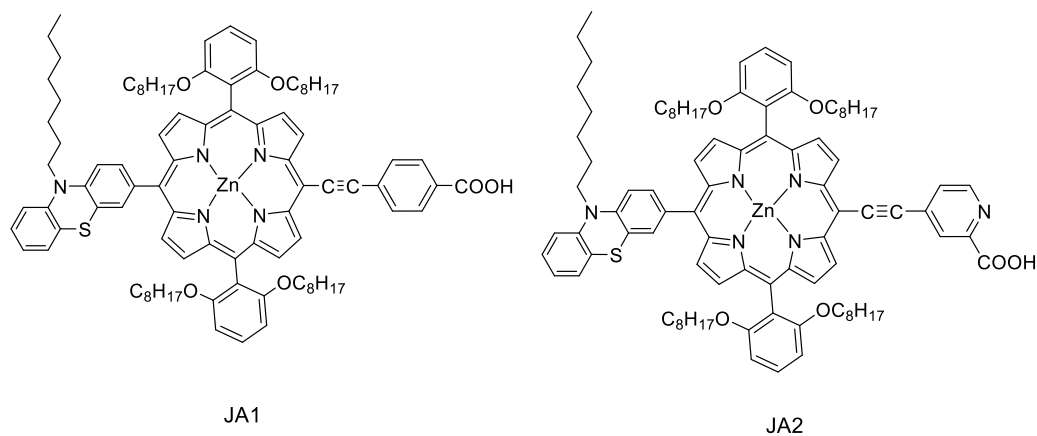


**Scheme 6.** Molecular structures of SAT-1, NI-6, and YNI-2

On the basis of this finding, Ooyama's group provided a new approach for co-adsorbing sensitizers: the co-sensitization of D- $\pi$ -A dyes with a pyridine anchor NI-6 or YNI-2, and a D- $\pi$ -Cat (catechol) sensitizer YM-2 (Scheme 7).<sup>96</sup> It was demonstrated that the Cat dye binds to the semiconductor's Brønsted acid sites via a bidentate linkage, providing remarkable light-harvesting efficiencies over a wide range of the solar spectrum. Photovoltaic data showed that the photocurrent density  $J_{sc}$  and solar energy-to-electricity conversion efficiency  $\eta$  of co-sensitized DSSC (YM-2+ NI-6 and YM-2+ YNI-2) are much lower than DSSC devices based only on NI-6 or YNI-2, but quite similar to those based on YM-2 alone. This decrease in the performance of the co-sensitized devices is mainly attributed to the lowered electron injection efficiency by electron transfer between the two dyes. Furthermore, Zheng *et al.* synthesized two new zinc-porphyrin dyes differing only in their anchoring groups: one consists of the traditional carboxylate anchoring group JA1, and the other incorporates a new picolinic acid anchor JA2 (Scheme 8).<sup>97</sup> This novel anchor can adsorb onto the metal oxide's surface via a tridentate mode, allowing the dye to choose between Brønsted acid sites and Lewis acid sites accordingly. Upon co-sensitizing these respective dyes with a TTR2 dye, it was clearly shown that there was a competitive adsorption between the carboxylate-based dye JA1 and TTR2, which led to a decrease in the overall device performance. Nonetheless, the co-sensitized picolinic-based dye showed no opposing adsorption properties, resulting in a  $J_{sc}$  of 17.75 mA.cm<sup>-2</sup>, a  $V_{oc}$  of 755 mV, a FF of 0.67, and a  $\eta$  of 8.98 %, all of which are higher than the photovoltaic values obtained for JA2 and TTR2 alone.



**Scheme 7.** Molecular structure of YM-2



**Scheme 8.** Molecular structures of JA1, JA2, and TTR2

## 1.6 Objective of Work

Inspired by the studies mentioned previously concerning a pyridine anchor, a cobalt redox shuttle, and the efficiency of dye cocktails, we designed and synthesized three novel dyes, T200, T201, and T202 bearing pyridine as anchoring and electron-withdrawing group. All the dyes have a bulky triphenylamine as a donor group, whereby supplementary butoxy chains were added to increase the hydrophobicity of the dyes, prevent dye aggregation, as well as suppress the recombination reactions by forming an aliphatic network, thereby preventing the  $\text{Co}^{3+}$  ions from reaching the  $\text{TiO}_2$  surface. To further increase the molar extinction coefficients of the sensitizers, we expanded the pi-conjugation by incorporating thienyl groups to their molecular structures. Therefore, the organic dyes differ only by their middle acceptor linkers. The photovoltaic, optical, and electrochemical performance of fully-assembled solar cells were investigated using cobalt-based electrolyte systems. The  $[\text{Co}(\text{bpy})_3]^{2+/3+}$  redox mediator was used instead of the prototypical  $\text{I}^-/\text{I}_3^-$  due to its weak visible light absorption, as well as its higher redox potential which not only enhances the photovoltage, but also minimizes the driving force required for the regeneration of the oxidized sensitizer. Finally, we also explored the co-sensitization of T202 and T201 with various commercially available dyes such as YD2, N719, and DB, as well as ruthenium dyes previously synthesized in our lab.

## CHAPTER II

### EXPERIMENTAL MATERIALS AND INSTRUMENTATION

#### 2.1 Materials

All organic chemicals were purchased from Sigma-Aldrich and used as supplied. Dyenamo Blue and YD2 dyes were purchased from Dyenamo (Sweden). FTO glass "Tec15" and "Tec8" were purchased from Pilkington (USA). TiO<sub>2</sub> colloids 30NR-D and WER2-O were purchased from Dyesol (Australia).

#### 2.2 Instrumentation

The NMR spectra (<sup>1</sup>H and <sup>13</sup>C) were measured on a Bruker AM 500 MHz spectrometer. UV-vis spectra were recorded on a Jasco V-570 UV/vis/NIR spectrometer. Steady state emission spectra were measured on a JobinYvon Horiba Fluorolog-3 spectrofluorometer. The electrochemical setup consisted of a three-electrode cell, with a platinum rod as the working electrode, a Pt wire ~ 1 mm diameter as the counter electrode, and Ag/Ag<sup>+</sup> (10 mM AgNO<sub>3</sub>) as the reference electrode. The electrochemical measurements were performed in 0.1 LiClO<sub>4</sub> in DMF, and Fc/Fc<sup>+</sup> standard (0.69 vs NHE in DMF) was used as an internal reference. Electrochemical impedance spectra of the DSSCs were performed with CH Instruments 760B (USA). The obtained impedance spectra were fitted with the Z-view software (v2.8b, Scribner Associates Inc.). The spectra were performed in the frequency range 0.1 Hz - 10<sup>5</sup> Hz with oscillation potential amplitudes of 10 mV at RT under open circuit conditions at different light levels. IPCE% spectra were

recorded using a Newport 74000 Cornerstone™ monochromator. Photocurrent vs. Voltage characteristics were measured with a Keithley 2400 sourcemeter and a solar simulator illuminated by a Xenon arc lamp (Oriel) through an AM1.5 simulation filter (ScienceTech). The irradiated area of the cell was 0.5 x 0.5 cm<sup>2</sup> with a 0.6 x 0.6 cm<sup>2</sup> black mask.

### 2.3 Computational Methods

Calculations were carried out using *Gaussian 03*. Geometries were optimized using the 6-31G\* basis set with (CAM-B3LYP) in water (C-PCM algorithm).

### 2.4 Solar Cell Fabrication

Dye-sensitized solar cells were fabricated using standard procedures. A compact titania layer (Ti-nanoxide BL/ SP, Solaronix, Switzerland) was spin-coated on a clean fluoride-doped conductive glass TEC15. This was followed by a pre-treatment process with 40 mM TiCl<sub>4</sub> aqueous solution at 70 °C for 1 hour. After that, a 4 μm mesoporous layer of TiO<sub>2</sub> was printed on the glass by the doctor-blading method from a diluted titania paste (60% TiO<sub>2</sub> Dyesol 30NR-D, 34% terpineol and 6% ethyl cellulose), followed by a 4 μm Dyesol WER2-O TiO<sub>2</sub> paste scattering layer. Then, the electrodes were sintered at 450-500 °C for 60 min, followed by a post-treatment process with 40 mM TiCl<sub>4</sub> aqueous solution at 70 °C for 30 min. An additional heating of the films at 500 °C for 1 hour is required before sensitizing them with the corresponding dye solutions in a 1:1:1 THF/acetonitrile/ tert-butanol mixture overnight. The counter electrodes, which consist of a TEC8 transparent conductive glass, was coated with a 2–3 μL/cm<sup>2</sup> of 5 mM H<sub>2</sub>PtCl<sub>6</sub> in 2-propanol and heated at 400 °C in the furnace for 20 min precisely. Solar cell assembly was conducted by sealing

the counter electrode to the TiO<sub>2</sub> working electrode using a 25 μm Surlyn (Dupont) spacer at ~100 °C for 3 min. The cobalt electrolyte (consisted of 0.25 M Co<sup>II</sup>(bpy)<sub>3</sub>, 2PF<sub>6</sub>, 0.06 M Co<sup>III</sup>(bpy)<sub>3</sub>, 3PF<sub>6</sub>, 0.1 M LiClO<sub>4</sub>, and 0.2 M *t*-butylpyridine (TBP) in acetonitrile) was inserted through two small holes, previously drilled through the counter electrode, which were then sealed with Surlyn.

## 2.5 Synthesis of Three Novel Dyes

### 2.5.1 Preparation of T200

#### 2.5.1.1 Synthesis of 4,7-dithien-2-yl-2,1,3-benzothiadiazole <sup>98</sup>

In a 100 ml round bottom flask, 4,7-Dibromo-2,1,3-benzothiadiazole (2 g, 6.8 mmol) and 2-thiopheneboronic acid (2.6 g, 20.4 mmol) were mixed along with triphenylphosphine PPh<sub>3</sub> (1.135 g, 4.08 mmol), potassium carbonate K<sub>2</sub>CO<sub>3</sub> (4.5 g, 137.45 mmol), and palladium acetate Pd(OAc)<sub>2</sub> (0.15 g, 0.70 mmol). The mixture was dissolved in tetrahydrofuran, purged under argon, and refluxed for 48 hrs. Solvent was removed under reduced pressure, and the reaction mixture was quenched with water. The solid was collected by suction filtration and washed with water and cold ethanol, resulting in an orange-brown solid. The solid was purified by column chromatography using toluene (and a small amount of hexane) as a mobile phase. 4,7-dithien-2-yl-2,1,3-benzothiadiazole was isolated as a bright orange solid (1.89 g, 93 %). <sup>1</sup>H NMR (500 MHz, CDCl<sub>3</sub>): δ 8.06 (dd, *J*= 3.5 Hz, *J*= 1 Hz 2H), 7.82 (s, 2H), 7.40 (dd, *J*= 5 Hz, *J*=1 Hz, 2H), 7.16 (dd, *J*= 4 Hz, *J*= 1.5 Hz, 2H). <sup>13</sup>C NMR (125 MHz, CDCl<sub>3</sub>): δ 152.68, 139.37, 128.1, 128.05, 127.53, 126.84, 125.84.



### 2.5.1.2 Synthesis of 4,4'-dihydroxybenzil<sup>99</sup>

In a 500 mL round bottom flask, a mixture of 1,2-Bis(4-methoxyphenyl)ethanedione (7 g, 25.9 mmol), aqueous HBr and glacial acetic acid were mixed and refluxed overnight. The reaction mixture was cooled to room temperature, and extracted using ethyl acetate and brine. The organic layer was then dried with magnesium sulfate, and the solvent was removed under reduced pressure. The solid was collected by suction filtration and washed with water. 4,4'-dihydroxybenzil (5.08 g, 81 %) was collected as a yellow solid. <sup>1</sup>H NMR (500 MHz, DMSO-*d*<sub>6</sub>):  $\delta$  7.81 (d, *J* = 8.5 Hz, 4H), 6.99 (d, *J* = 8.5 Hz, 4H). <sup>13</sup>C NMR (125 MHz, CDCl<sub>3</sub>):  $\delta$  194.14, 164.51, 132.73, 124.60, 116.60.

### 2.5.1.3 Synthesis of 4,4'-diethylhexylbenzil<sup>100</sup>

In a 500 mL round bottom flask, 4,4'-dihydroxybenzil (5 g, 20.64 mmol), potassium carbonate K<sub>2</sub>CO<sub>3</sub> (11.4 g, 82.56 mmol), and 2-ethylhexyl bromide (8.76 g, 45.40 mmol) were mixed in acetone. 18-crown ether was then added and the reaction mixture was purged under argon and refluxed for 48 hrs. The reaction was then cooled to room temperature, and solvent was removed under reduced pressure. The mixture was then poured into water and dichloromethane was added. The organic layer was separated and dried with magnesium sulfate, and the solvent was removed under reduced pressure. The oily yellow compound was purified by column chromatography with hexane: ethyl acetate (20:1) as mobile phase. 4,4'-diethylhexylbenzil was obtained as an oily yellow liquid. <sup>1</sup>H NMR (500 MHz, CDCl<sub>3</sub>):  $\delta$  7.86 (d, *J* = 8.5 Hz, 4H), 6.89 (d, *J* = 9 Hz, 4H), 3.85 (dd, *J* = 5.5 Hz, *J* = 1.5 Hz, 4H), 1.69 (p, 2H), 1.43-1.32 (m overlapping, 9H), 1.25-1.21 (m overlapping,

10H), 0.87-0.82 (m overlapping, 12H).  $^{13}\text{C}$  NMR (125 MHz,  $\text{CDCl}_3$ ):  $\delta$  192.60, 163.72, 131.33, 125.05, 113.72, 69.91, 38.21, 29.89, 29.41, 28.01, 22.77, 21.97, 13.02, 10.05.

#### 2.5.1.4 Synthesis of 2,3-bis[4-[(2-ethylhexyl)oxy]phenyl]-5,8-di-2-thienyl-quinoxaline<sup>101</sup>

In a 500 mL round bottom flask, 4,7-Di(thiophene-2-yl)-2,1,3-benzothiadiazole (0.64 g, 2.14 mmol) and zinc dust (1.72 g) were mixed in glacial acetic acid. The reaction was purged under argon for 30 mins at 80°C. After cooling to room temperature, the greyish solid was removed by suction filtration, washed with acetic acid, and the filtrate was transferred to a 250 mL round bottom flask containing 4,4'-diethylhexylbenzil (1 g, 2.14 mmol). The mixture was purged with argon and heated at 60°C overnight. The solid formed was collected by suction filtration and washed with acetic acid and water. 2,3-bis[4-[(2-ethylhexyl)oxy]phenyl]-5,8-di-2-thienyl-quinoxaline (1.2 g, 80 %) was isolated as a yellow solid in quantitative yield.  $^1\text{H}$  NMR (500 MHz,  $\text{CDCl}_3$ ):  $\delta$  8.03 (s, 2H), 7.79 (dd,  $J= 3.5$  Hz, 2H), 7.67 (d,  $J= 9$  Hz, 4H), 7.45 (dd,  $J= 5$  Hz,  $J= 1$  Hz, 2H), 7.12 (dd,  $J= 5$  Hz,  $J= 3.5$  Hz, 2H), 6.86 (d,  $J= 9$  Hz, 4H), 3.83 (dd,  $J= 5.5$  Hz,  $J= 1.5$  Hz, 4H), 1.70 (p, 5H), 1.48-1.31 (m overlapping, 14H), 1.28-1.25 (m overlapping, 14H), 0.90-0.83 (m overlapping, 16H).  $^{13}\text{C}$  NMR (125 MHz,  $\text{CDCl}_3$ ):  $\delta$  160.24, 151.35, 138.97, 136.98, 131.84, 131.11, 131.04, 128.70, 126.56, 126.53, 126.21, 114.29, 70.61, 39.41, 20.55, 29.12, 23.89, 23.06, 14.10, 11.14.

#### 2.5.1.5 Synthesis of 5,8-bis(5-bromo-2-thienyl)-2,3-bis[4-[(2-ethylhexyl)oxy]phenyl]-quinoxaline<sup>102</sup>

In a 250 mL round bottom flask, dissolve 2,3-bis[4-[(2-ethylhexyl)oxy]phenyl]-5,8-di-2-thienyl-quinoxaline (1.2 g, 1.7 mmol) in THF, and add NBS (0.63 g, 3.58 mmol). The mixture was purged under argon and stirred overnight. After cooling, the solvent was removed under reduced pressure, and the mixture was added into water and extracted with dichloromethane. The organic layer was then dried with sodium sulfate, and purified by column chromatography using hexane as mobile phase. 5,8-bis(5-bromo-2-thienyl)-2,3-bis[4-[(2-ethylhexyl)oxy]phenyl]-quinoxaline (1.31 g, 90 %) was isolated as an orange solid. <sup>1</sup>H NMR (500 MHz, CDCl<sub>3</sub>): δ 7.96 (s, 2H), 7.62 (d, *J* = 9 Hz, 4H), 7.49 (d, *J* = 4 Hz, 2H), 7.05 (d, *J* = 4 Hz, 2H), 6.88 (d, *J* = 9 Hz, 4H), 3.85 (dd, *J* = 5.5 Hz, *J* = 2 Hz, 4H), 1.70 (p, 2H), 1.48-1.33 (m overlapping, 9H), 1.29-1.25 (m overlapping, 9H), 0.90-0.83 (m overlapping, 15H). <sup>13</sup>C NMR (125 MHz, CDCl<sub>3</sub>): δ 159.39, 150.89, 138.82, 135.44, 130.86, 129.61, 129.42, 128.07, 124.38, 124.30, 115.91, 113.34, 69.63, 38.42, 29.53, 28.11, 22.87, 22.04, 13.08, 10.14.

#### 2.5.1.6 Synthesis of T200

In a 50 mL round bottom flask, 5,8-bis(5-bromo-2-thienyl)-2,3-bis[4-[(2-ethylhexyl)oxy]phenyl]-quinoxaline (0.2 g, 0.116 mmol), 4-pyridinyl boronic acid (0.032 g, 0.127 mmol), and 2',4'-Dibutoxy-N-(2',4'-dibutoxybiphenyl-4-yl)-N-(4-(4,4,5,5-tetramethyl-1,3,2-dioxaborolan-2-yl)phenyl)-4-amine (0.21 g, 0.127 mmol) were mixed along with triphenylphosphine PPh<sub>3</sub> (0.028 g, 0.0508 mmol), potassium carbonate K<sub>2</sub>CO<sub>3</sub> (0.47 g, 1.71 mmol), and palladium acetate Pd(OAc)<sub>2</sub> (0.004 g, 0.00875 mmol). A

stoichiometric proportion of dioxane: THF: water (3:2:1) was added, and the reagents were purged under argon and refluxed for 48 hours. The solvent was then removed under reduced pressure and the red solid was then dissolved in dichloromethane, extracted with water, and dried with sodium sulfate. The resulting compound was then purified by column chromatography with hexane: dcm (30:70) as mobile phase. T200 was then isolated as a purple solid with a yield of 46 %. <sup>1</sup>H NMR (500 MHz, Benzene-d<sub>6</sub>) δ 8.34 – 8.31 (m, 2H), 7.75 – 7.68 (m, 2H), 7.67 – 7.60 (m, 5H), 7.52 (dd, *J*<sub>1</sub> = 4.1, *J*<sub>2</sub> = 1.6 Hz, 1H), 7.47 – 7.41 (m, 6H), 7.18 (d, *J* = 8.4 Hz, 2H), 7.12 – 7.04 (m, 8H), 6.99 (d, *J* = 8.6 Hz, 2H), 6.64 (dd, *J*<sub>1</sub> = 8.8, *J*<sub>2</sub> = 7.0 Hz, 4H), 6.47 (d, *J* = 2.4 Hz, 2H), 6.32 (dd, *J*<sub>1</sub> = 8.5, *J*<sub>2</sub> = 2.4 Hz, 2H), 3.54 (t, 4H), 3.44 (t, 4H), 3.39 – 3.35 (m, 4H), 1.47 – 0.98 (m, 22H), 0.67 (q, 15H), 0.63 – 0.55 (m, 13H), 0.24 (d, *J* = 5.2 Hz, 8H). <sup>13</sup>C NMR (126 MHz, C<sub>6</sub>D<sub>6</sub>) δ 202.60, 159.65, 159.13, 156.50, 150.62, 149.83, 146.79, 145.21, 142.73, 140.49, 140.05, 136.86, 136.59, 136.47, 133.07, 131.36, 131.32, 130.59, 130.56, 130.23, 129.79, 123.96, 123.35, 123.23, 122.70, 121.60, 118.54, 113.42, 113.39, 104.52, 100.04, 69.32, 66.92, 66.52, 38.56, 38.53, 30.56, 30.29, 29.73, 29.71, 28.89, 28.24, 28.22, 22.98, 22.24, 22.22, 18.44, 13.14, 12.83, 12.79, 10.12. MALDI-TOF MS (*m/z*): calculated for C<sub>95</sub>H<sub>106</sub>N<sub>4</sub>O<sub>6</sub>S<sub>2</sub>, 1464.0; found 1464.7

## 2.5.2 Preparation of T201

### 2.5.2.1 Synthesis of 3,6-Di(thiophen-2-yl)pyridazine<sup>103</sup>

In a 200 mL round bottom flask, 3,6-Dibromopyridazine ( 2 g, 8.4 mmol) and 2-thienylboronic acid ( 3.22 g, 25.22 mmol) were mixed in 80-90 mL of tetrahydrofuran (THF). Triphenylphosphine PPh<sub>3</sub> (1.40 g, 5.04 mmol), potassium carbonate K<sub>2</sub>CO<sub>3</sub> (4.5 g), and palladium acetate Pd(OAc)<sub>2</sub> (0.19 g, 0.86 mmol) were added, and the reaction mixture

was purged under argon and refluxed for 48 hours. The mixture was then quenched with water, and the dark green solid was collected by suction filtration, and washed with water. The resulting compound was then purified by column chromatography with toluene: ethyl acetate (20:1) as mobile phase. The collected solid was then recrystallized from ethanol, collected by suction filtration, and washed with cold ethanol. 3,6-Di(thiophen-2-yl)pyridazine was isolated as a dark green solid (1.48 g, 72%).  $^1\text{H}$  NMR (500 MHz,  $\text{CDCl}_3$ )  $\delta$  7.76 (d,  $J = 1.5$  Hz, 2H), 7.73 (s, 2H), 7.47 (dd,  $J_1 = 4$  Hz,  $J_2 = 1.5$  Hz, 2H), 7.12 (d,  $J = 1.5$  Hz, 2H).  $^{13}\text{C}$  NMR (126 MHz,  $\text{CDCl}_3$ )  $\delta$  152.21, 139.27, 128.46, 127.18, 126.22, 121.92.

#### 2.5.2.2 Synthesis of 3,6-Bis(5-bromo-2-thienyl)pyridazine<sup>104</sup>

In a 50 mL round bottom flask, dissolve 3,6-Di(thiophen-2-yl)pyridazine (1.1 g, 2.73 mmol) and *N*-Bromosuccinimide (1.50 g, 8.42 mmol) in DMF, stir and heat at 60° C overnight. The solid was collected by suction filtration and washed with water and methanol. 3,6-Bis(5-bromo-2-thienyl)pyridazine was collected as yellow-white crystals (1.17 g, 65 %).  $^1\text{H}$  NMR (500 MHz, DMSO)  $\delta$  8.33 (s, 2H), 7.85 (d,  $J = 4$  Hz, 2H), 7.41 (d,  $J = 4$ Hz, 2H).  $^{13}\text{C}$  NMR (126 MHz, DMSO)  $\delta$  153.32, 142.22, 132.45, 128.89, 123.54, 116.48.

#### 2.5.2.3 Synthesis of T201

In a 50 mL round bottom flask, 3,6-Bis(5-bromo-2-thienyl)pyridazine (0.2 g, 0.50 mmol), 4-pyridinyl boronic acid (0.068 g, 0.55 mmol), and 2',4'-dibutoxy-*N*-(2',4'-dibutoxy-[1,1'-biphenyl]-4-yl)-*N*-(4-(4,4,5,5-tetramethyl-1,3,2-dioxaborolan-2-yl)phenyl)-[1,1'-

biphenyl]-4-amine (0.45 g, 0.55 mmol) were mixed along with triphenylphosphine PPh<sub>3</sub> (0.061 g, 0.22 mmol), potassium carbonate K<sub>2</sub>CO<sub>3</sub> (1.024 g, 7.41 mmol), and palladium acetate Pd(OAc)<sub>2</sub> (0.0085 g, 0.038 mmol). A stoichiometric proportion of dioxane: THF: water (3:2:1) was added, and the reagents were purged under argon and refluxed for 48 hours. The solvent was then removed under reduced pressure and the dark brown solid was then dissolved in dichloromethane, extracted with water, and dried with sodium sulfate. The resulting compound was then purified by column chromatography on silica with 2% methanol in dichloromethane to yield the respective dye in 40%. <sup>1</sup>H NMR (500 MHz, Acetone-*d*<sub>6</sub>) δ 8.54 – 8.49 (m, 2H), 8.09 (d, *J* = 4.1 Hz, 1H), 7.83 (d, *J* = 4.0 Hz, 1H), 7.77 (d, *J* = 3.9 Hz, 1H), 7.72 (d, *J* = 4.0 Hz, 1H), 7.58 (dd, *J*<sub>1</sub> = 8.3, *J*<sub>2</sub> = 1.4 Hz, 4H), 7.55 (d, *J* = 1.5 Hz, 2H), 7.49 (dd, *J*<sub>1</sub> = 7.5, *J*<sub>2</sub> = 1.7 Hz, 3H), 7.42 (s, 3H), 7.17 (d, *J* = 8.4 Hz, 2H), 7.06 (d, *J* = 8.7 Hz, 4H), 6.53 (d, *J* = 2.4 Hz, 2H), 6.48 (dd, *J*<sub>1</sub> = 8.4, *J*<sub>2</sub> = 2.4 Hz, 2H), 3.91 (td, 8H), 1.70 – 1.56 (m, 8H), 1.48 – 1.28 (m, 8H), 0.83 (dt, 12H). <sup>13</sup>C NMR (126 MHz, Acetone) δ 171.29, 159.93, 157.08, 150.62, 145.35, 134.10, 133.76, 132.94, 131.92, 131.89, 131.84, 131.76, 130.67, 130.38, 128.63, 128.54, 126.67, 124.05, 123.50, 122.89, 122.39, 119.60, 105.83, 100.21, 68.45, 67.87, 67.42, 31.26, 31.15, 19.16, 19.05, 13.25. MALDI-TOF MS (*m/z*): calculated for C<sub>63</sub>H<sub>64</sub>N<sub>4</sub>O<sub>4</sub>S<sub>2</sub>, 1005.3; found 1005.4

### 2.5.3 Preparation of T202

#### 2.5.3.1 Synthesis of 4,7-Bis(2-bromo-5-thienyl)-2,1,3-benzothiadiazole<sup>105</sup>

In a 50 mL round bottom flask, 4,7-dithien-2-yl-2,1,3-benzothiadiazole (0.9 g, 3 mmol), NBS (1.12 g, 6.3 mmol), and *o*-dichlorobenzene were mixed. The reaction mixture was heated to 55° C for 3 hrs. After 3 hrs, the temperature was brought up to 150° C till

everything dissolves, and then cooled down to room temperature. The solid was collected by suction filtration, and washed with cold *o*-dichlorobenzene, methanol, and water. 4,7-Bis(2-bromo-5-thienyl)-2,1,3-benzothiadiazole (0.95 g, 70%) was obtained as red-brown crystals. <sup>1</sup>H NMR (500 MHz, DMSO-*d*<sub>6</sub>): δ 8.18 (s, 2H), 7.99 (d, *J* = 4 Hz, 2H), 7.42 (s, *J* = 4 Hz, 2H).

### 2.5.3.2 Synthesis of T202

In a 50 mL round bottom flask, 4,7-Bis(2-bromo-5-thienyl)-2,1,3-benzothiadiazole (0.15 g, 0.33 mmol), 4-pyridinyl boronic acid (0.044 g, 0.36 mmol), and 2',4'-dibutoxy-N-(2',4'-dibutoxy-[1,1'-biphenyl]-4-yl)-N-(4-(4,4,5,5-tetramethyl-1,3,2-dioxaborolan-2-yl)phenyl)-[1,1'-biphenyl]-4-amine (0.30 g, 0.36 mmol) were mixed along with triphenylphosphine PPh<sub>3</sub> (0.040 g, 0.144 mmol), potassium carbonate K<sub>2</sub>CO<sub>3</sub> (0.67 g, 4.85 mmol), and palladium acetate Pd(OAc)<sub>2</sub> (0.0056 g, 0.025 mmol). A stoichiometric proportion of dioxane: THF: water (3:2:1) was added, and the reagents were purged with argon before refluxing for 48 hours. The solvent was then removed under reduced pressure and the dark red solid was then dissolved in dichloromethane, washed with water, and dried over sodium sulfate. The resulting compound was then purified by column chromatography on silica with 1% methanol in dichloromethane as the mobile phase to yield the respective dye with 34.6% yield <sup>1</sup>H NMR (500 MHz, Benzene-*d*<sub>6</sub>) δ 8.55 (d, *J* = 5.0 Hz, 2H), 8.25 (d, *J* = 3.9 Hz, 1H), 8.03 (d, *J* = 3.9 Hz, 1H), 7.70 – 7.65 (m, 4H), 7.58 – 7.54 (m, 2H), 7.51 (d, *J* = 7.7 Hz, 1H), 7.38 (d, *J* = 8.4 Hz, 2H), 7.32 (dd, *J* = 2.3, 9.0 Hz, 5H), 7.24 (d, *J* = 2.1 Hz, 1H), 7.23 – 7.21 (m, 2H), 7.19 (d, *J* = 3.9 Hz, 2H), 6.99 (q, *J* = 1.2, 1.2, 1.2 Hz, 1H), 6.67 (d, *J* = 2.4 Hz, 2H), 6.53 (dd, *J* = 2.4, 8.5 Hz, 2H), 3.75 (t, *J* =

6.4, 6.4 Hz, 4H), 3.64 (t,  $J = 6.4$ , 6.4 Hz, 4H), 1.67 – 1.62 (m, 4H), 1.52 – 1.47 (m, 4H), 1.44 – 1.39 (m, 4H), 1.30 – 1.25 (m, 4H), 0.90 – 0.86 (m, 8H), 0.79 (s, 4H).  $^{13}\text{C}$  NMR (126 MHz,  $\text{C}_6\text{D}_6$ )  $\delta$  160.57, 157.87, 153.03, 151.22, 148.67, 146.70, 146.43, 142.43, 141.66, 141.14, 138.28, 134.74, 131.64, 131.25, 130.17, 127.35, 126.54, 126.13, 125.24, 125.08, 124.78, 124.32, 123.97, 123.95, 119.88, 105.87, 101.40, 68.28, 67.90, 31.95, 31.66, 19.83, 19.81, 14.23, 14.17, 1.61. MALDI-TOF MS ( $m/z$ ): calculated for  $\text{C}_{65}\text{H}_{64}\text{N}_4\text{O}_4\text{S}_3$ , 1061.4; found 1061.3.



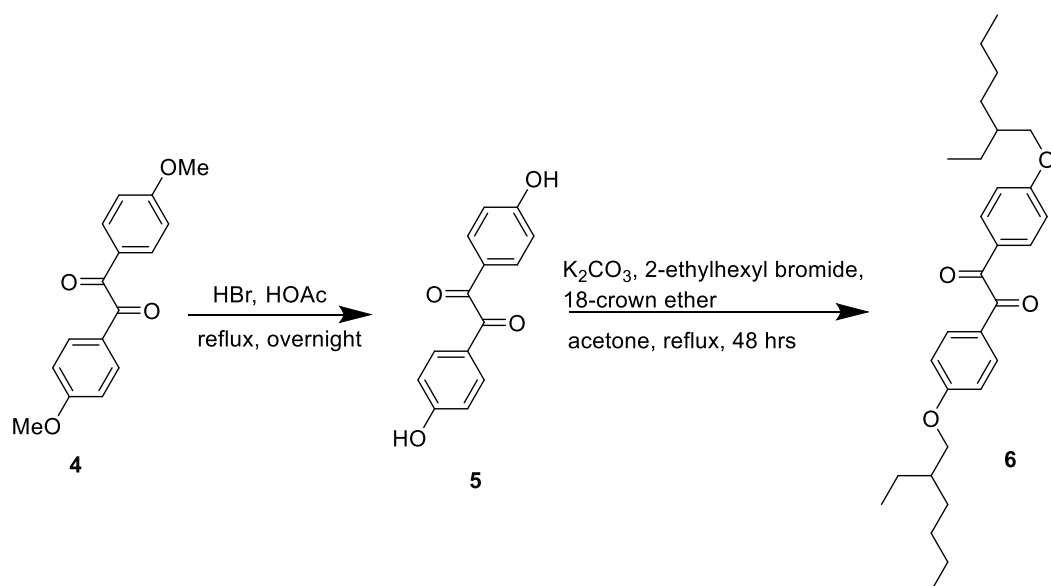
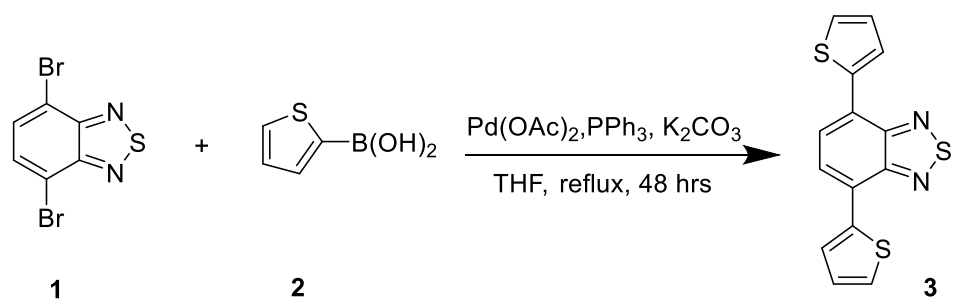
## CHAPTER III

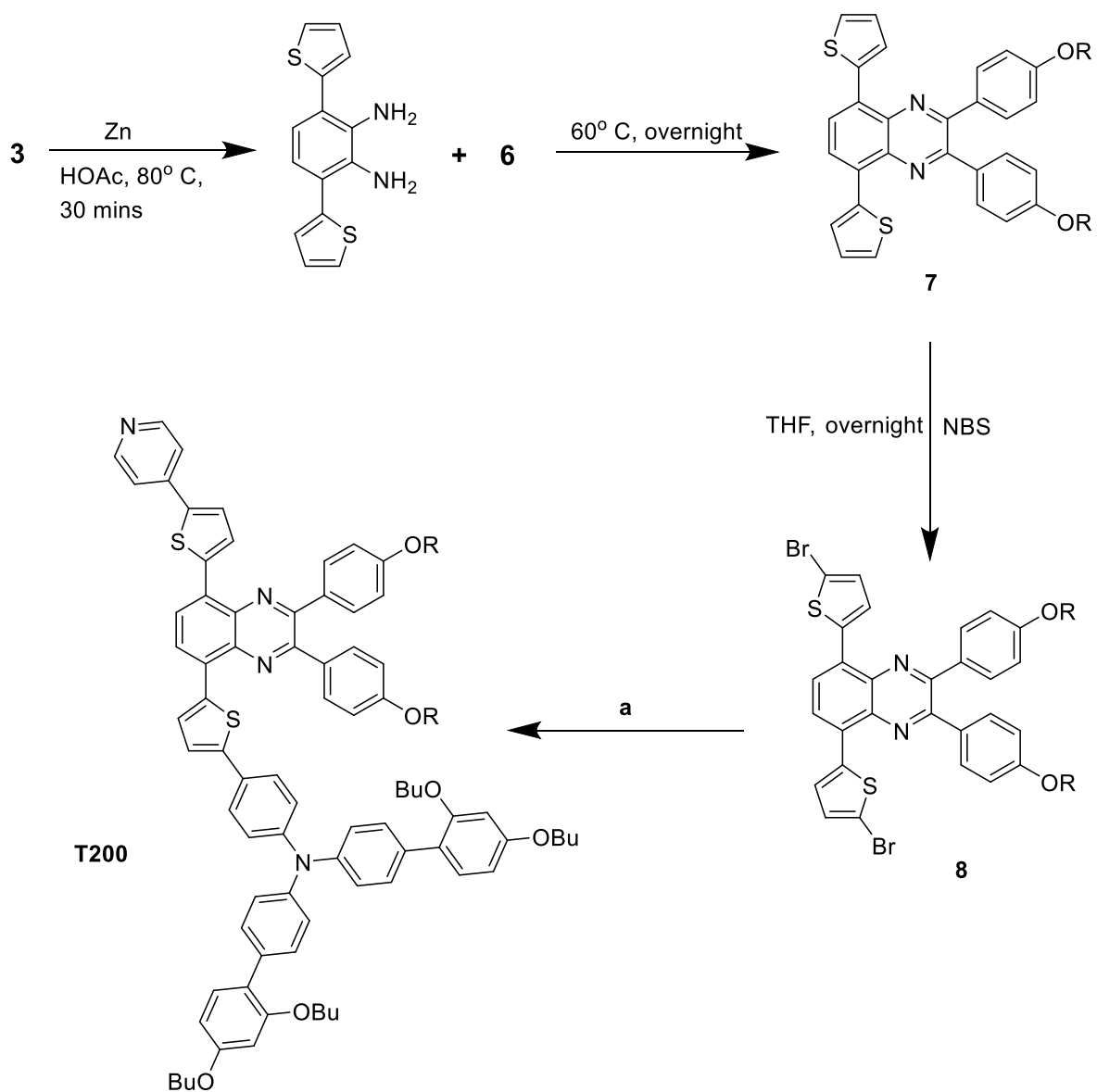
### RESULTS AND DISCUSSION

#### 3.1 Synthesis and Characterization of Dyes

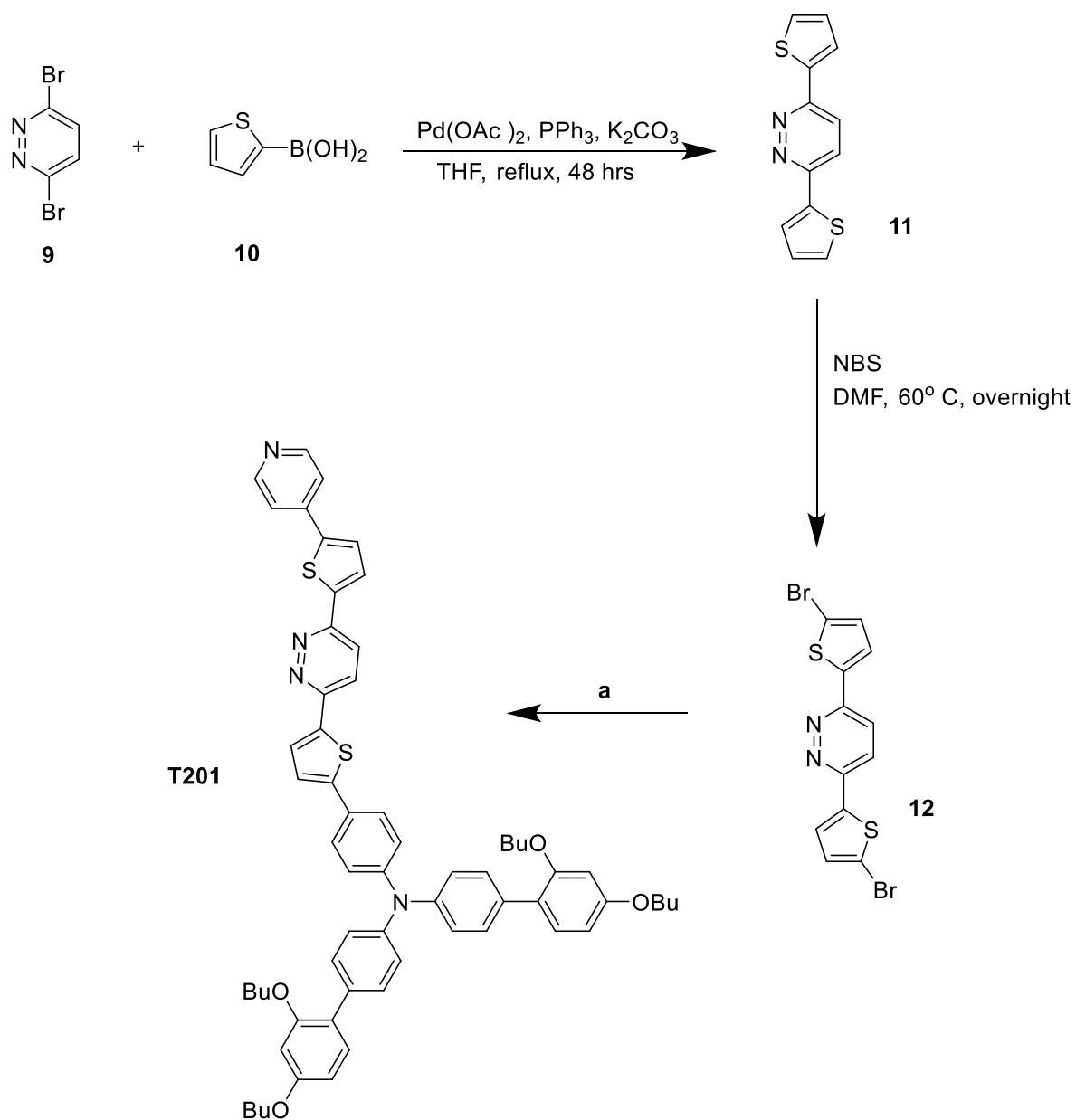
We were successful in synthesizing three novel dyes T200, T201, and T202 using the procedure shown in the synthetic Schemes 9, 10, and 11. The three dyes have in common a pyridine anchoring/electron-withdrawing group and a triphenylamine donor group. In addition, in an attempt to increase the spectral response in the near-IR region as well as improve the molar absorptivities, thienyl groups were incorporated into the molecular skeleton of each of the three sensitizers. The synthesis of T200 started with a Suzuki coupling reaction using a 2-thienylboronic acid to yield the benzothiadiazole product. The second reaction involved an ether cleavage of 1,2-Bis(4-methoxyphenyl)ethanedione followed by an  $S_N2$  reaction using ethylhexylbromide. The purpose of integrating such alkyl chains is to decrease any recombination reaction between the  $TiO_2$  electrons and the electrolyte. The latter product was then reacted with the benzothiadiazole product mentioned above via a condensation reaction. Bromination of the formed product using NBS, followed by two simultaneous Suzuki coupling reaction afforded the desired dye T200. For T201, a different acceptor group was utilized: the reaction also started with a Suzuki coupling reaction of 2-thienylboronic acid and dibromopyridazine to yield 3,6-di(thiophen-2-yl)pyridazine. This product was then brominated using NBS, followed by two subsequent Suzuki coupling reactions. Finally, the

synthesis of T202 consisted of the bromination of the benzothiadiazole product initially produced in the T200 synthetic scheme, followed by two successive Suzuki coupling reactions as for T200 and T201. The structures of the dyes were confirmed by  $^1\text{H}$  NMR,  $^{13}\text{C}$  NMR, and mass spectrometry.

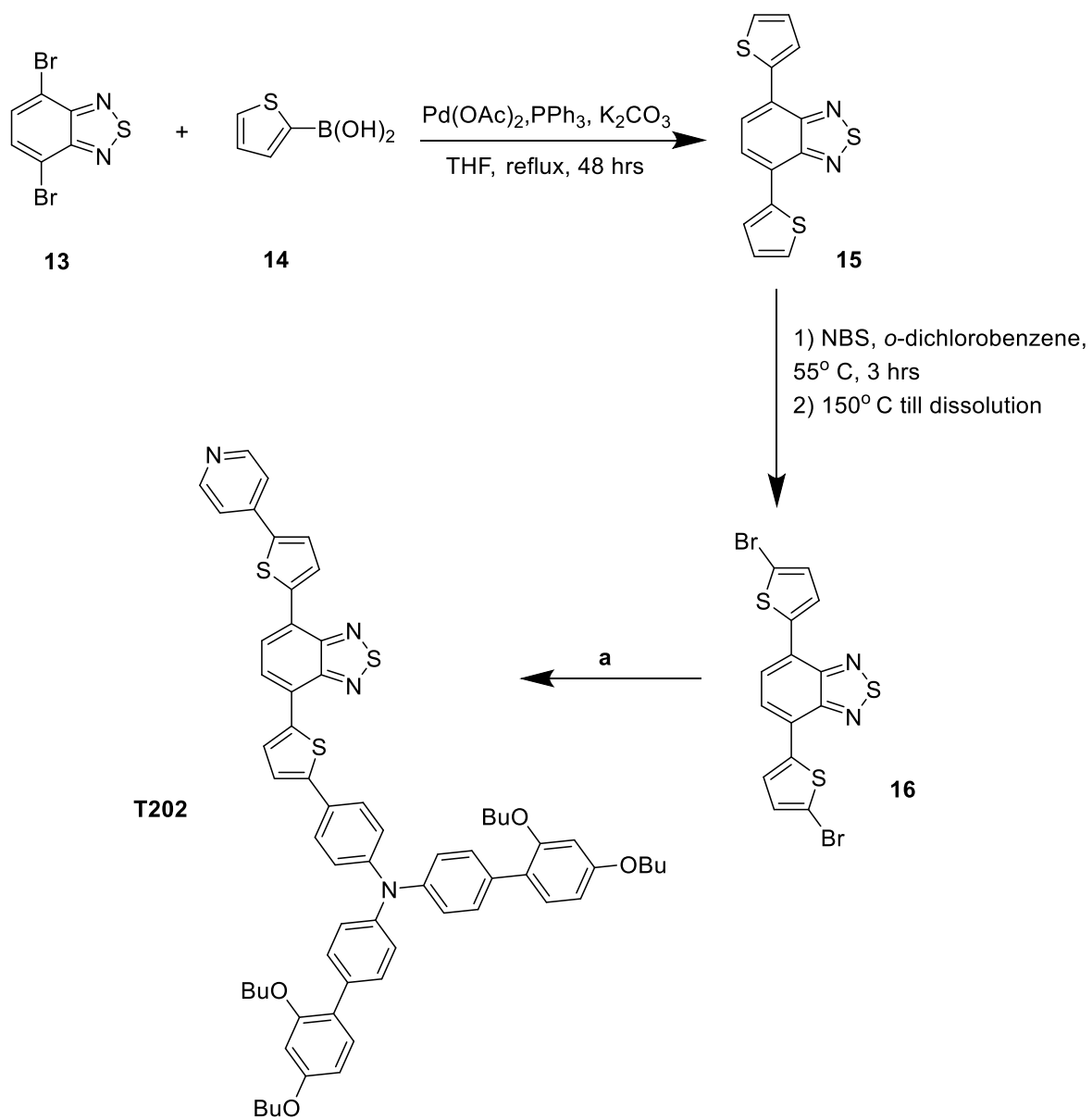




**Scheme 9.** Synthetic scheme of T200 where a) is 4-pyridinyl boronic acid,  $\text{C}_{52}\text{H}_{66}\text{BNO}_2$ ,  $\text{PPh}_3$ ,  $\text{K}_2\text{CO}_3$ , palladium acetate, dioxane: THF:  $\text{H}_2\text{O}$



**Scheme 10.** Synthetic scheme of T201 where a) is 4-pyridinyl boronic acid,  $\text{C}_{52}\text{H}_{66}\text{BNO}_2$ ,  $\text{PPh}_3$ ,  $\text{K}_2\text{CO}_3$ , palladium acetate, dioxane: THF:  $\text{H}_2\text{O}$

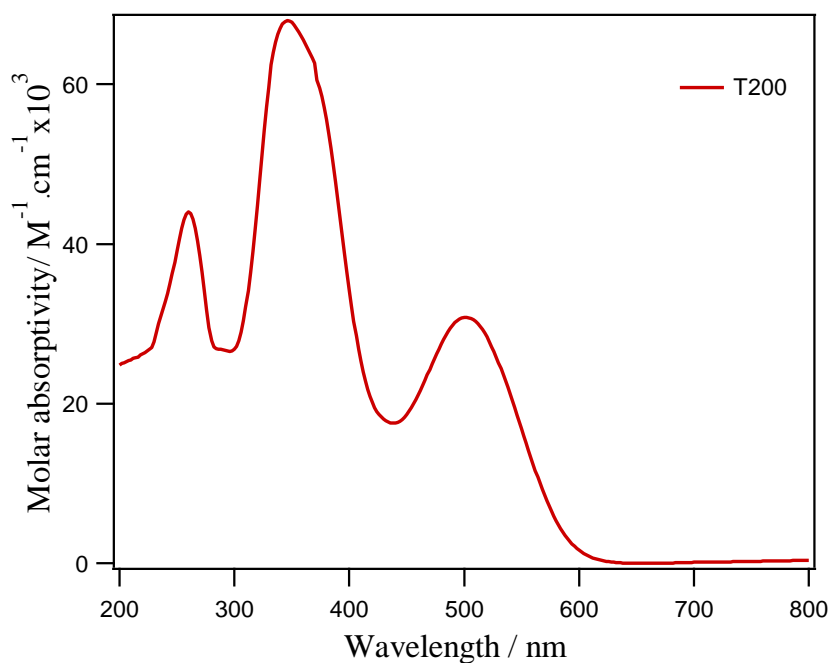


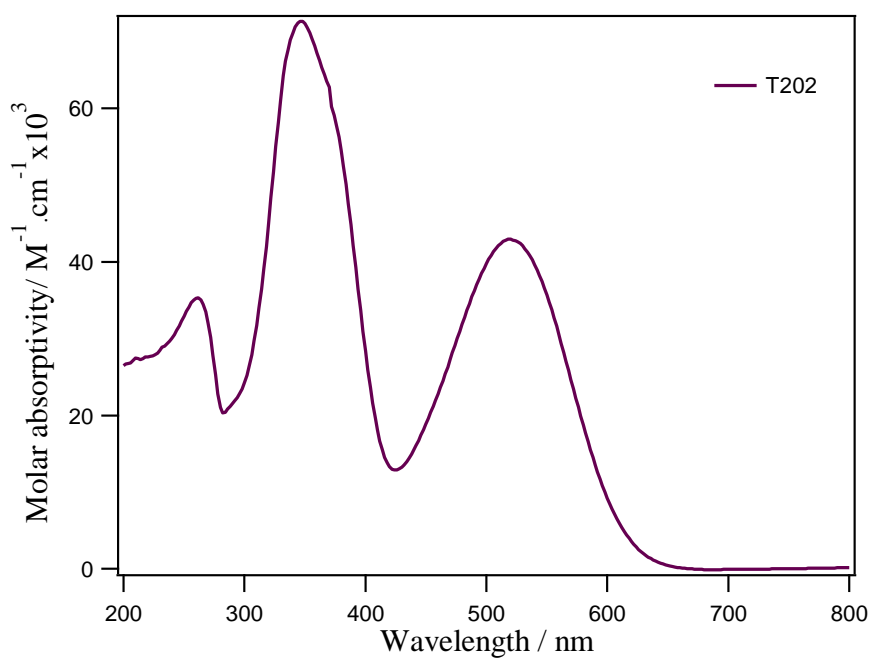
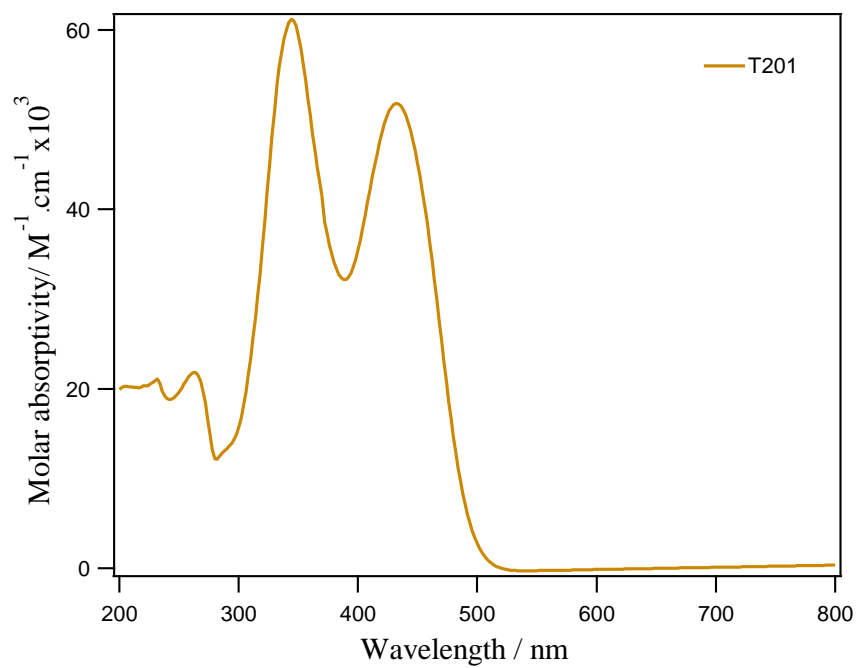
**Scheme 11.** Synthetic scheme of T202 where a) is 4-pyridinyl boronic acid,  $\text{C}_5\text{H}_6\text{BNO}_2$ ,  $\text{PPh}_3$ ,  $\text{K}_2\text{CO}_3$ , palladium acetate, dioxane: THF:  $\text{H}_2\text{O}$

## 3.2 Characterization and Cell Assembly

### 3.2.1 Optical and Electrochemical Properties

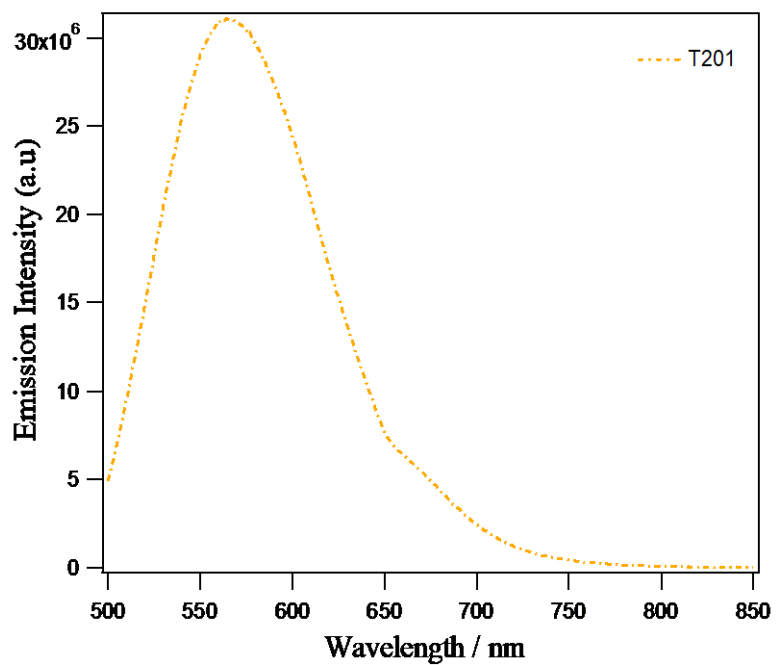
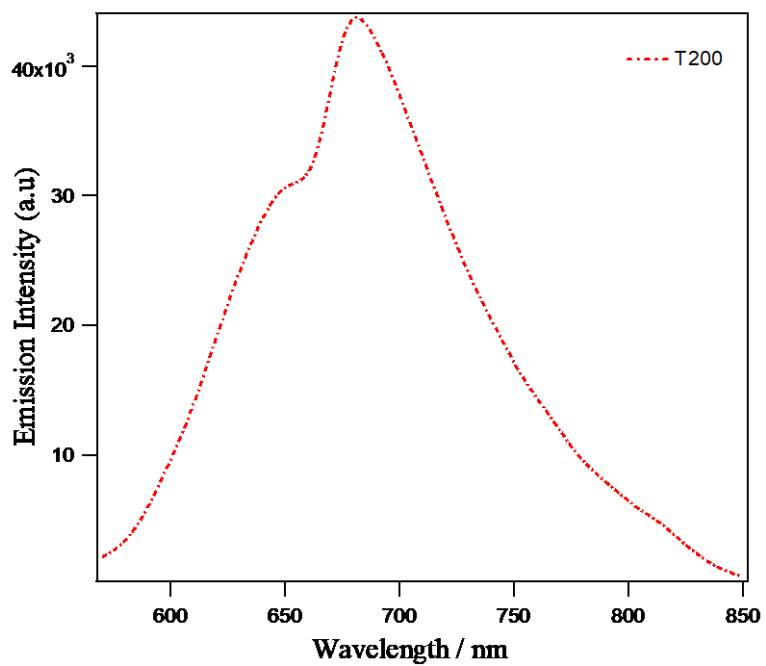
The absorption and emission spectra of T200, T201, and T202 recorded in THF are presented in Figures 6 and 7, and the corresponding data are listed in Table 1. Absorption maxima of 502, 432, and 520 nm were obtained for T200, T201, and T202 respectively, and the corresponding molar absorptivities ( $\epsilon$ ) are  $31000 \text{ M}^{-1} \text{ cm}^{-1}$ ,  $52000 \text{ M}^{-1} \text{ cm}^{-1}$ , and  $43000 \text{ M}^{-1} \text{ cm}^{-1}$ . The emission maxima are at 682, 565, and 705 nm for T200, T201, and T202 respectively.

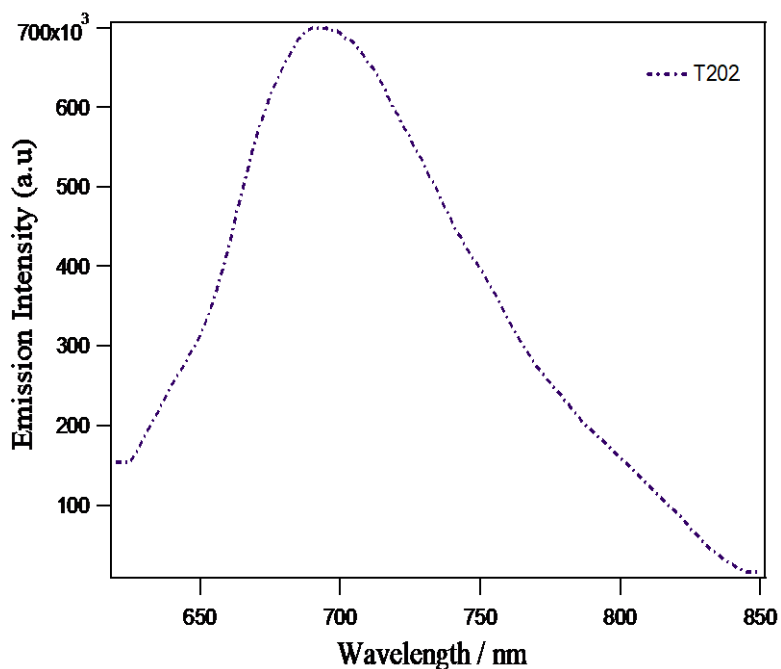




**Figure 6.** The absorbance spectra of T200, T201, and T202 dyes in THF



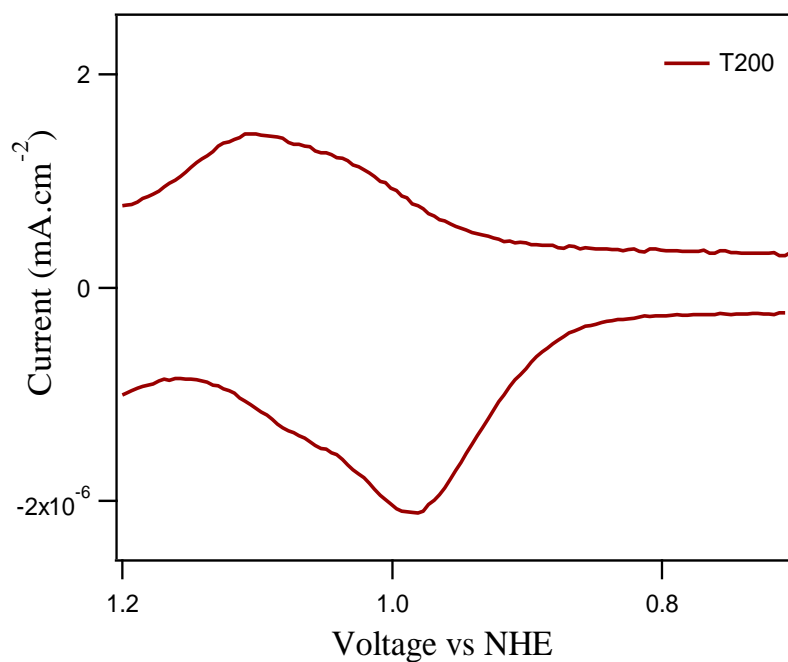




**Figure 7.** The emission spectra of T200, T201, and T202 recorded in THF (excitation wavelengths at 502, 432, and 520 nm, respectively)

Differential pulse voltammetry (DPV) was performed to measure the first oxidation potentials ( $E_{ox}$ ) of the dyes in dimethyl formamide solution (Table 1).  $Ag/Ag^+$  was used as a reference electrode and platinum as a counter electrode, with a scan rate of  $100 \text{ mV}\cdot\text{s}^{-1}$ . The experiments were done with respect to ferrocene oxidation  $Fc/Fc^+$  and calculated vs. NHE by using  $E_{ox}$  of  $Fc/Fc^+$  as  $0.69 \text{ V}$  in DMF, whereby the  $E_{ox}$  for T200, T201, T202 were approximately  $1.04 \text{ V}$ ,  $1.07 \text{ V}$ , and  $1.05 \text{ V}$  vs. NHE, respectively. The differential pulse voltammograms of T200, T201, and T202 are shown in Figure 8. It is crucial to note that the oxidation potentials of the three dyes are more positive than the  $Co^{II}/Co^{III}$  redox potential ( $0.56$  versus NHE) which ensures facile regeneration of the oxidized dyes. The redox potential of the excited dye's state, calculated from the redox

potential ( $E_{ox}$ ) and the optical energy gap ( $E_{0-0}$ ) (measured from the intersection of the absorption and emission bands) by  $E_{ox}-E_{0-0}$ , are adequately more negative than the TiO<sub>2</sub> conduction band edge  $E_{CB}$  (-0.5 versus NHE), promoting thermodynamically favorable electron injection into the TiO<sub>2</sub>.



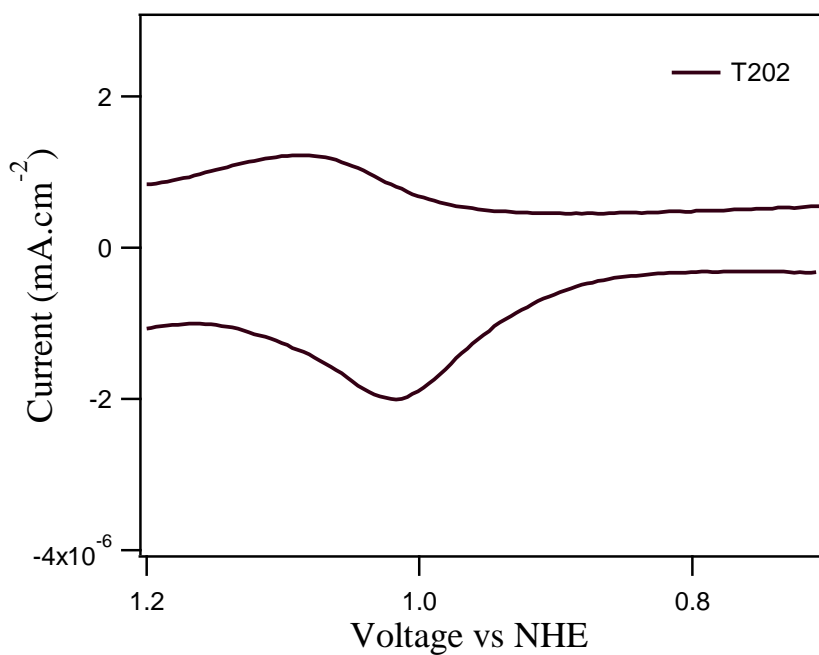
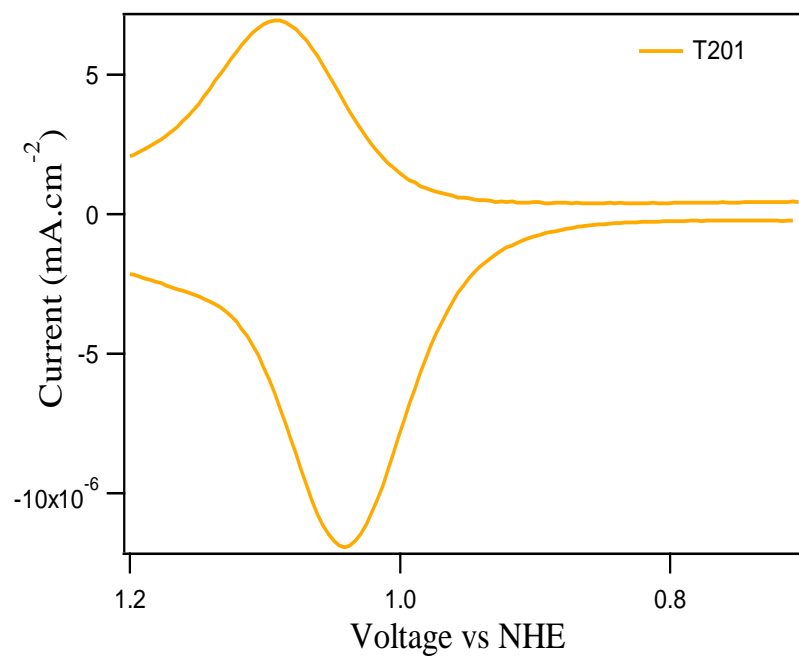


**Figure 8.** Differential pulse voltammograms of T200, T201, and T202 in DMF in 0.1 M TBAPF<sub>6</sub> recorded at a scan rate of 100 mV.s<sup>-1</sup>

**Table 1.** Optical and electrochemical properties of T200, T201, and T202

Dye	Abs. ( $\epsilon \times 10^4 \text{ M}^{-1} \text{ cm}^{-1}$ )	$\lambda_{\text{em}} (\lambda_{\text{ex}})$ , nm	$E_{\text{ox}}$ , V vs NHE	$E_{\text{ox}} - E_{0-0}$ V vs NHE
T200	346 (6.8), 502 (3.1)	682 (502)	1.04	-1.07
T201	344 (6.1), 432 (5.2)	565 (432)	1.07	-1.44
T202	350 (7.1), 520 (4.3)	705 (520)	1.05	-1.08

### 3.2.2 Computational Methods

In order to gain further insight into the electronic structure of T200, T201, and T202, time-dependent density functional theory (TD-DFT) calculations were performed at the CAM-B3LYP level for geometry optimization. The frontier molecular orbitals (MO) energies of the sensitizers are given in Figure 9. For T200, the highest occupied molecular orbital (HOMO) lies at  $-4.73$  eV, and is delocalized over the triphenylamine (TPA) moiety. The HOMO-1, lying at  $0.59$  eV below the HOMO, is a delocalized orbital over the molecule. The lowest unoccupied molecular orbital (LUMO), lies at  $-2.43$  eV. It is evident that there is no contribution from the donor triphenylamine group, and the electron density is shifted towards the far end of the molecule i.e. the acceptor/anchoring groups. The LUMO+1 is located at  $0.87$  eV above the LUMO, and is localized mainly on the pyridine group. Figure 10 shows the isodensity plots of the frontier molecular orbitals MOs of dyes T200, T201, and T202.

As for dye T201, the HOMO, lying at -4.82 eV, is a delocalized  $\pi$  orbital lying across the entire electron donating TPA group. The HOMO-1 is 0.78 eV below the HOMO level, and is distributed over the entire molecule. While the LUMO, lying at -2.29 eV, is mainly localized over the diazine acceptor, and the pyridine anchoring group. The LUMO+1, lying around 0.69 eV above the LUMO level, is located mainly across the thiophene and diazine groups, with a less electron density on the pyridine moiety.

For the dye T202, the HOMO is located at -4.76 eV, and distributed across the TPA group, similarly to the 2 previous dyes. The HOMO-1, lying at 0.63 eV below the HOMO, has its electron density distributed across the entire molecule's frame. The LUMO is located at -2.79 eV, and consists of a delocalized MO orbital over the benzothiadiazole group, excluding the pyridine moiety. Lying at 1.12 eV above the LUMO level, the LUMO+1 has its electron density mainly on the thiophene and pyridine groups.

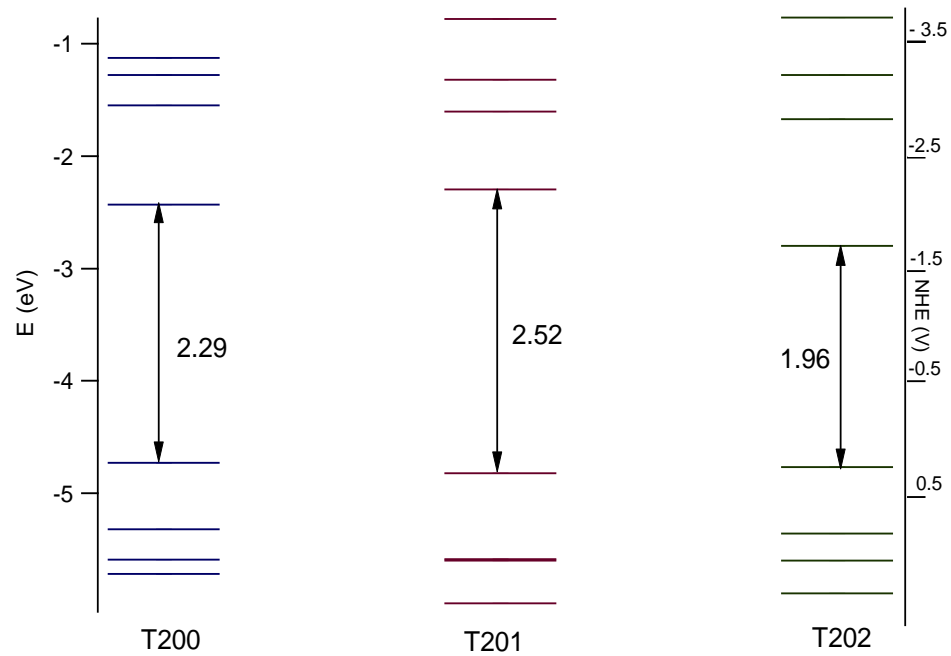


**Figure 9.** The frontier molecular orbital energies of the dyes T200, T201, and T202

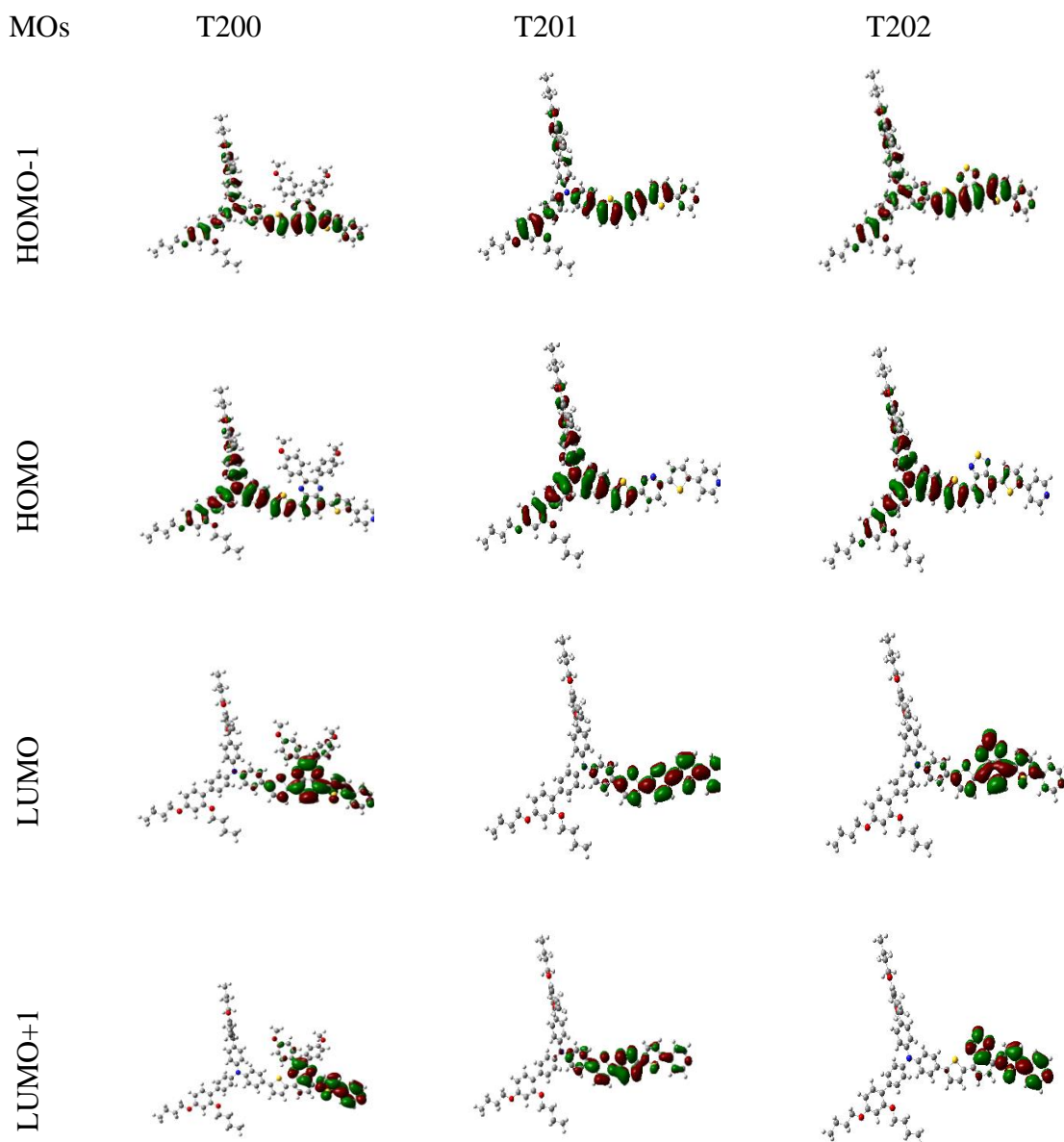


**Figure 10.** Isodensity plots of the frontier orbitals of the dyes T200, T201, and T202

The computed ground-state vertical excitation energies with oscillator strength ( $f$ ) more than 0.02 are shown in Table 2-4. Due to the fact that only absorption in the visible and near-UV region is of importance for photon-to-current conversion, only singlet to



singlet transitions oscillator strength ( $f$ ) greater than 0.02, and wavelengths above 300 nm were listed.

**Table 2.** Computed excitation energies, assignments, and oscillator strengths for the dye T200

Dye	TDDFT excitation energies, nm	Oscillator strength <sup>a</sup>	Assignment
<b>T200</b>	460.9	1.4714	HOMO→LUMO (56%), HOMO-1→LUMO (35%)
	368.1	0.2592	HOMO-3→LUMO (46%), HOMO-1→LUMO (18%), HOMO→LUMO+3 (7%), HOMO→LUMO (6%)
	347.6	0.3960	HOMO-3→LUMO (30%), HOMO-1→LUMO (15%), HOMO→LUMO+2 (12%), HOMO-4→LUMO (10%), HOMO→LUMO (6%)
	325.1	0.9607	HOMO-1→LUMO+1 (22%), HOMO→LUMO+3 (19%), HOMO→LUMO+1 (17%), HOMO→LUMO+2 (8%), HOMO→LUMO (6%), HOMO-5→LUMO (5%)
	312.3	0.0593	HOMO→LUMO+2 (19%), HOMO→LUMO (18%), HOMO-1→LUMO+1 (15%), HOMO-1→LUMO (13%), HOMO-1→LUMO+2 (7%), HOMO→LUMO+1 (6%)
	311.2	0.9922	HOMO→LUMO+4 (72%), HOMO-1→LUMO+4 (13%)
	303.0	0.2010	HOMO-1→LUMO+2 (25%), HOMO→LUMO+3 (21%), HOMO-1→LUMO+1 (6%)

<sup>a</sup> Only bands with oscillator strength  $f \geq 0.02$  are listed.

**Table 3.** Computed excitation energies, assignments, and oscillator strengths for the dye T201

Dye	TDDFT excitation energies, nm	Oscillator strength <sup>a</sup>	Assignment
<b>T201</b>	407.7	2.2502	HOMO→LUMO (49%), HOMO-1→LUMO (26%), HOMO→LUMO+1 (11%)
	336.1	0.1362	HOMO-1→LUMO (28%), HOMO-3→LUMO (23%), HOMO→LUMO+1 (21%), HOMO→LUMO+4 (7%)
	309.5	0.9566	HOMO→LUMO+3 (78%)
	304.6	0.0578	HOMO-1→LUMO+1 (25%), HOMO→LUMO+2 (15%), HOMO→LUMO+1 (15%), HOMO-1→LUMO+2 (13%), HOMO→LUMO (11%)

<sup>a</sup> Only bands with oscillator strength  $f \geq 0.02$  are listed.

**Table 4.** Computed excitation energies, assignments, and oscillator strengths for the dye T202

Dye	TDDFT excitation energies, nm	Oscillator strength	Assignment
<b>T202</b>	521.4	1.4326	HOMO→LUMO (57%), HOMO-1→LUMO (37%)
	380.5	0.0366	HOMO-1→LUMO (41%), HOMO→LUMO (25%), HOMO-3→LUMO (15%), HOMO→LUMO+2 (11%)
	337.2	1.2237	HOMO→LUMO+2 (39%), HOMO-1→LUMO+1 (19%), HOMO→LUMO+1 (18%)
	310.3	0.2662	HOMO→LUMO+3 (26%), HOMO-4→LUMO (15%), HOMO-3→LUMO (14%), HOMO-1→LUMO+1 (6%), HOMO-6→LUMO (6%)
	310.0	0.7515	HOMO→LUMO+3 (45%), HOMO-4→LUMO (9%), HOMO-1→LUMO+3 (9%), HOMO-3→LUMO (8%)

### 3.3 Photovoltaic Performance and IPCE Spectra

#### 3.3.1 Individual Dyes

The performance of the three sensitizers was assessed by fabricating liquid DSCs using a cobalt tris(bipyridyl) electrolyte system (containing 0.6 M TBP), for which the corresponding *IV* curves measured under standard AM 1.5 conditions are shown in Figure 11. The corresponding photovoltaic parameters are summarized in Table 5. The DSSC based on T202 as a sensitizer showed the highest photovoltaic performance with a  $J_{SC} = 13.38 \text{ mA}\cdot\text{cm}^{-2}$ , a  $V_{OC} = 828 \text{ mV}$ , a fill factor FF of 0.61, and an overall efficiency  $\eta$  of 6.8%. An overall PCE% value of 5.4% ( $J_{SC} = 11.8 \text{ mA}\cdot\text{cm}^{-2}$ ,  $V_{OC} = 756 \text{ mV}$ , FF = 0.61) was obtained for a DSSC sensitized with T200. The pyridazine acceptor based dye T201 gave the poorest photovoltaic performance of  $8.0 \text{ mA}\cdot\text{cm}^{-2}$  for short-circuit current,  $828 \text{ mV}$  for open-circuit voltage, a 0.61 fill factor, and a mediocre efficiency of 4.0 %.

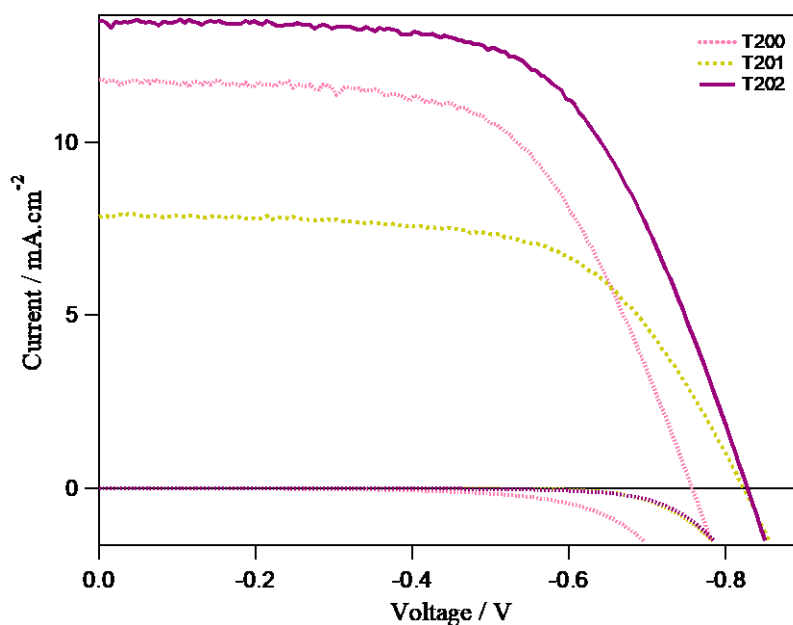


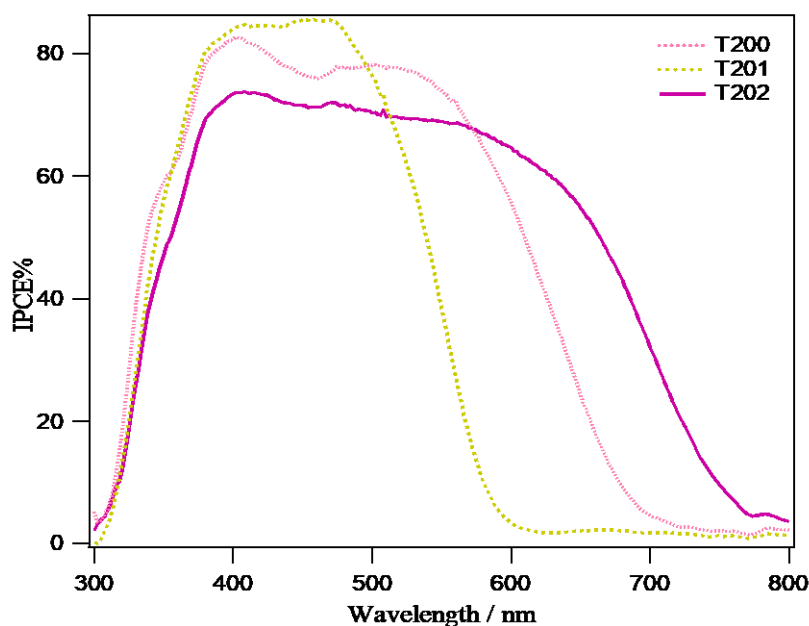
**Figure 11.** Photocurrent–voltage characteristics of DSSCs sensitized with T200, T201, and T202, and the corresponding dark currents

**Table 5.** Photovoltaic Parameters of T200, T201, and T202

Dye	$J_{SC}$ (mA.cm <sup>-2</sup> )	$V_{OC}$ (mV)	FF	PCE (%) <sup>a</sup>
T200	11.8	751	0.61	5.4
T201	8.0	828	0.61	4.0
T202	13.4	823	0.61	6.8

<sup>a</sup> Measured under 100 mW.cm<sup>-2</sup> simulated AM1.5 spectrum with an active area 0.5 x 0.5 cm<sup>2</sup> and a black mask (0.6 x 0.6 cm<sup>2</sup>); the electrolyte consisted of 0.25 M Co(II), 0.06 M Co(III), 0.1 M LiClO<sub>4</sub> and 0.6 M TBP

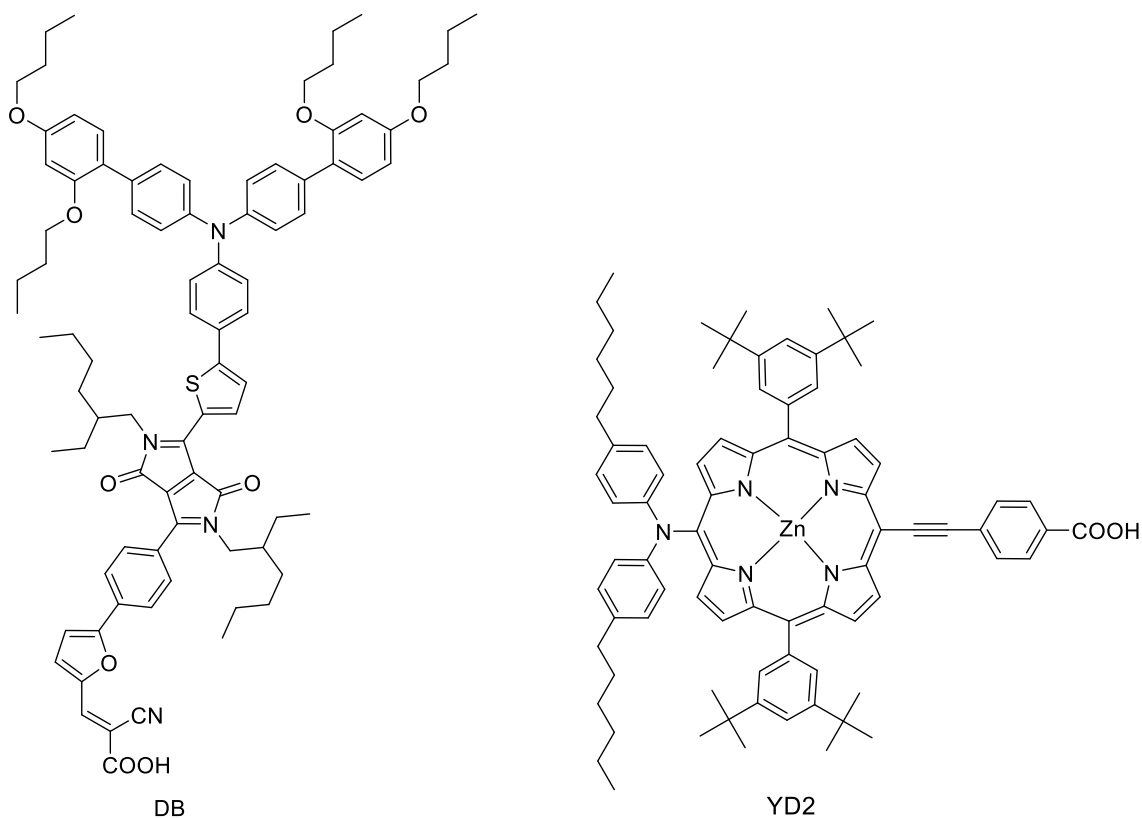
Action spectra of monochromatic incident to photon current efficiency (IPCE%) for a DSSC based on TiO<sub>2</sub> electrode, pyridine dyes, and Co<sup>2+</sup>/ Co<sup>3+</sup> electrolyte is shown in Figure 12. The onset wavelength of the IPCE spectrum for a DSSC based on T201 was 610 nm, whereby IPCE values of around 85 % were recorded in the range of 350 to 550 nm. With a starting wavelength of 770 nm, a maximum of around 72 % at 400 nm was observed for T202-based solar cells. T200 demonstrated a 82 % IPCE% at 400 nm, with a starting wavelength of 700nm.

**Figure 12.** IPCE % spectra of DSSCs sensitized with T200, T201, and T202

### 3.4 Co-adsorption of Complementary Dyes

#### 3.4.1 Co-sensitization of T202 with DB and YD2

In order to prove the hypothesis that no competition was perceived when mixing dyes with different binding sites to the TiO<sub>2</sub> semiconductor, T202 was co-adsorbed with two commercially available dyes YD2 and Dynamo Blue (DB). As explained previously, T202 contains a pyridine anchoring group which favorably binds to the Lewis acid sites of the metal oxide, while DB and YD2 contain a carboxylic acid anchor which fixes to the semiconductor's Brønsted acid sites. The molecular structures of DB and YD2 are given in Scheme 12.



**Scheme 12.** The molecular structures of YD2 and DB dyes

### 3.4.1.1 Dye Loading Measurements

Before solar cell testing, 6  $\mu\text{m}$   $\text{TiO}_2$  electrodes were immersed in 0.2 mM solution of T202, 0.2 mM solution of YD2, and a mixture of T202 and YD2 bearing equal concentrations in THF: EtOH for 24 hours, in order to study the dye loading amounts of the co-sensitized films. The UV/Vis spectra of the dyes adsorbed on  $\text{TiO}_2$  films are shown in Figure 13.

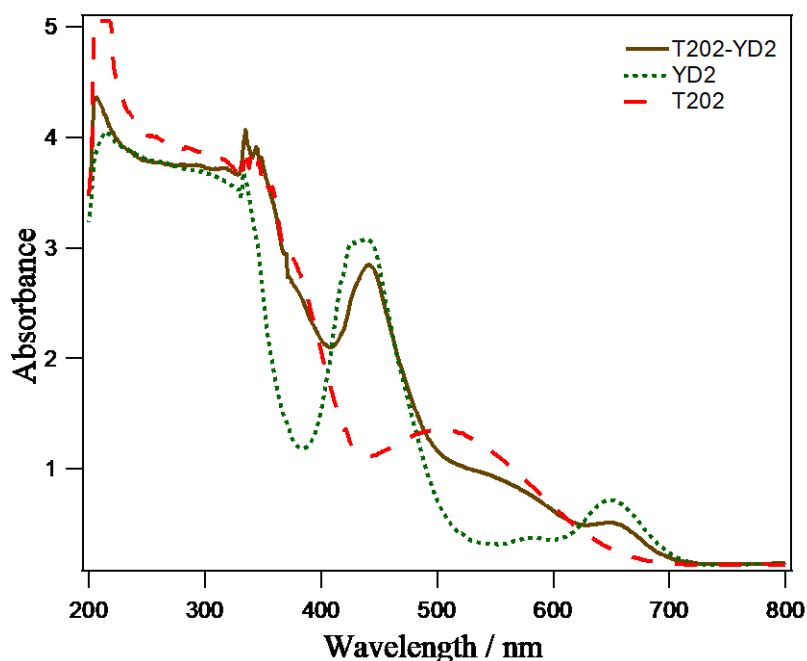


**Figure 13.** The absorbance spectra of T202, YD2, and T202-YD2 on  $\text{TiO}_2$  films

To allow the desorption of the dye molecules, dye-adsorbed  $\text{TiO}_2$  electrodes were dipped in an alkaline solution of THF:EtOH:H<sub>2</sub>O for a couple of minutes. A plot of the absorbance as a function of wavelength would allow the calculation of the dye loading quantities by measuring the maximum absorbance in each curve. Table 6 and Figure 14

show the dye loading amounts and absorbance spectra of desorbed TiO<sub>2</sub> films for T202, YD2, and mixed T202-YD2.

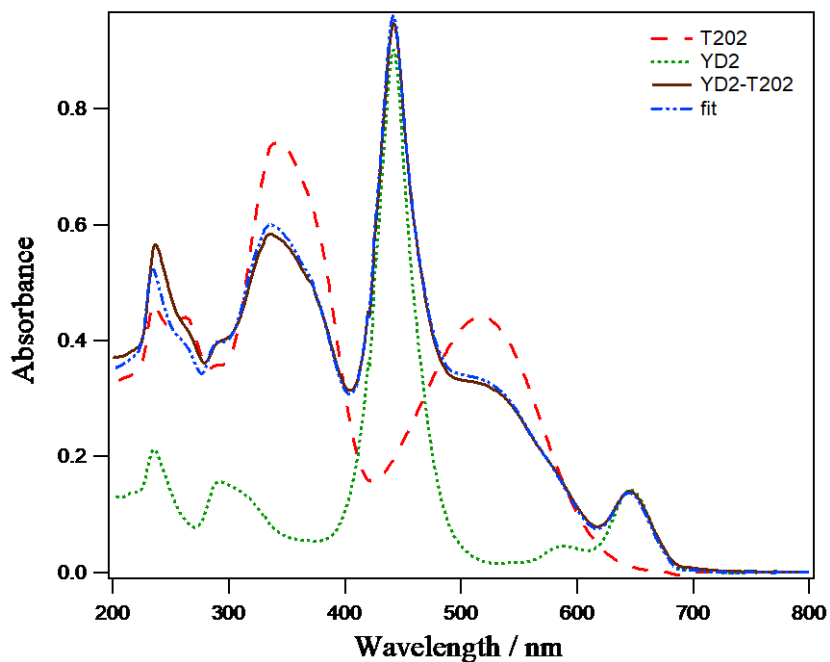


**Figure 14.** The absorbance spectra of TiO<sub>2</sub> desorbed films of YD2, YD2—T202, and T202 as a function of wavelength

**Table 6.** The dye loading of T202 and YD2 for pure and co-adsorbed TiO<sub>2</sub> films<sup>a</sup>

Dye Concentration in Solution	nT202 (mol)	nYD2 (mol)	Total dye loading (mol)
T202 (0.2 mM)	$1.0 \times 10^{-7}$	0	$1.0 \times 10^{-7}$
YD2 (0.2mM)	0	$4.3 \times 10^{-8}$	$4.3 \times 10^{-8}$
T202(0.2 mM) + YD2 (0.2mM)	$7.2 \times 10^{-8}$	$3.9 \times 10^{-8}$	$11.1 \times 10^{-8}$

<sup>a</sup> A 6 μm TiO<sub>2</sub> film of 2.56 cm<sup>2</sup> area was used. Each measurement was done in duplicate.

Experimental fitting of the T202-YD2 absorbance spectra would provide us with the percentage of adsorbed T202 and YD2 amounts compared to the non-coadsorbed ones.

These coefficients turned out to be 0.72 for T202, and 0.91 for YD2. The dye loading measurements of the co-sensitized T202-YD2 film ( $7.2 \times 10^{-8}$  mol for T202, and  $3.9 \times 10^{-8}$  mol for YD2) adsorbed to  $1.6 \times 1.6 \text{ cm}^2$  of  $6 \mu\text{m}$   $\text{TiO}_2$  film, visibly show that, as predicted, the above mentioned dyes do not compete for the same site on the semiconductor.

As mentioned previously,  $6 \mu\text{m}$   $\text{TiO}_2$  electrodes were immersed in a dye bath having a concentration of 0.2 mM for T202, 0.03 mM for DB, and a mixture of the same concentrations as above for T202 and DB for 24 hours. The UV/Vis spectra of the dyes adsorbed on  $\text{TiO}_2$  films are shown in Figure 15.

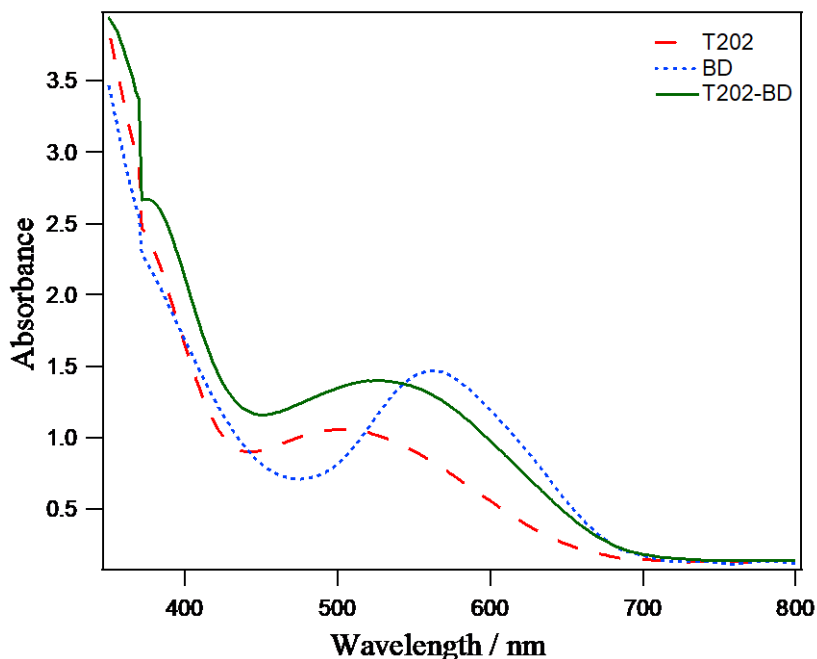


**Figure 15.** The absorbance spectra of T202, DB, and T202-DB on  $\text{TiO}_2$  films

This was followed by the desorption of all the sensitized films by immersing them in a 0.01M KOH solution of THF:EtOH:H<sub>2</sub>O for a while. Dye loading measurements were



completed by plotting the absorbance of the desorbed films as a function of the wavelength, and using the maximum absorbance of the curves to calculate the dye loading amounts for sole and co-sensitized films. Table 7 and Figure 16 show the dye loading amounts and absorbance spectra of desorbed TiO<sub>2</sub> films for T202, DB, and mixed T202-DB.

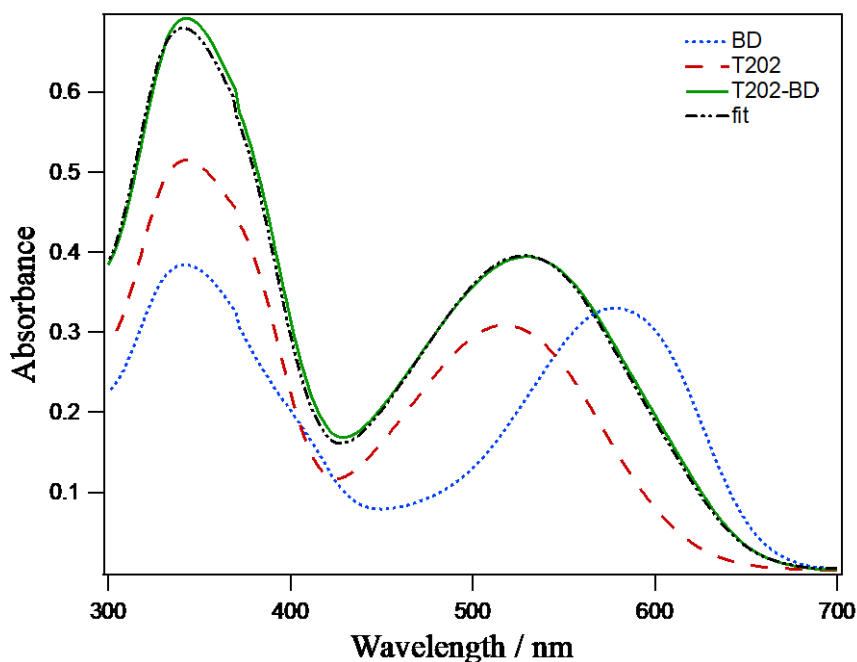


**Figure 16.** The absorbance spectra of TiO<sub>2</sub> desorbed films of DB, DB—T202, and T202 as a function of wavelength

**Table 7.** The dye loading of T202 and DB for pure and co-adsorbed TiO<sub>2</sub> films<sup>a</sup>

Dye Concentration in Solution	nT202 (mol)	nDB (mol)	Total dye loading (mol)
T202 (0.2 mM)	$7.2 \times 10^{-8}$	0	$7.2 \times 10^{-8}$
DB (0.03 mM)	0	$9.7 \times 10^{-8}$	$9.7 \times 10^{-8}$
T202(0.2 mM) + DB (0.03 mM)	$7.6 \times 10^{-8}$	$3.4 \times 10^{-8}$	$11 \times 10^{-8}$

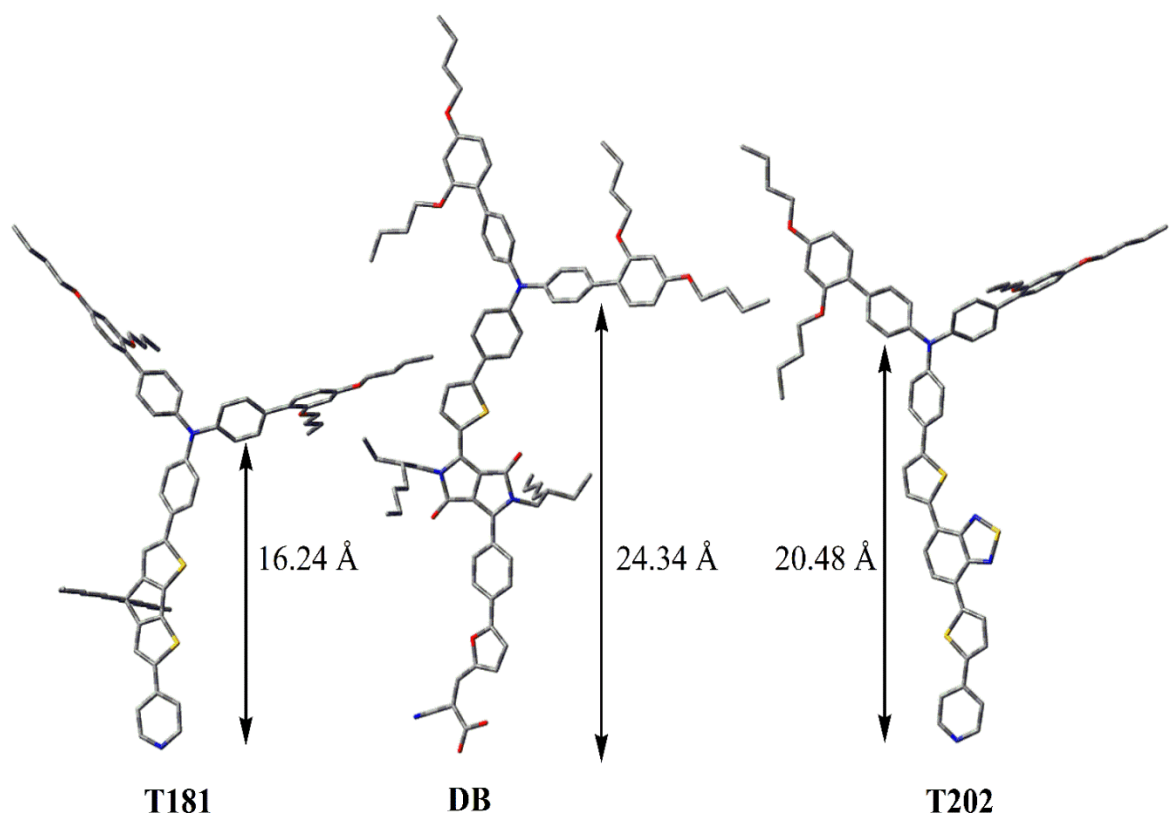
<sup>a</sup> A 6 μm TiO<sub>2</sub> film of 2.56 cm<sup>2</sup> area was used. Each measurement was done in duplicate.

Spectra fitting of the desorbed solutions from the co-sensitized films allowed us to obtain the coefficients of adsorbed T202 and DB, which turned out to be 1.05 for the former, and 0.35 for the latter. This means that, while 100 % of T202 was adsorbed in the co-sensitized film, the amount of DB adsorbed was decreased by 65 % with respect to the single-sensitized DB film.<sup>106</sup> The dye loading amounts for the co-sensitized T202-DB film are  $7.6 \times 10^{-8}$  mol for T202, and  $3.4 \times 10^{-8}$  mol for DB.

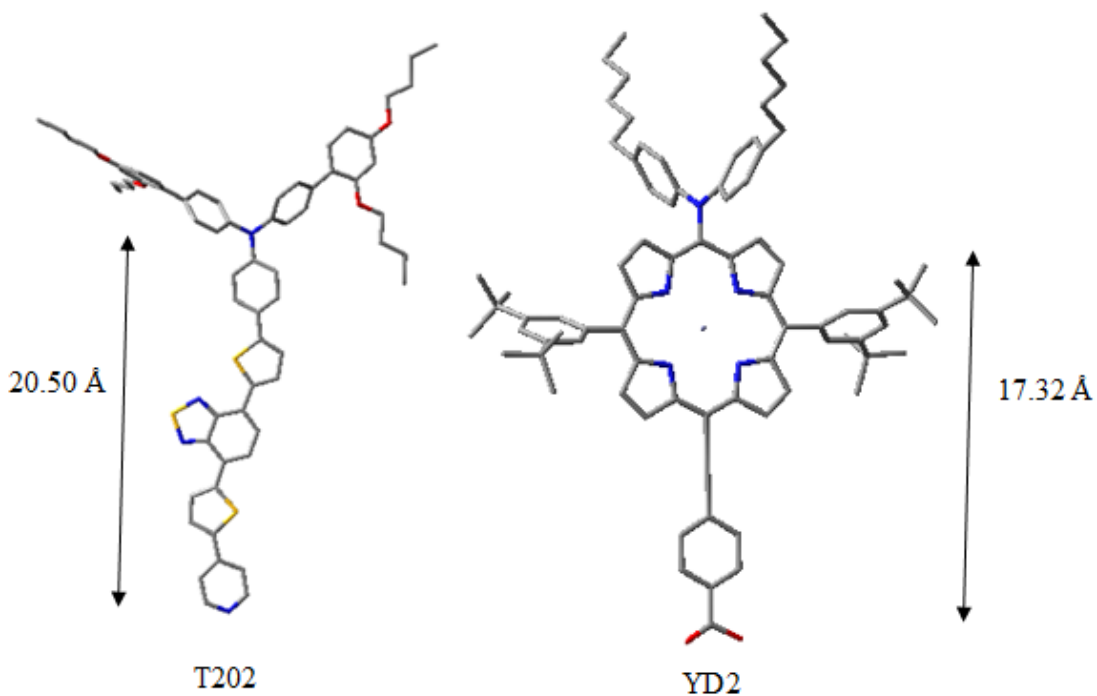
#### 3.4.1.2 Effect of Dye Size on Co-adsorption

In a previous work, the co-adsorption of a pyridyl-based dye T181 with a carboxylic acid-based one (Dynamo Blue DB) was successfully performed by Ghaddar *et al.* and it was shown that the total dye loading was equal to the sum of the two individual dyes.<sup>106</sup> Density functional theory (DFT) calculations were performed, and the dyes' respective optimized geometries and their relative sizes demonstrated that the bulky donor group of T181 can adequately fit within the void right below the DB donor group.

To further verify our speculations concerning the relevance between lower dye loadings and sensitizer structural size, the optimized structures of T202, YD2, and DB are shown in Scheme 13 and 14).



**Scheme 13.** Calculated relative sizes of the geometry optimized T202, T181, and DB dyes



**Scheme 14.** Calculated relative sizes of the geometry optimized T202 and YD2 dyes

The calculated vertical distance between the N atom of the triphenyl amine donor group and the N atom of the pyridyl moiety is 20.50 Å for T202, and the distance between the N atom of the diphenylamine group and the O atom of the carboxylic acid is 17.32 Å for YD2. It is evident from their respective geometries that, even though both dyes have bulky donor groups, we speculate that the zinc-porphyrin moiety in YD2 was to averagely fit in between the empty spaces of T202— a case which was not observed upon co-sensitizing T202 with DB. The calculated vertical distance between the N atom of the triphenylamine group and the O atom of the carboxylic acid moiety is 24.34 Å, roughly the same size as T202. Therefore, we assume that the reason for the lower loading amount of

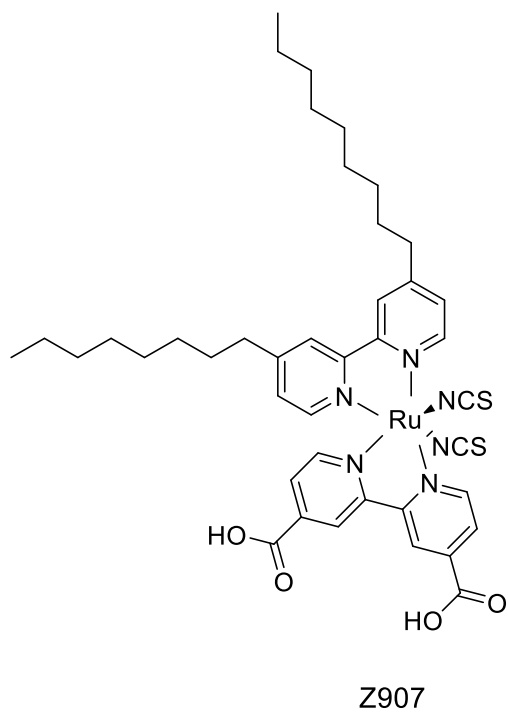
DB in T202-DB co-sensitized cells was probably due to the inability of the T202 sensitizer to properly fit in the grooves of the DB dye. An increase in the concentration of DB above 0.03 M is detrimental and therefore was avoided due to its tendency to form aggregation.

Based on these findings, it is clearly evident that other than complementary light absorption properties, the selection of co-sensitizers undoubtedly relies on the respective molecular sizes/geometries.<sup>107</sup>

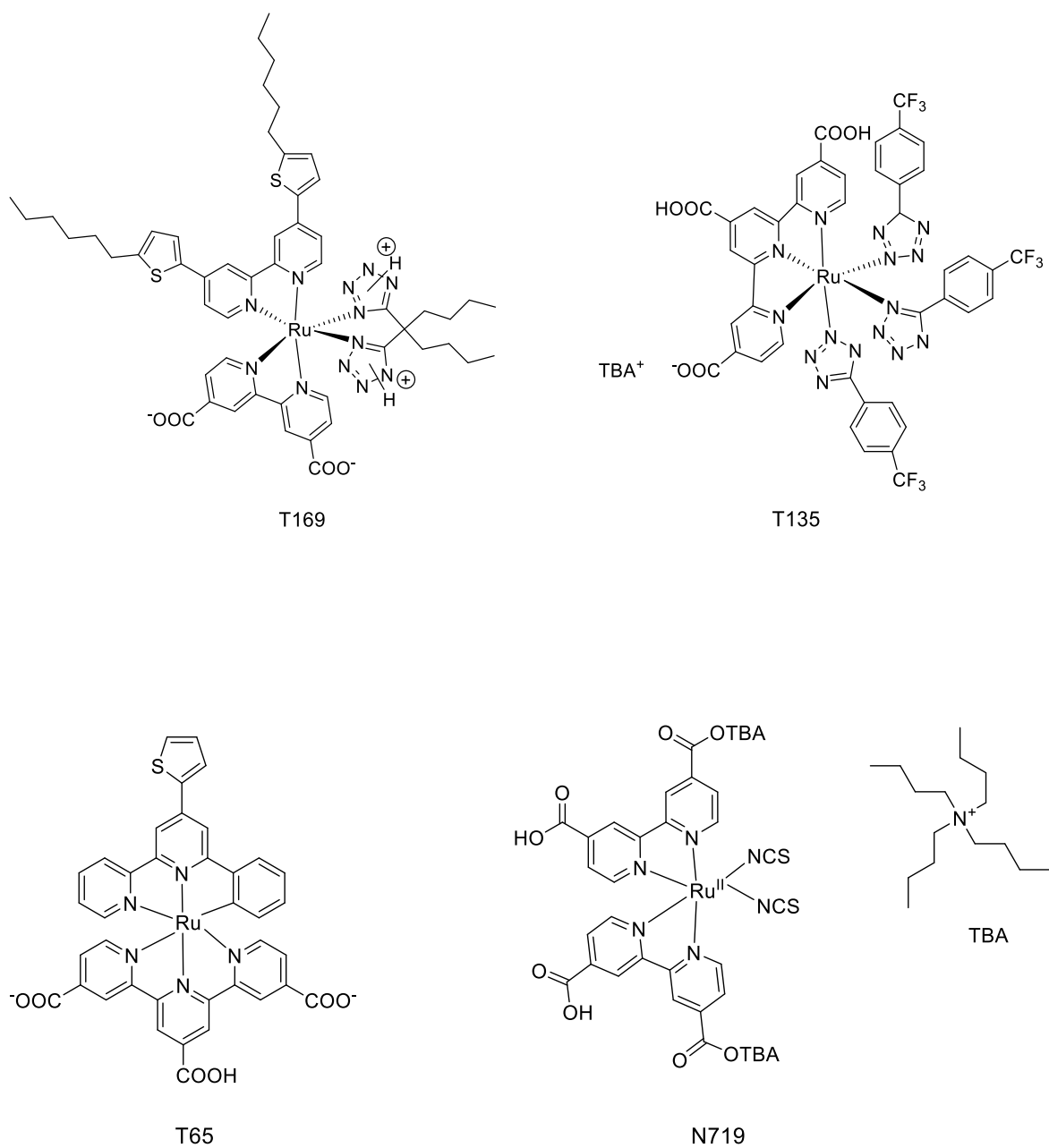
### ***3.4.2 Co-sensitization of T201 with Ruthenium (II) Dyes***

The co-sensitization of T201 with several ruthenium-based dyes was performed in order to study the performance of metal-based dyes in a cobalt redox shuttle. The performance of Ru(II) dyes varies with Co(II)/Co(III) redox mediators; the prototypical N719 dye for instance delivers a dramatically low photovoltaic efficiency of 2 % while in conjunction with a cobalt-based system, however, the Z907 dye (Scheme 15) gave higher and similar performance with both iodine and cobalt-based electrolytes.<sup>108</sup> This can be attributed to the molecular structure of the respective dyes; N719 has two carboxylate groups, which, along with the oxidized Co (III) species, have the ability of forming ion pairs. This increases the probability of recombination of the TiO<sub>2</sub> electrons with the Co (III), thus decreasing the DSSC's photovoltage, photocurrent, as well as the charge collection efficiency. Contrastingly, the presence of long alkyl chains at the vicinity of the Z907 dye decreases this interception by acting as a blocking-layer, and therefore preventing the approach of the oxidized redox species to the semiconductor surface. For this purpose, we aim to form dye cocktails of ruthenium and organic dyes in order to increase the device's photovoltage, and suppress recombination efficiencies.

The selected dyes for co-adsorption with T201 were T169, T135, T65, and the commercially available N719 (molecular structures are given in Scheme 16).



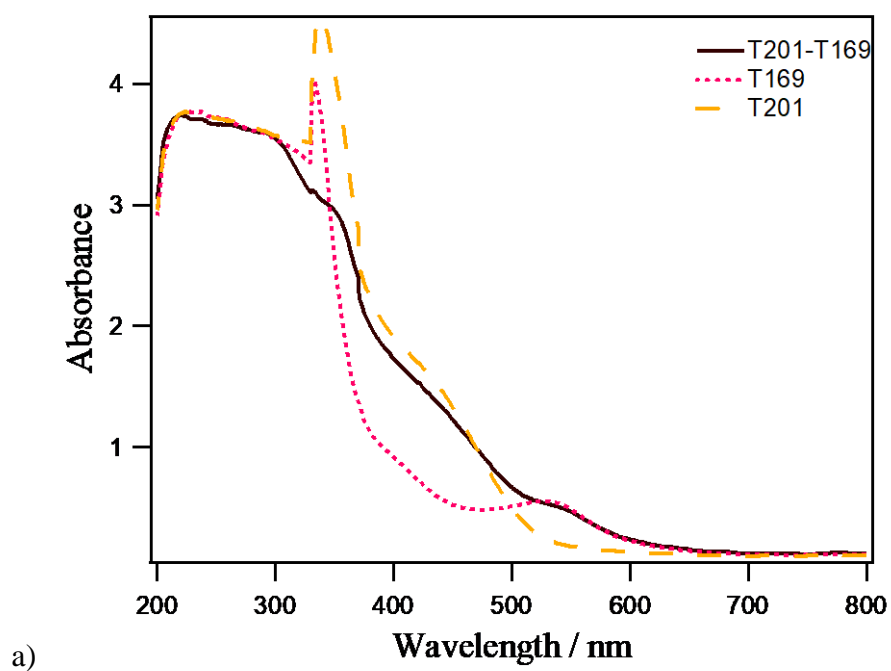
**Scheme 15.** Molecular structure of Z907 dye



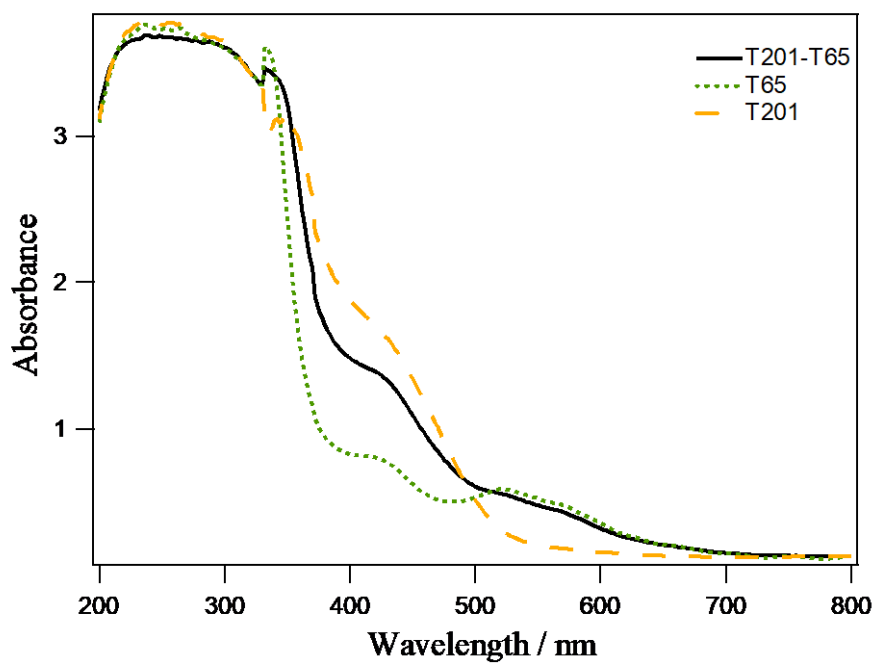
**Scheme 16.** Molecular structures of the chosen Ru (II) dyes

### 3.4.2.1 Dye Loading Measurements

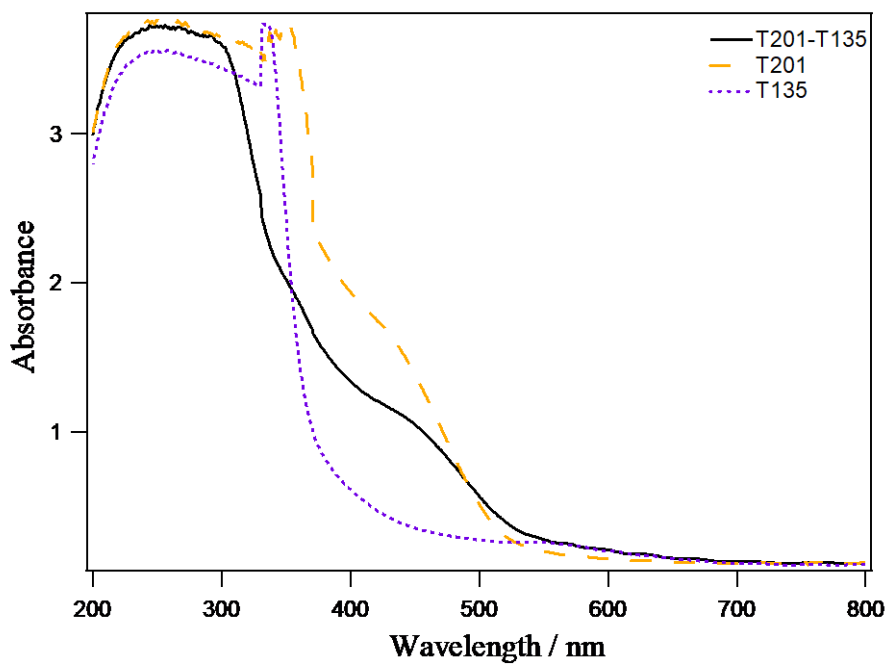
As performed in the previous section, the dye loading amounts of pure and co-sensitized T201 films for each of the T169, T135, T65 and N719 ruthenium dyes were studied by immersing 4  $\mu\text{m}$  films in a 0.2 mM solution of T201, 0.2 mM T65, 0.3 mM N719, and 0.1 mM for each of T169 and T135. The UV-Vis spectra of the  $\text{TiO}_2$ -adsorbed dyes are given in Figure 17.







b)



c)

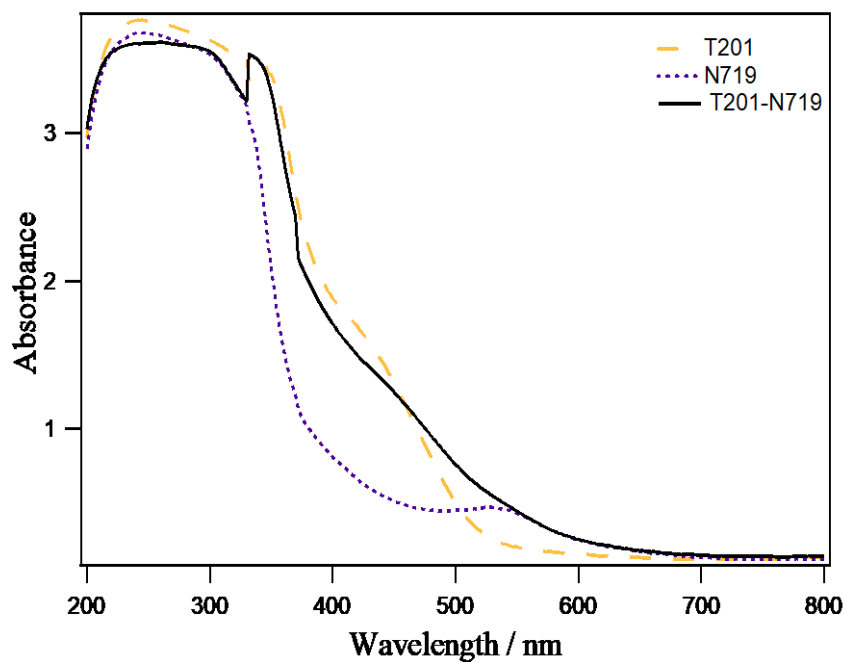
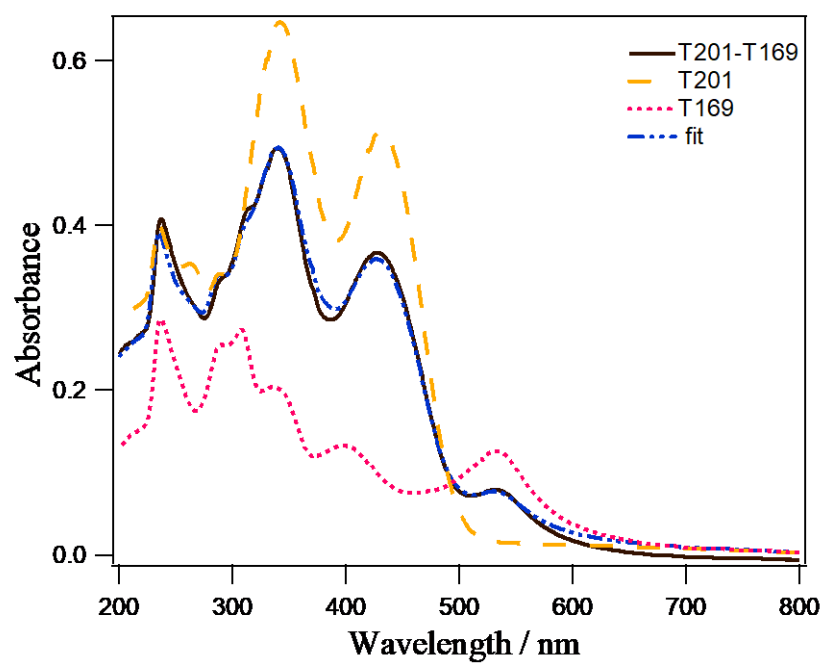
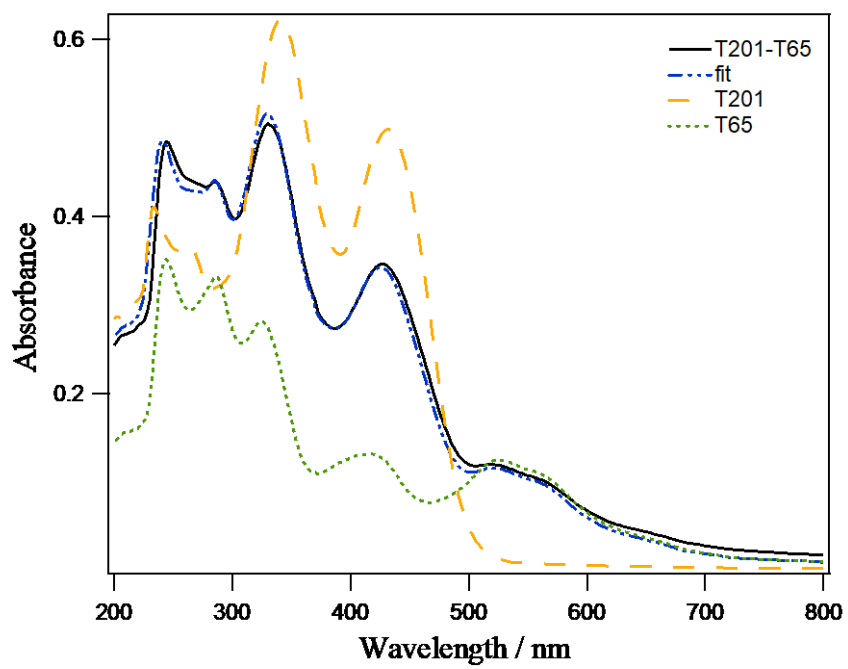


**Figure 17.** The absorbance spectra of a) T201, T169, and T201-T169 b) T201, T65, and T201-T65 c) T201, T135, and T201-T135 d) T201, N719, and T201-N719 on TiO<sub>2</sub> films

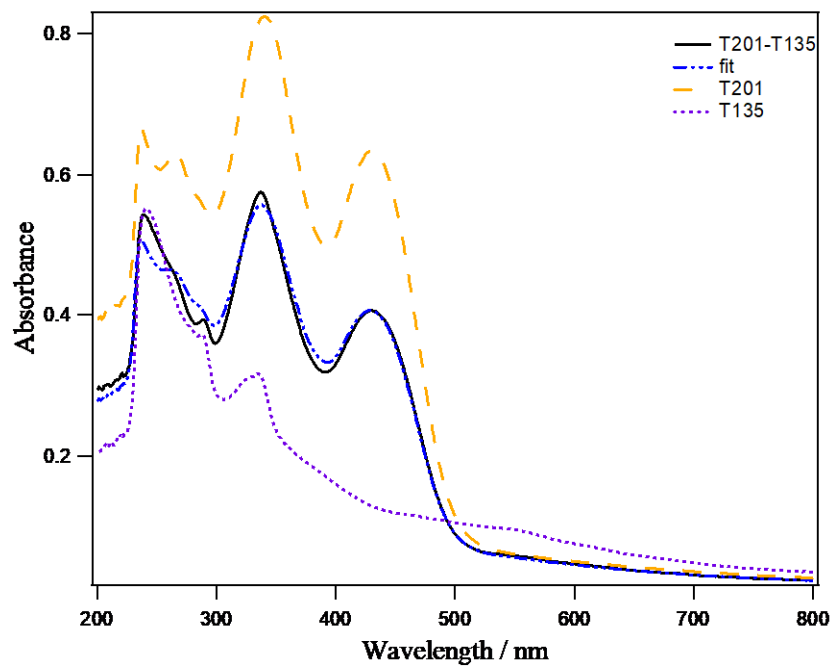
Next, the desorption of the dye molecules was performed by immersing the dye-adsorbed TiO<sub>2</sub> electrodes in an alkaline solution of THF:EtOH:H<sub>2</sub>O for a couple of minutes. The absorbance spectra of the desorbed solutions were plotted as a function of wavelength whereby dye loading amounts were obtained from the maximum absorbance of the curves. Table 8 and Figure 18 show the dye loading amounts and absorbance spectra of desorbed TiO<sub>2</sub> films for T201, T169, T65, T139, N719, and co-sensitized dyes.



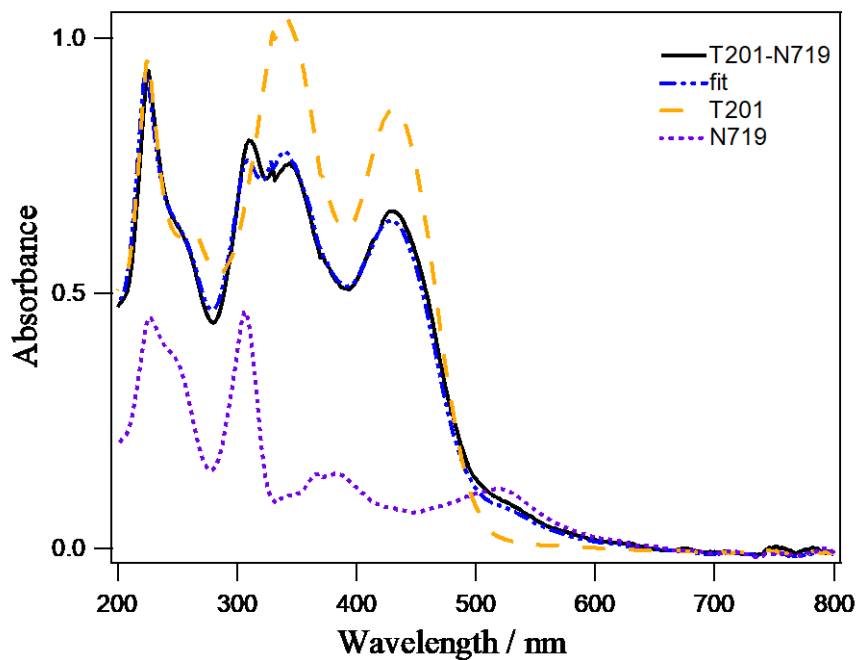
a)



b)



c)



d)

**Figure 18.** The absorbance spectra of TiO<sub>2</sub> desorbed films of a) T201, T169, and T201-T169 b) T201, T65, and T201-T65 c) T201, T135, and T201-T135 d) T201, N719, and T201-N719 as a function of wavelength

**Table 8.** The dye loading of a) T201 and T169 b) T201 and T65 c) T201 and T135 d) T201 and N719 for pure and co-adsorbed TiO<sub>2</sub> films<sup>a</sup>

a)

Dye Concentration in Solution	nT201 (mol)	nT169 (mol)	Total dye loading (mol)
T201 (0.2 mM)	$9.9 \times 10^{-8}$	0	$9.9 \times 10^{-8}$
T169 (0.1 mM)	0	$9.3 \times 10^{-8}$	$9.3 \times 10^{-8}$
T201(0.2 mM) + T169 (0.1 mM)	$5.9 \times 10^{-8}$	$4.9 \times 10^{-8}$	$10.8 \times 10^{-8}$

b)

Dye Concentration in Solution	nT201 (mol)	nT65 (mol)	Total dye loading (mol)
T201 (0.2 mM)	$9.6 \times 10^{-8}$	0	$9.6 \times 10^{-8}$
T65 (0.2mM)	0	$8.3 \times 10^{-8}$	$8.3 \times 10^{-8}$
T201(0.2 mM) + T65 (0.2mM)	$4.5 \times 10^{-8}$	$7.2 \times 10^{-8}$	$11.7 \times 10^{-8}$

c)

Dye Concentration in Solution	nT201 (mol)	nT135 (mol)	Total dye loading (mol)
T201 (0.2 mM)	$1.2 \times 10^{-7}$	0	$1.2 \times 10^{-7}$
T135 (0.1 mM)	0	$1.2 \times 10^{-7}$	$1.2 \times 10^{-7}$
T201(0.2 mM) + T135 (0.1 mM)	$7.2 \times 10^{-8}$	$2.4 \times 10^{-8}$	$9.6 \times 10^{-8}$

d)

Dye Concentration in Solution	nT201 (mol)	nN719 (mol)	Total dye loading (mol)
T201 (0.2 mM)	$1.6 \times 10^{-7}$	0	$1.6 \times 10^{-7}$
N719 (0.3 mM)	0	$8.3 \times 10^{-8}$	$8.3 \times 10^{-8}$
T201(0.2 mM) + N719 (0.3 mM)	$1.1 \times 10^{-7}$	$5.0 \times 10^{-8}$	$1.6 \times 10^{-7}$

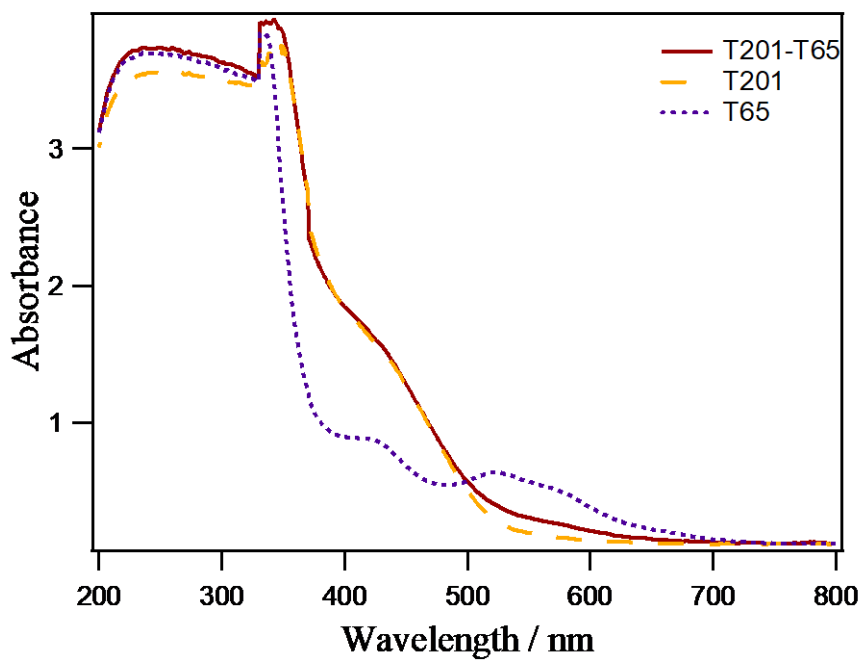
<sup>a</sup> A 4  $\mu\text{m}$  TiO<sub>2</sub> film of 2.56 cm<sup>2</sup> area was used. Each measurement was done in duplicate.

The experimental values of T201 co-sensitized with each of T169, T65, T135, and N719 were fitted along with the spectra of their respective desorbed solutions. The coefficients of adsorption were calculated from the graph and turned out to be 0.60 and 0.53 for T201 and T169, 0.47 and 0.88 for T201 and T65, 0.60 and 0.20 for T201 and T135, and finally, 0.69 and 0.60 for T201 and N719, respectively.

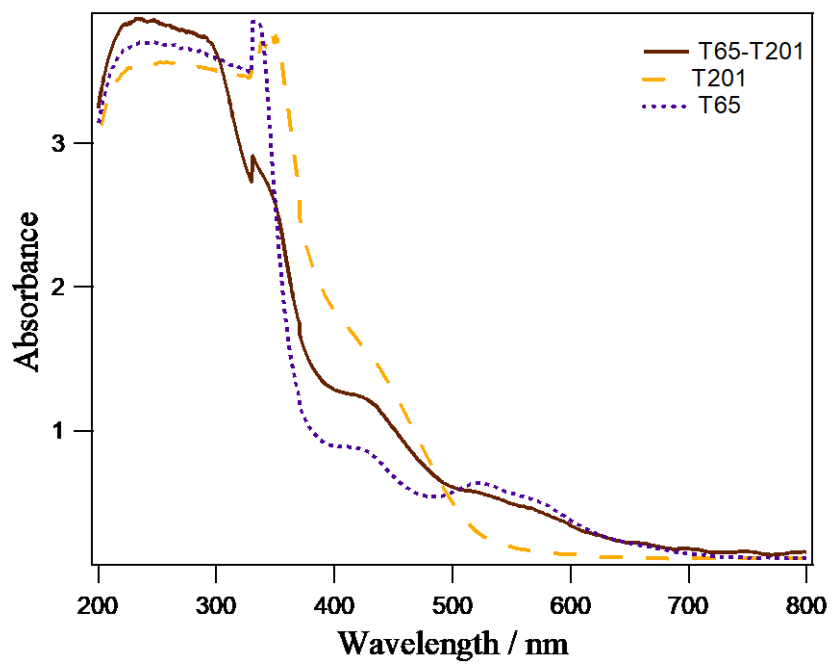
#### 3.4.2.2 Sequential Deposition vs One-Step Co-adsorption Method

In 2015, Ooyama *et al.* tested the co-adsorption of dyes via a stepwise adsorption method (firstly immersed in the first dye solution and then the next one) or a one-step co-adsorption method using a mixed dye solution.<sup>96</sup> Subsequently, they found that there was little difference in the photovoltaic performance between the co-sensitized cells prepared either by the former or the latter technique.

Curious to see if the same applies to our dyes, we have conducted a sequential deposition of T65 followed by T201 and vice versa. This was performed by first immersing a 4  $\mu\text{m}$  thick  $\text{TiO}_2$  electrode into a 0.2 mM T65 solution for 15 h and then 0.2 mM solution of T201 for 15 h and vice versa. The UV-Vis spectra of the  $\text{TiO}_2$ -adsorbed dyes are given in Figure 19. From the graphs, it is obvious that the successive deposition of T65 followed by T201 gave an absorption spectrum comparable to forming a dye cocktail of both dyes, however deposition of T201 followed by T65 showed that the latter did not adsorb on the  $\text{TiO}_2$  film. This can be clearly explained by the corresponding sizes of both sensitizers; whereby by the bulky donor group of T201 when adsorbed first prevented the smaller T65 dye from binding to the film.



a)



b)

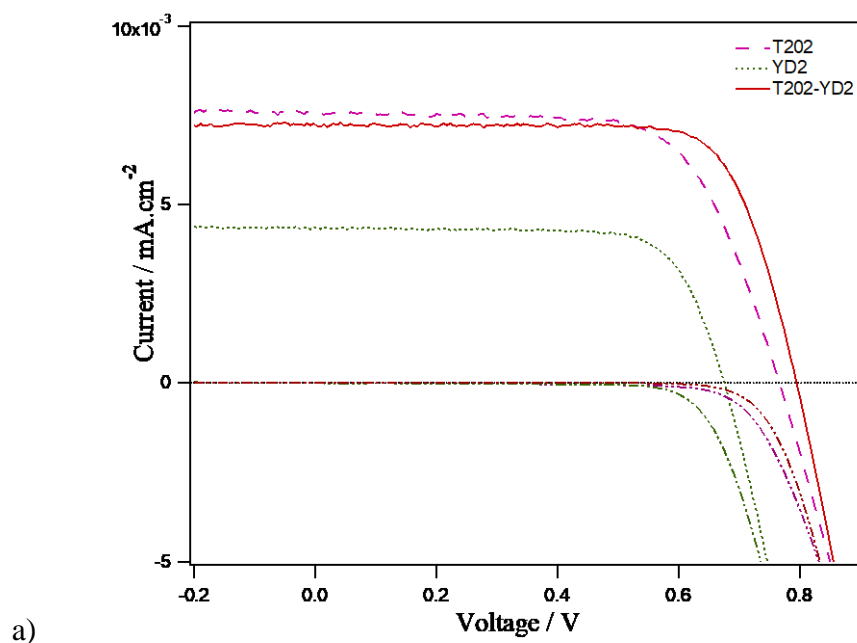
**Figure 19.** The absorbance spectra of a) T201 deposition followed by T65 b) T65 deposition followed by T201 on TiO<sub>2</sub> films

### 3.4.3 Photovoltaic Performance and IPCE spectra

#### 3.4.3.1 Co-adsorption of T202 with DB and YD2

After measuring the dye loading amounts, and proving that molecular size does in fact play a role in the adsorption method of the sensitizers to the titania surface, liquid dye-sensitized solar cells were fabricated in order to test the photovoltaic performance of the co-sensitized T202-DB and T202-YD2 with a cobalt tris(bipyridine) electrolyte system (containing 0.2 M TBP).

The first study consisted of assembling DSSCs of individual dyes T202 and YD2 having each a concentration of 0.2 mM, and co-adsorbed dyes T202-YD2 having the same concentrations (with a TiO<sub>2</sub> thickness of 4 μm). The output photovoltaic characteristics are summarized in Table 9, and Figures 20 (a, b).





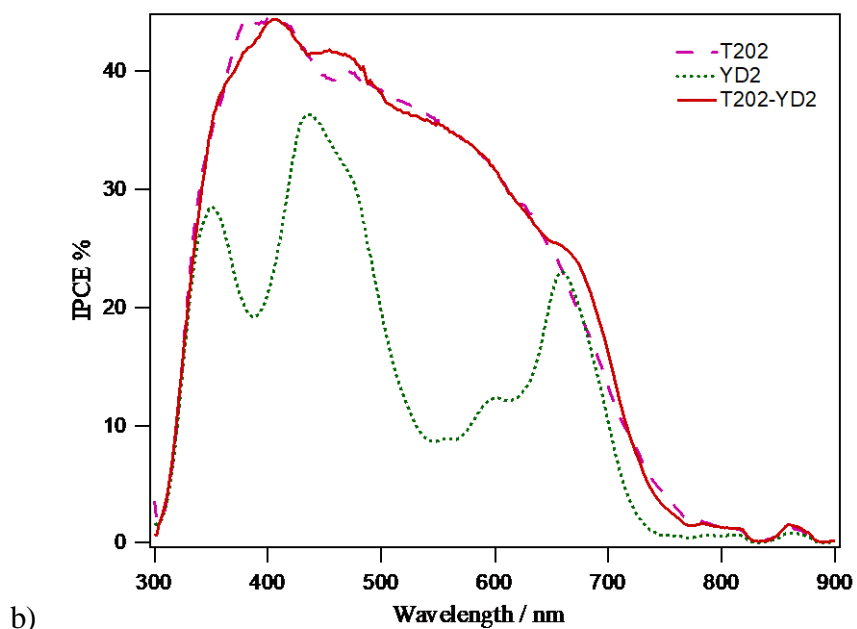


**Figure 20.** (a) Photocurrent-voltage characteristics under  $1000 \text{ W m}^{-2}$  AM1.5 G illumination of DSSCs sensitized with T202 and YD2 and co-sensitized with T202-YD2 (lines) and in darkness (dotted lines); (b) Corresponding IPCE % spectra ( $4 \mu\text{m}$   $\text{TiO}_2$  thickness)

**Table 9.** Photovoltaic performance of the T202 and YD2 DSSCs and co-sensitized T202-YD2

Dye	$J_{\text{SC}}$ ( $\text{mA}\cdot\text{cm}^{-2}$ )	$V_{\text{OC}}$ (mV)	FF	PCE % <sup>a</sup>
T202	7.60	768	0.67	3.9
YD2	4.30	674	0.74	2.1
T202-YD2	7.20	795	0.70	4.0

<sup>a</sup>Measured under  $100 \text{ mW cm}^{-2}$  simulated AM1.5 spectrum with an active area of  $0.5 \times 0.5 \text{ cm}^2$  and a black mask ( $0.6 \times 0.6 \text{ cm}^2$ ); the electrolyte consisted of 0.25 M Co(II), 0.06 M Co(III), 0.1 M  $\text{LiClO}_4$ , and 0.2 M TBP

As summarized in Table 9, the power conversion efficiency of the YD2-based DSC was significantly improved from 2.1 % to 4.0 % (compared to YD2) upon co-

sensitization with the pyridine-anchor dye T202. Notable differences in the short-circuit current  $J_{SC}$  were detected for T202- and YD2-based dyes, whereby T202 exhibited a value of  $7.60 \text{ mA}\cdot\text{cm}^{-2}$ , while that of YD2 was  $4.30 \text{ mA}\cdot\text{cm}^{-2}$ . These results clearly highlight the efficiency of T202 as a pyridyl-based sensitizer. Moreover, it is worth mentioning here that, with respect to YD2 and T202, remarkable increases in  $V_{OC}$  and PCE were observed upon co-adsorption with T202. Regarding the photovoltage, a 121 mV increase was obtained for upon co-adsorption with respect to YD2 and 27 mV with respect to T202. This clearly proves that the zinc-porphyrin dye YD2 was more or less able to occupy some empty spaces of the T202 dye which not only prevented dye aggregation, but also limited charge recombination by inhibiting the  $\text{Co}^{3+}$  ions present in the electrolyte from penetrating into the  $\text{TiO}_2$  surface.

The same cobalt electrolyte (containing 0.2 M TBP) was used as a redox mediator for the assembly of DSSCs using T202 and DB as sensitizers.<sup>106</sup> The single dyes have a concentration of 0.2 mM, and 0.03 mM for T202 and DB respectively, and a dye cocktail of both dyes having the same concentrations (with a  $\text{TiO}_2$  thickness of 6-7  $\mu\text{m}$ ). Their photovoltaic performances are presented in Table 10 and Figure 21 (a,b).

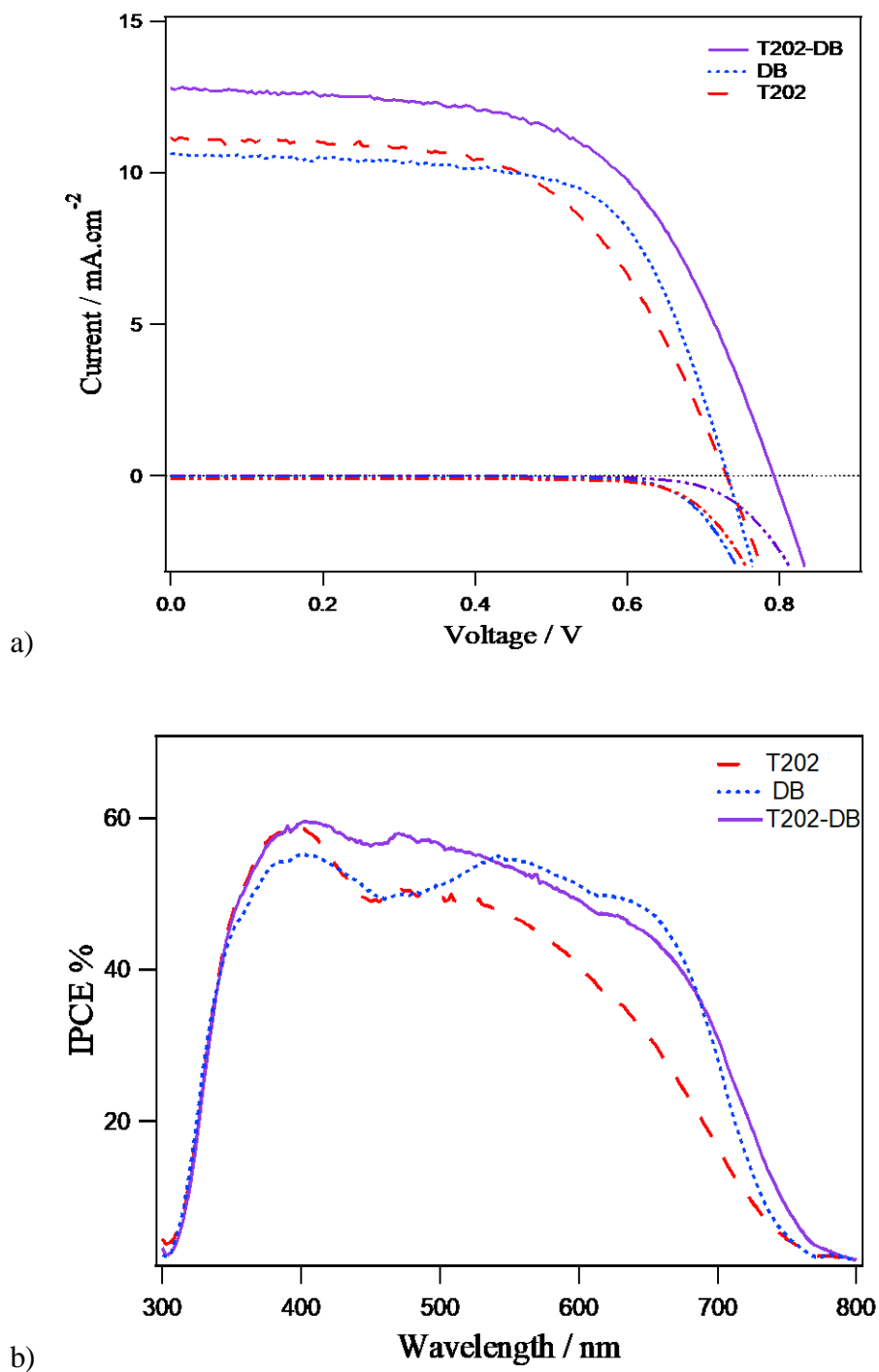


**Figure 21.** (a) Photocurrent-voltage characteristics under  $1000 \text{ W m}^{-2}$  AM1.5 G illumination of DSSCs sensitized with T202 and DB and co-sensitized with T202-DB (lines) and in darkness (dotted lines); (b) Corresponding IPCE % spectra (6-7  $\mu\text{m}$  TiO<sub>2</sub> thickness)

**Table 10.** Photovoltaic performance of the T202 and DB DSSCs and co-sensitized T202-DB

Dye	$J_{SC}$ (mA·cm <sup>-2</sup> )	$V_{OC}$ (mV)	FF	PCE % <sup>a</sup>
T202	11.1	739	0.57	4.7
DB	10.6	737	0.66	5.1
T202-DB	12.8	792	0.59	6.0

<sup>a</sup>Measured under 100 mW cm<sup>-2</sup> simulated AM1.5 spectrum with an active area of 0.5 × 0.5 cm<sup>2</sup> and a black mask (0.6 × 0.6 cm<sup>2</sup>); the electrolyte consisted of 0.25 M Co(II), 0.06 M Co(III), 0.1 M LiClO<sub>4</sub>, and 0.2 M TBP

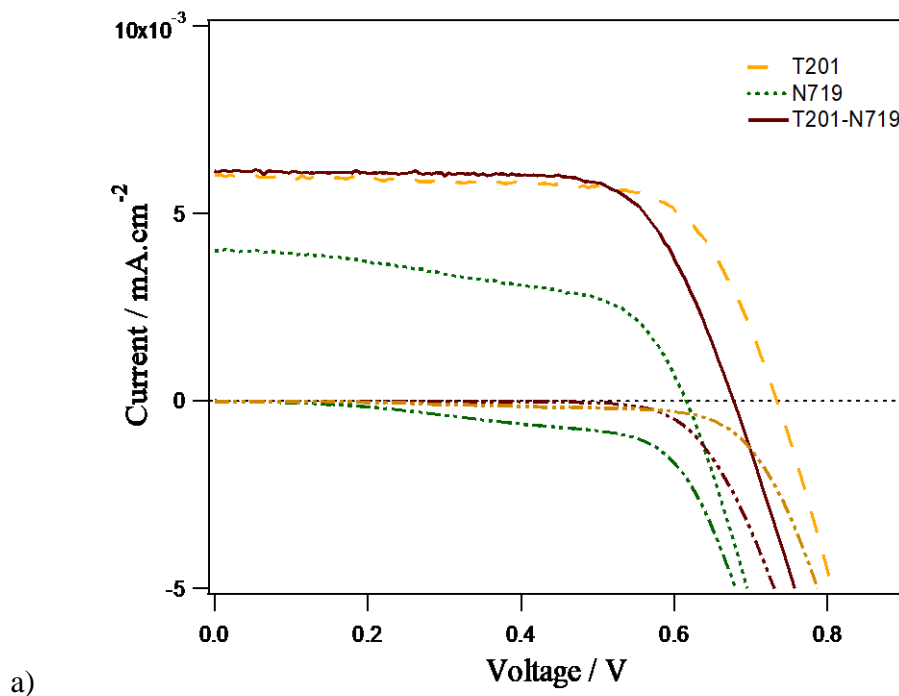
The competence of T202 as a sensitizer is further emphasized in Table 10. The DB-based DSC had a power conversion efficiency of 5.1 % which is higher than that of T202 (4.7 %). Furthermore, comparable  $J_{SC}$  and  $V_{OC}$  were obtained for both T202 ( $J_{SC}$  = 11.1 mA·cm<sup>-2</sup>;  $V_{OC}$  = 739 mV) and DB ( $J_{SC}$  = 10.6 mA·cm<sup>-2</sup> and  $V_{OC}$  = 737 mV). Upon co-sensitization, it is evident that the PCE has increased with respect to both dyes, by around 15% for DB and 22% for T202. The increase in  $J_{SC}$  from 11.1 mA·cm<sup>-2</sup> to 12.8 mA·cm<sup>-2</sup> was probably due to the complementary absorption properties of T202 with DB as can be inferred from the IPCE % spectrum. As for the photovoltage, an increment of 55 mV was obtained with respect to DB upon co-adsorption, which, as mentioned previously, was undoubtedly due to a decrease in the electron recombination processes as suggested by the dark currents seen in Figure 21.

#### 3.4.3.2 Co-adsorption of T201 with N719

The paradigm N719 dye is one of the most efficient dyes when used with an iodide/iodine based electrolyte system, however, it poorly performs when used with cobalt

based redox systems. As explained in section 3.4.2, the molecular structure of N719 increases the rate of recombination with cobalt species in a DSSC most probably due to the formation of ion pairs between the carboxylate ions and the  $\text{Co}^{+3}$  complexes. This allows the dye to have a very limited efficiency in conjunction with a cobalt-based electrolyte system. For this purpose, we aim to study dye-sensitized solar cells of T201, N719, and T201-N719, and their photovoltaic performance in a cobalt tris-bipyridine electrolyte system (containing 0.2 M TBP), in order to see if the above recombination kinetics can be diminished.

To do so, DSSCs were sensitized with individual dye T201 and N719 having concentrations of 0.2 mM and 0.3 mM respectively, and the co-sensitized DSSC bearing an equal concentration of both dyes (with a  $\text{TiO}_2$  thickness of 6-7  $\mu\text{m}$ ). The output characteristics are summarized in Table 11 and Figure 22 (a,b).



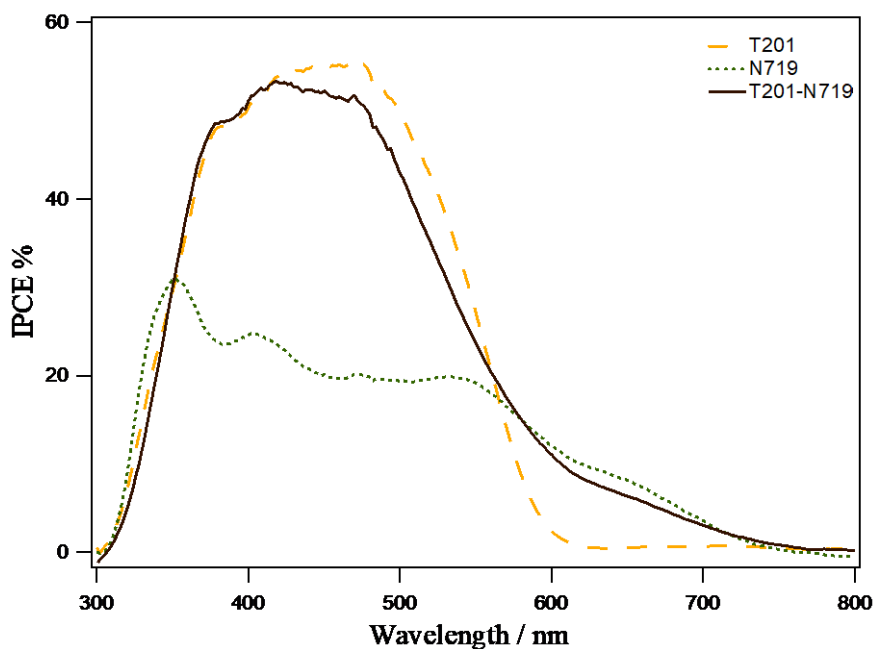


**Figure 22.** (a) Photocurrent-voltage characteristics under  $1000 \text{ W m}^{-2}$  AM1.5 G illumination of DSSCs sensitized with T201 and N719 and co-sensitized with T201-N719 (lines) and in darkness (dotted lines); (b) Corresponding IPCE % spectra (6-7  $\mu\text{m}$   $\text{TiO}_2$  thickness)

**Table 11.** Photovoltaic performance of the T201 and N719 DSSCs and co-sensitized T201-N719

Dye	$J_{SC}$ ( $\text{mA}\cdot\text{cm}^{-2}$ )	$V_{OC}$ (mV)	FF	PCE % <sup>a</sup>
T201	6.01	735	0.70	3.1
N719	4.01	614	0.52	1.3
T201-N719	6.18	674	0.70	2.9

<sup>a</sup>Measured under  $100 \text{ mW cm}^{-2}$  simulated AM1.5 spectrum with an active area of  $0.5 \times 0.5 \text{ cm}^2$  and a black mask ( $0.6 \times 0.6 \text{ cm}^2$ ); the electrolyte consisted of 0.25 M Co(II), 0.06 M Co(III), 0.1 M  $\text{LiClO}_4$ , and 0.2 M TBP

It can be seen from the above results that the T201-sensitized solar cell provided a 3.1 % PCE, around double that of N719 (1.3 %). The short-circuit current and open-circuit voltage of T201 are adequately higher than those of N719, providing a  $J_{SC} = 6.01 \text{ mA.cm}^{-2}$  and  $V_{OC} = 735 \text{ mV}$  for the former, and  $J_{SC} = 4.01 \text{ mA.cm}^{-2}$  and  $V_{OC} = 614 \text{ mV}$  for the latter. Evidentially, the performance of the Ru (II) sensitizer was enhanced upon co-sensitization with the organic, pyridine-anchor dye. As expected, the overall conversion efficiency of the cell increased by two-fold – from 1.3 % to 2.9 % with respect to N719– which further proves that presence of T201 helped in suppressing the recombination kinetics. This was further justified by a 60 mV increase in the photovoltage with respect to N719. As mentioned before, the formation of ion pairs between the carboxylate groups of N719 and the oxidized  $\text{Co}^{3+}$  species were probably inhibited by the presence of the long alkyl chains found in the T201 triphenylamine donor group, which accounted for the considerable increase in photovoltage.

#### ***3.4.4 Electrochemical Impedance Spectroscopy***

To further elucidate the above-mentioned photovoltaic results and obtain dynamic information of the interfacial charge transfer processes and recombination kinetics in DSSCs sensitized with T202, DB, YD2, T202-DB, T202-YD2, T201, N719, and T201-N719, electrochemical impedance spectroscopy (EIS) measurements were performed at  $V_{OC}$  under different light intensities.

### 3.4.4.1 Measurements for Co-adsorption of T202 with YD2 versus DB

Figures 23, 24, and 25 show respectively the charge transfer resistance  $R_{CT}$  -which represents the resistance for the recombination of the  $TiO_2$  electrons with the oxidized redox species in the electrolyte and/or to the oxidized dye in case of low regeneration kinetics-, the chemical capacitance  $C_{\mu}$  -which denotes the filling of the traps inside the mesoporous semiconductor -, and the electron lifetime. These three factors were plotted vs the applied voltage ( $nE_F - E_{F,redox}$ ), where  $nE_F$  denotes the electron quasi-Fermi energy level in the  $TiO_2$  and  $E_{F,redox}$  is the electrolyte redox Fermi level.

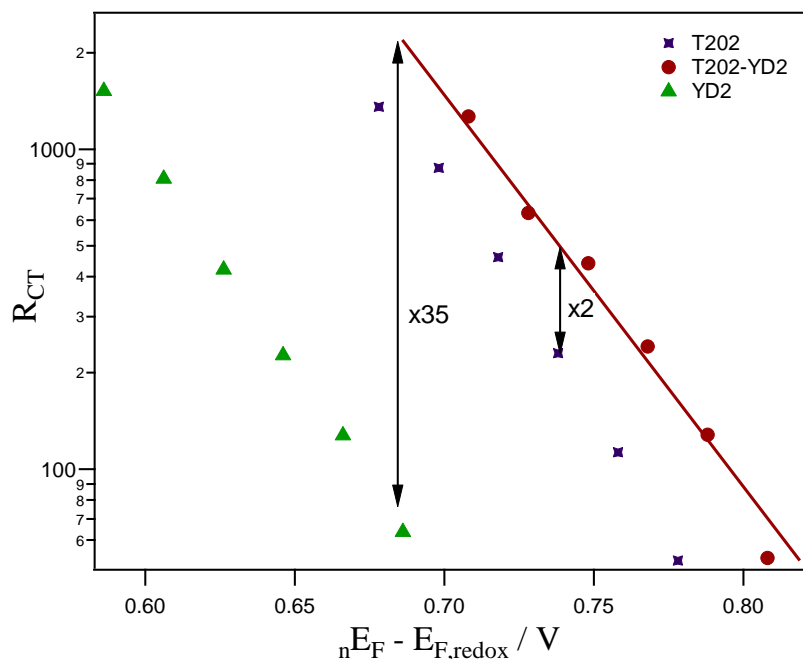


**Figure 23.** Charge transfer resistance values extracted from EIS measurements of T202, YD2, and co-sensitized T202-YD2 DSSCs



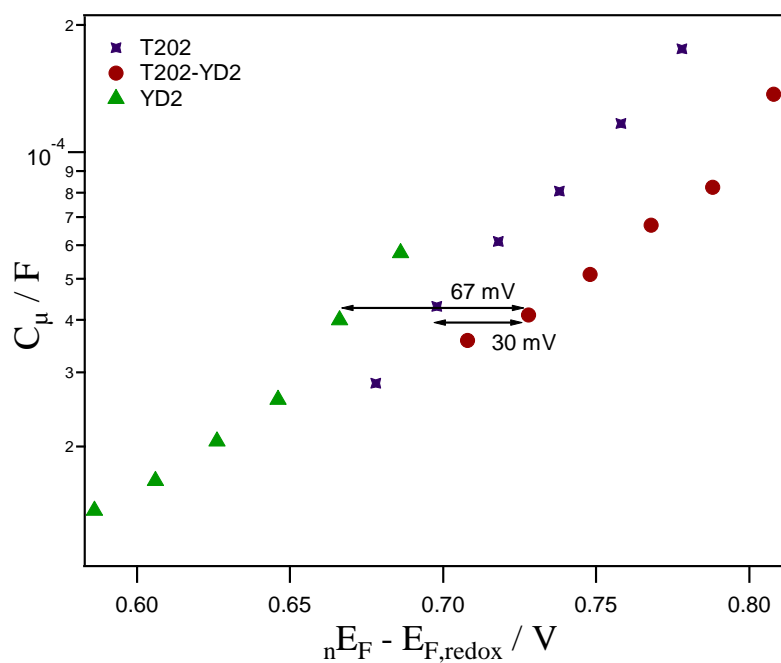


**Figure 24.** Chemical capacitance values extracted from EIS measurements of T202, YD2, and co-sensitized T202-YD2 DSSCs

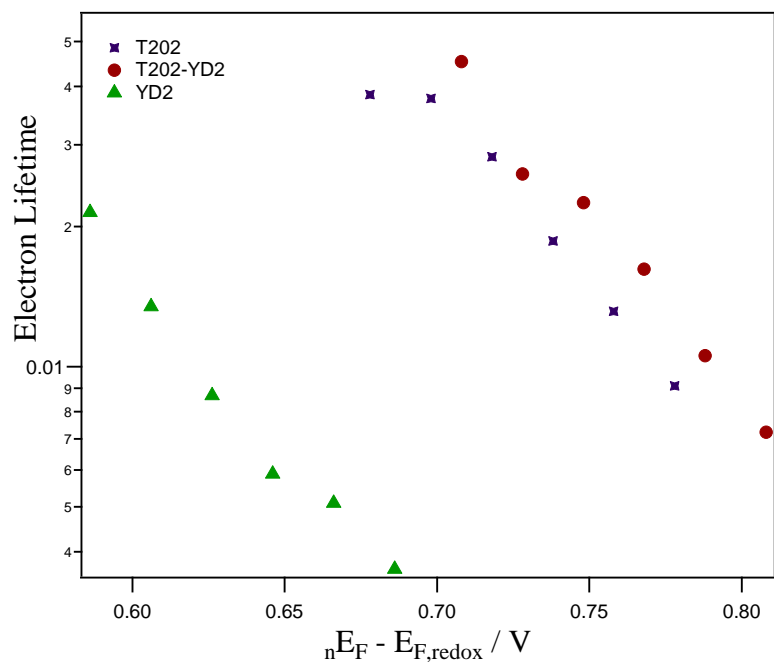


**Figure 25.** Electron lifetime values extracted from EIS measurements of T202, YD2, and co-sensitized T202-YD2 DSSCs

According to Figure 23, the  $R_{CT}$  values of the co-sensitized T202-YD2 cells were around 35 times and 2 times higher than those of the YD2 and T202 cells respectively. A larger  $R_{CT}$  value can be explained by a decrease in the electron recombination processes between the  $TiO_2$  electrons and the oxidized redox species and/or oxidized dye. This blocking of the recombination pathway is probably due to an increase in total dye coverage as depicted by Boschloo *et al.*<sup>109</sup> However, the very slight increase in the recombination resistance of the T202-YD2 device with respect to the T202 device had little effect on the  $J_{SC}$  and  $V_{OC}$  values, which in turn explains the mediocre increase in conversion efficiency. Furthermore, it is observed in Figure 24 that the T202-YD2 co-sensitized device clearly shows a shift  $\Delta ({}_nE_F - E_{F,redox})$  of  $\sim 67$  mV higher than that of the YD2 device alone. These chemical capacitance results are compatible with the increase in  $V_{OC}$  of the co-adsorbed cell in reference to YD2 as observed in Table 9. Because the same cobalt electrolyte was used for the three cells, we know for certain that the electrolyte redox Fermi level  $E_{F,redox}$  will not be altered. Therefore, we speculate that the electron quasi-Fermi energy level  ${}_nE_F$  has shifted upwards. However, it is crucial to mention that the presence of the carboxylic acid anchor in YD2 results in a 20 mV decrease in the semiconductor's conduction band, consequently, we should observe a decrease in  $V_{OC}$  upon co-sensitizing T202 and YD2. The upward shift in  ${}_nE_F$  and higher charge transfer resistance finely explain the  $V_{OC}$  increase, where the higher total dye coverage on the titania surface results in low recombination kinetics and therefore explains the profound increase in photovoltage and the overall efficiency of the co-sensitized T202-YD2 with respect to the single cells. The high electron lifetimes  $\tau = R_{CT} \cdot C\mu$  as a function of  $({}_nE_F - E_{F,redox})$  plotted in Figure 25 are consistent with the slower recombination kinetics seen by the  $R_{CT}$  values of the co-adsorbed T202-YD2.

Using the same cobalt-based electrolyte system, EIS measurements of solar cells sensitized with T202, DB, and T202-DB were performed. The plots of  $R_{CT}$ ,  $C_{\mu}$ , and electron lifetimes are shown in Figures 26, 27, and 28 respectively.

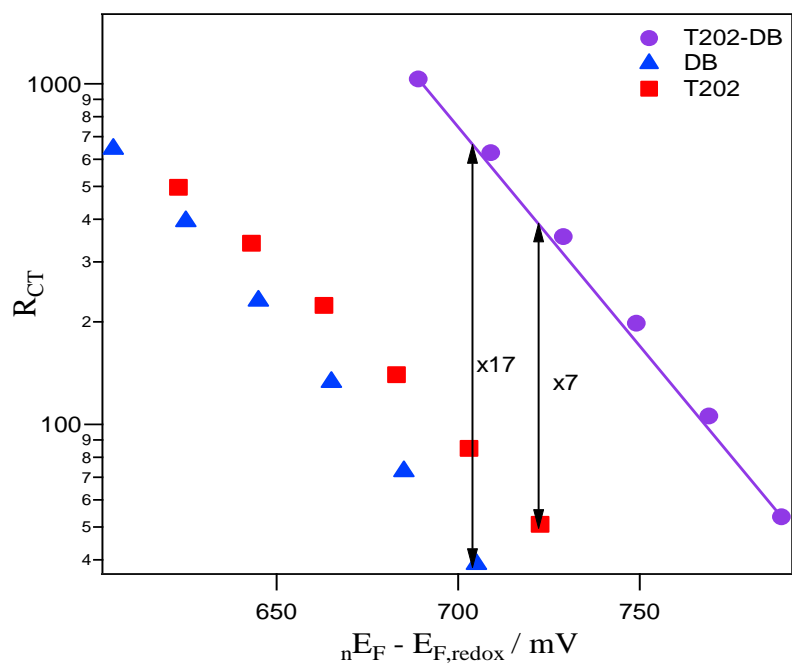


**Figure 26.** Charge transfer resistance values extracted from EIS measurements of T202, DB, and co-sensitized T202-DB DSSCs

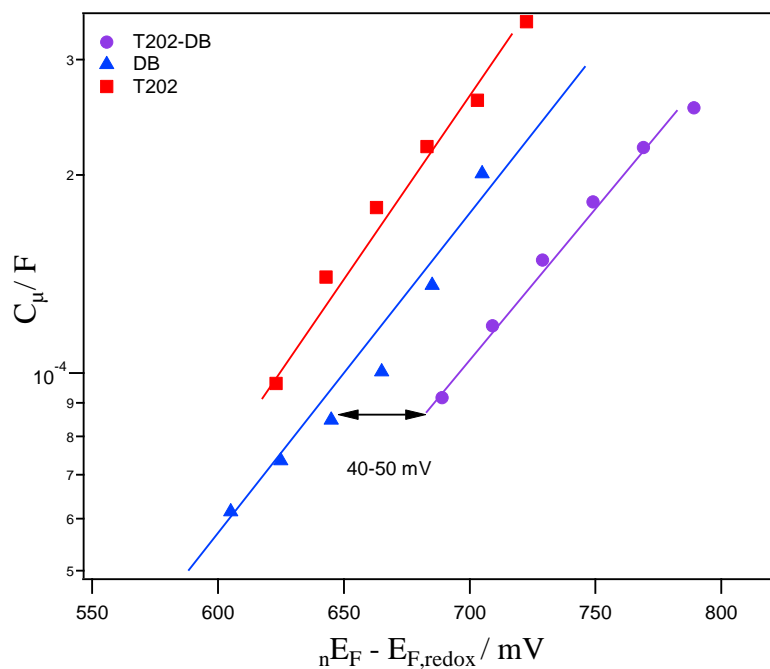


**Figure 27.** Chemical capacitance values extracted from EIS measurements of T202, DB, and co-sensitized T202-DB DSSCs

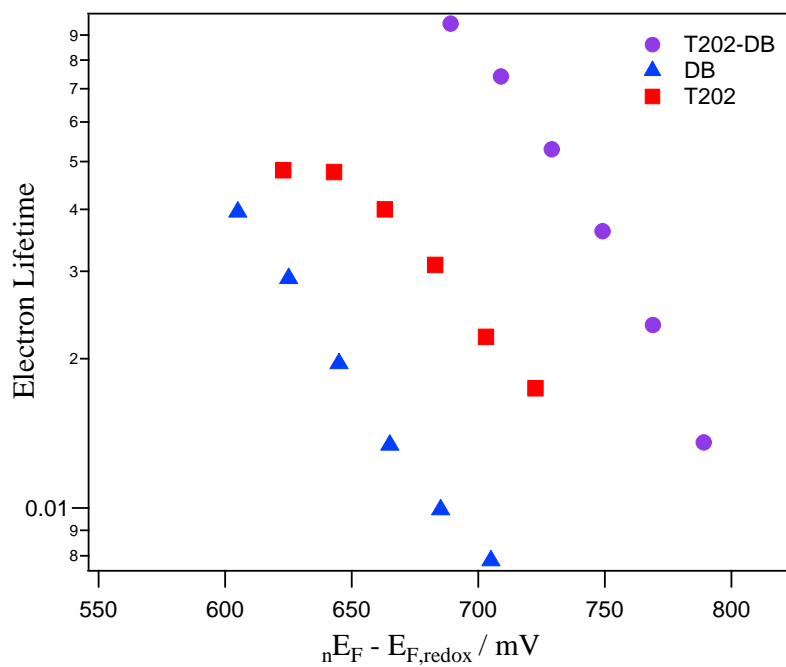


**Figure 28.** Electron lifetime values extracted from EIS measurements of T202, DB, and co-sensitized T202-DB DSSCs

It is evident from the charge transfer values of Figure 26 that the T202-DB device showed an  $R_{CT}$  value of around 17 times higher than the DB device. As previously explained, these results are probably due to the obstruction of the electrolyte pathway to the  $TiO_2$  surface. Looking at the chemical capacitance results in Figure 27, we notice that a 40-50 mV shift in  $\Delta ({}_nE_F - E_{F,redox})$  was observed for the T202-DB sensitized solar cell in relevance to DB. This upward shift in the semiconductor's conduction band edge is interrelated with the results obtained in Table 10, which show an increase in  $V_{OC}$  of the co-sensitized cell with respect to DB. Again the increase in  $V_{OC}$  is due to both the slower recombination kinetics and increase in the  ${}_nE_F - E_{F,redox}$  energy gap. In addition, the high electron lifetimes plotted in Figure 28 further elucidate the high charge transfer resistances, and thus slower recombination processes explained above.

#### 3.4.4.2 Measurements for Co-adsorption of T201 with N719

In a third study, and in order to explain the co-sensitization results of T201 and N719, EIS measurements were performed on individual and co-sensitized DSSC assembled using a cobalt electrolyte system. The plots of the charge transfer resistance  $R_{CT}$ , the chemical capacitance  $C_{\mu}$ , and electron lifetimes are presented in Figures 29, 30, and 31 respectively.

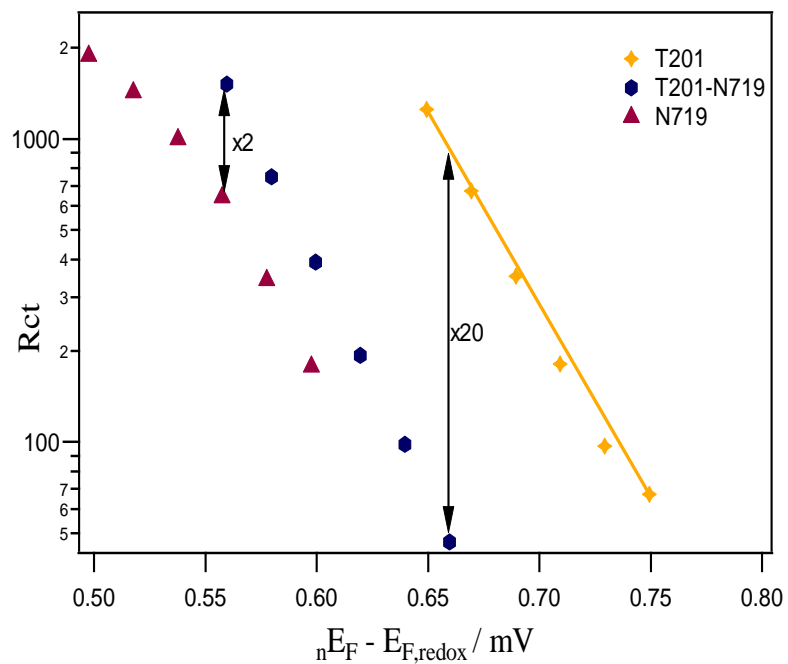


**Figure 29.** Charge transfer resistance values extracted from EIS measurements of T201, N719, and co-sensitized T201-N719 DSSCs

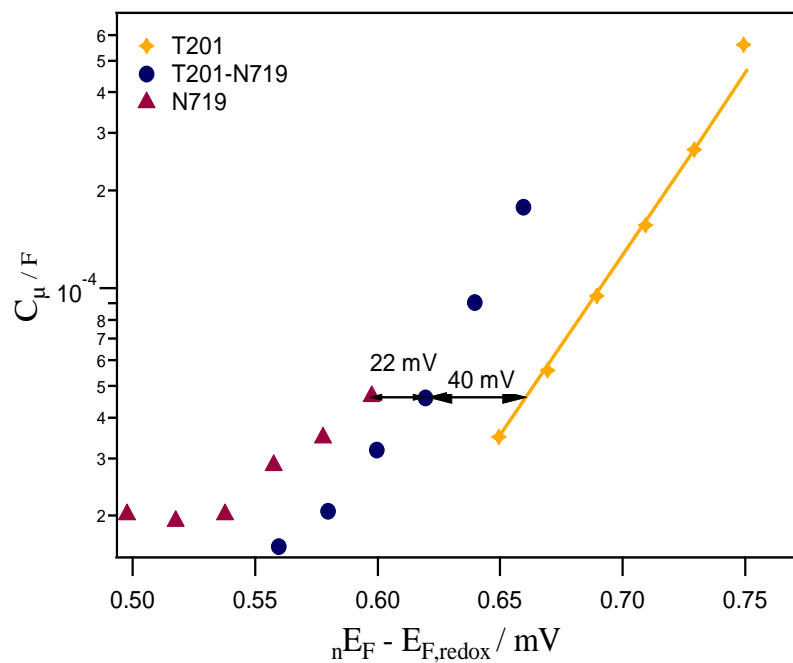


**Figure 30.** Chemical capacitance values extracted from EIS measurements of T201, N719, and co-sensitized T201-N719 DSSCs

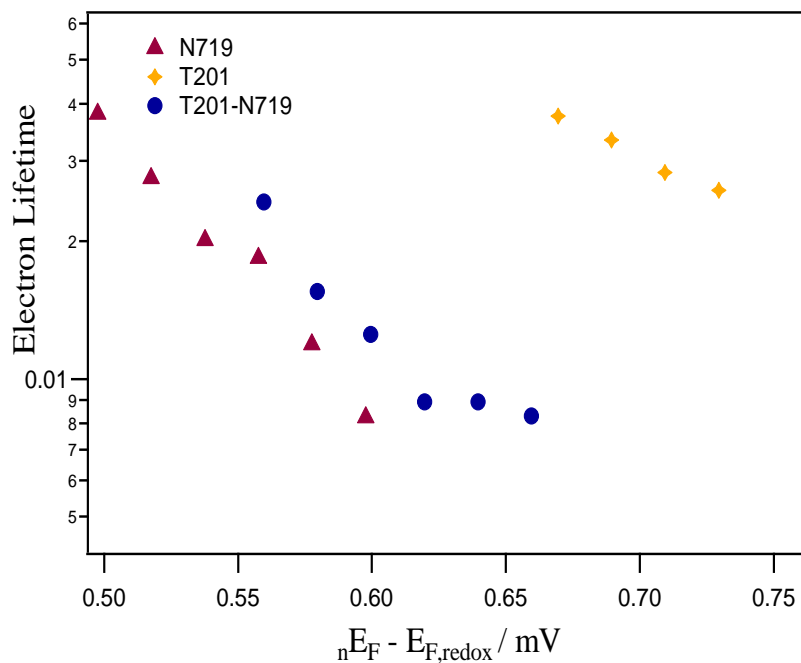


**Figure 31.** Electron lifetime values extracted from EIS measurements of T201, N719, and co-sensitized T201-N719 DSSCs

According to Figure 29, the charge transfer resistance values of the co-sensitized T201-N719 device were around two times higher than that of the N719 device alone. As discussed earlier, this is most likely due to an increase in the dye loading amount, which in turn decreases any recombination kinetics between the oxidized electrolyte and the  $\text{TiO}_2$  electrons. The chemical capacitance results in Figure 30 show a 22 mV shift towards higher values in  $\Delta (nE_F - E_{F,redox})$  for the T201-N719 device in comparison to the N719 device. These results are consistent with the increase in open-circuit voltage obtained in Table 11.

## CHAPTER IV

### CONCLUSION

In conclusion, we were successful in synthesizing three novel dyes T200, T201, and T202 bearing a pyridine ring as an anchoring and electron-withdrawing group. Given the fact that a pyridine anchor binds to the Lewis acid sites of the semiconductor, we carried on the co-adsorption of T202 with carboxylic acid-based dyes YD2 and DB. The dye loading measurements showed a slight decrease in the dye loading amounts of T202 and YD2 on the co-sensitized film, leading us to the conclusion that the zinc porphyrin moiety was passably able to fill the intermolecular space present in T202. On the other hand, striking results were obtained for T202 and DB, whereby the amount of DB adsorbed decreased by 65 % with respect to the single-sensitized DB film. This was attributed to the complementary-size relationship of the sensitizers such that T202 did not possess a suitable size and shape to fill the grooves present in DB. Furthermore, in order to improve the performance of Ruthenium (II) dyes in a cobalt redox shuttle, the co-adsorption of T201 with each of T169, T135, T65, and N719 was performed; whereby the highest dye loading amounts were obtained for T201 and N719. In addition, the photovoltaic performances of the co-adsorbed T202-YD2, T202-DB, as well as T201-N719 liquid DSSCs were enhanced with respect to the single-sensitized films, especially in terms of photovoltage. EIS measurements demonstrated that the  $V_{OC}$  increase was correlated with an increase in total



dye coverage, which blocked any recombination between the TiO<sub>2</sub> electrons and the oxidized species, as well as an upward shift in the flatband potential of the semiconductor.

In summary, the co-sensitization of complementary sensitizers is one of the most promising strategies to enhance dye coverage on the semiconductor, increase light harvesting efficiencies, and improve the photovoltaic performance of dye-sensitized solar cells. Future work should most likely highlight the three most important factors in the selection of co-sensitizers: 1) their molecular geometries, 2) the presence of different anchoring groups to prevent competitive adsorption, and 3) their complementary absorption properties. These aspects favor the reduction of recombination between the electrons in the semiconductor and the oxidized redox mediator, which also allows the advantageous use of thin films.

## SUPPORTING INFORMATION

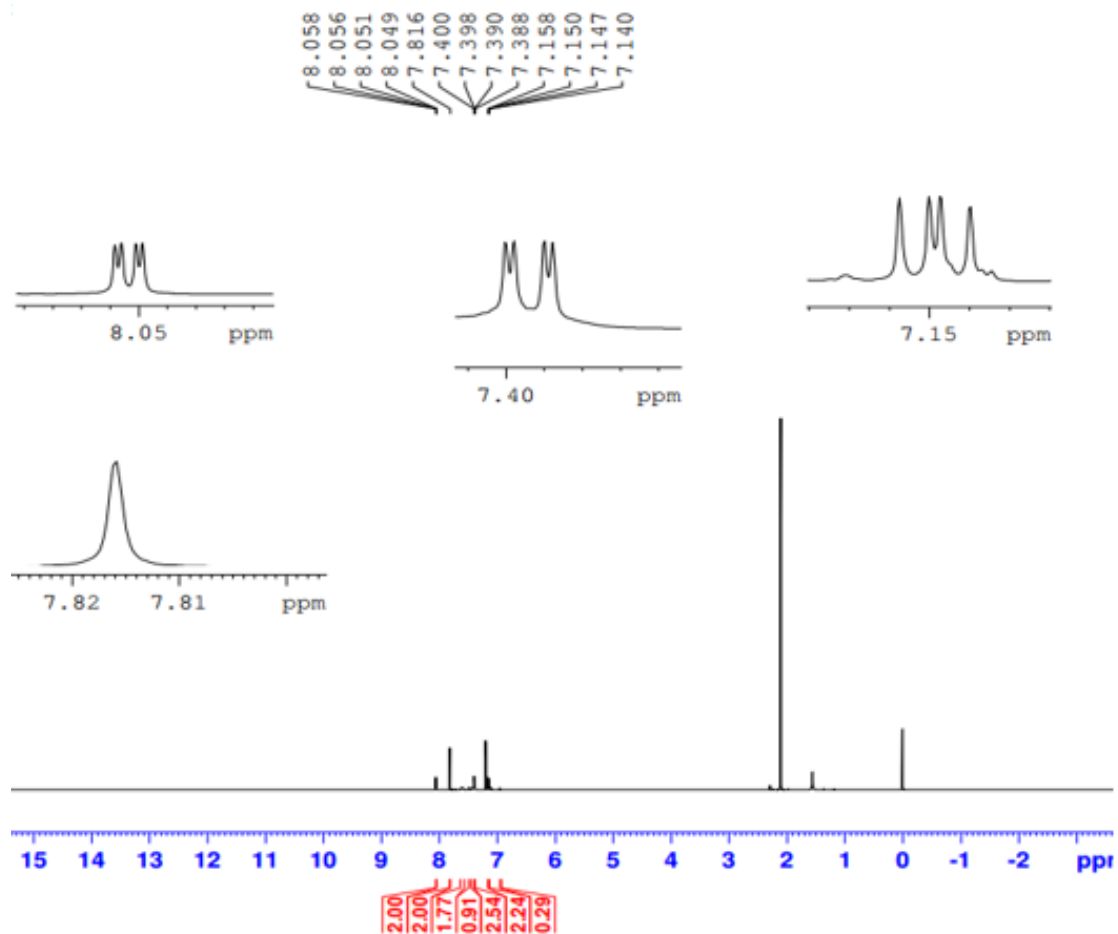


**Figure 32S.**  $^1\text{H}$ NMR of 4,7-dithien-2-yl-2,1,3-benzothiadiazole in  $\text{CDCl}_3$  at 500 MHz

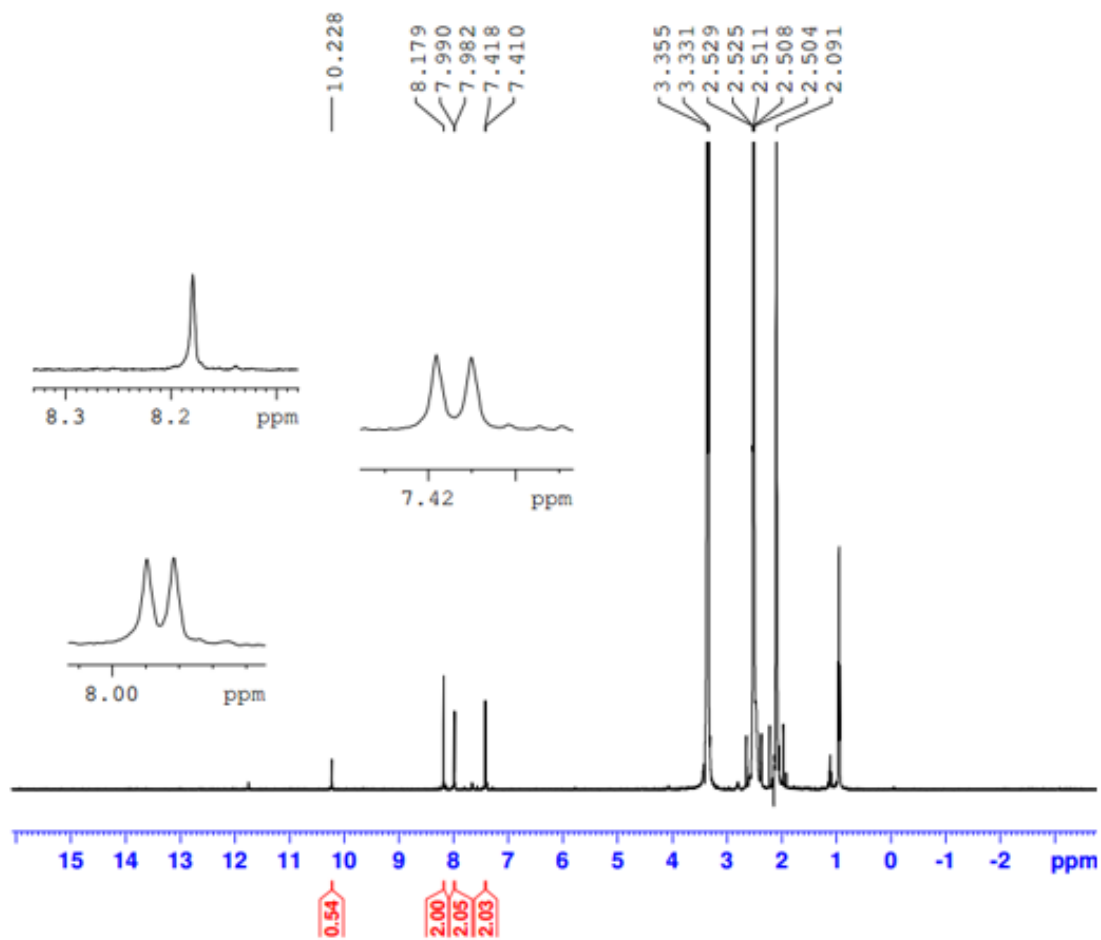


**Figure 33S.**  $^1\text{H}$ NMR of 4,7-Bis(2-bromo-5-thienyl)-2,1,3-benzothiadiazole in  $\text{DMSO-d}_6$  at 500 MHz

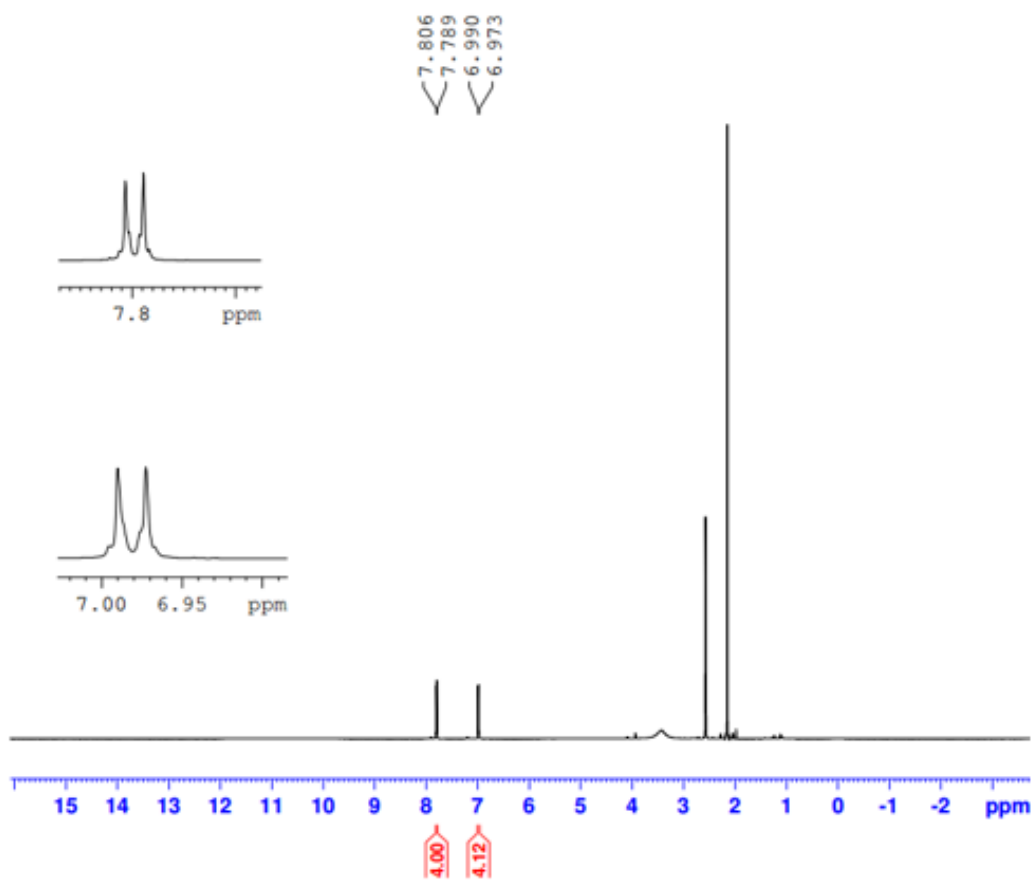


**Figure 34S.**  $^1\text{H}$ NMR of 4,4'-dihydroxybenzil in  $\text{DMSO-d}_6$  at 500 MHz

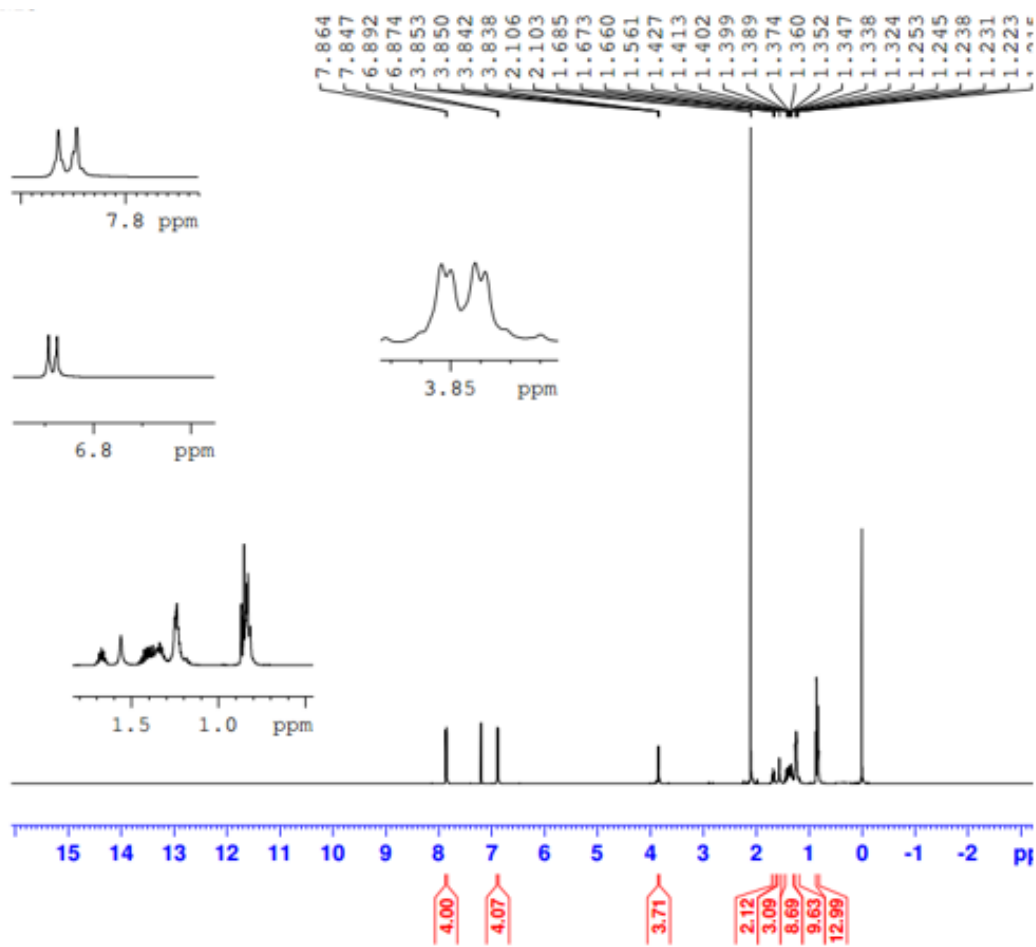


**Figure 35S.**  $^1\text{H}$ NMR of 4,4'-diethylhexylbenzil in  $\text{CDCl}_3$  at 500 MHz

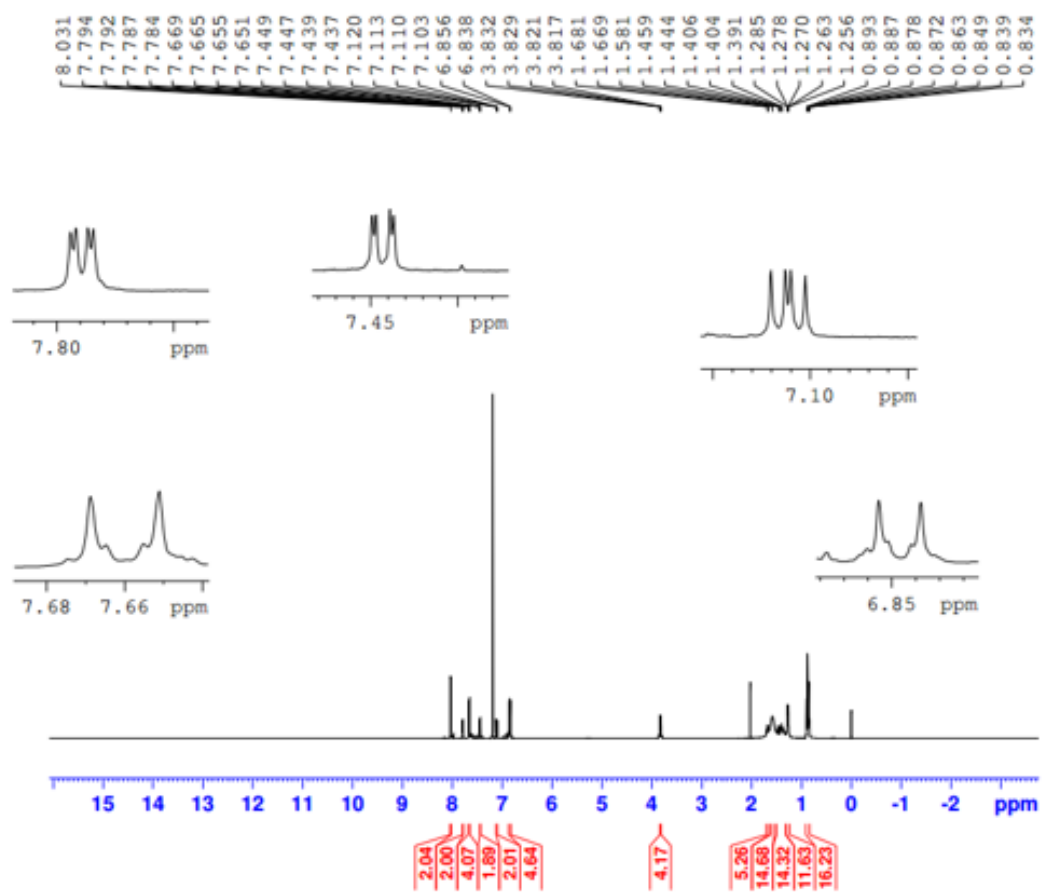


**Figure 36S.** <sup>1</sup>H NMR of 2,3-bis[4-[(2-ethylhexyl)oxy]phenyl]-5,8-di-2-thienyl-quinoxaline in CDCl<sub>3</sub> at 500 MHz

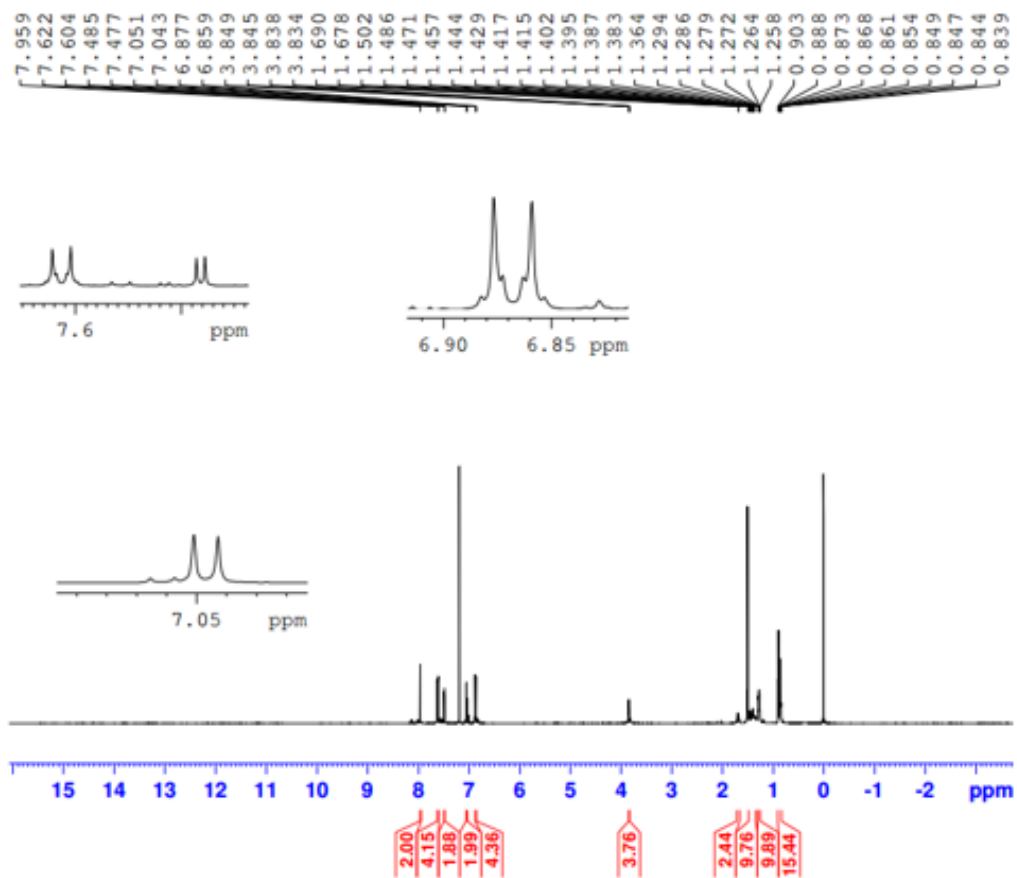


**Figure 37S.** <sup>1</sup>H NMR of 5,8-bis(5-bromo-2-thienyl)-2,3-bis[4-[(2-ethylhexyl)oxy]phenyl]-quinoxaline in CDCl<sub>3</sub> at 500 MHz

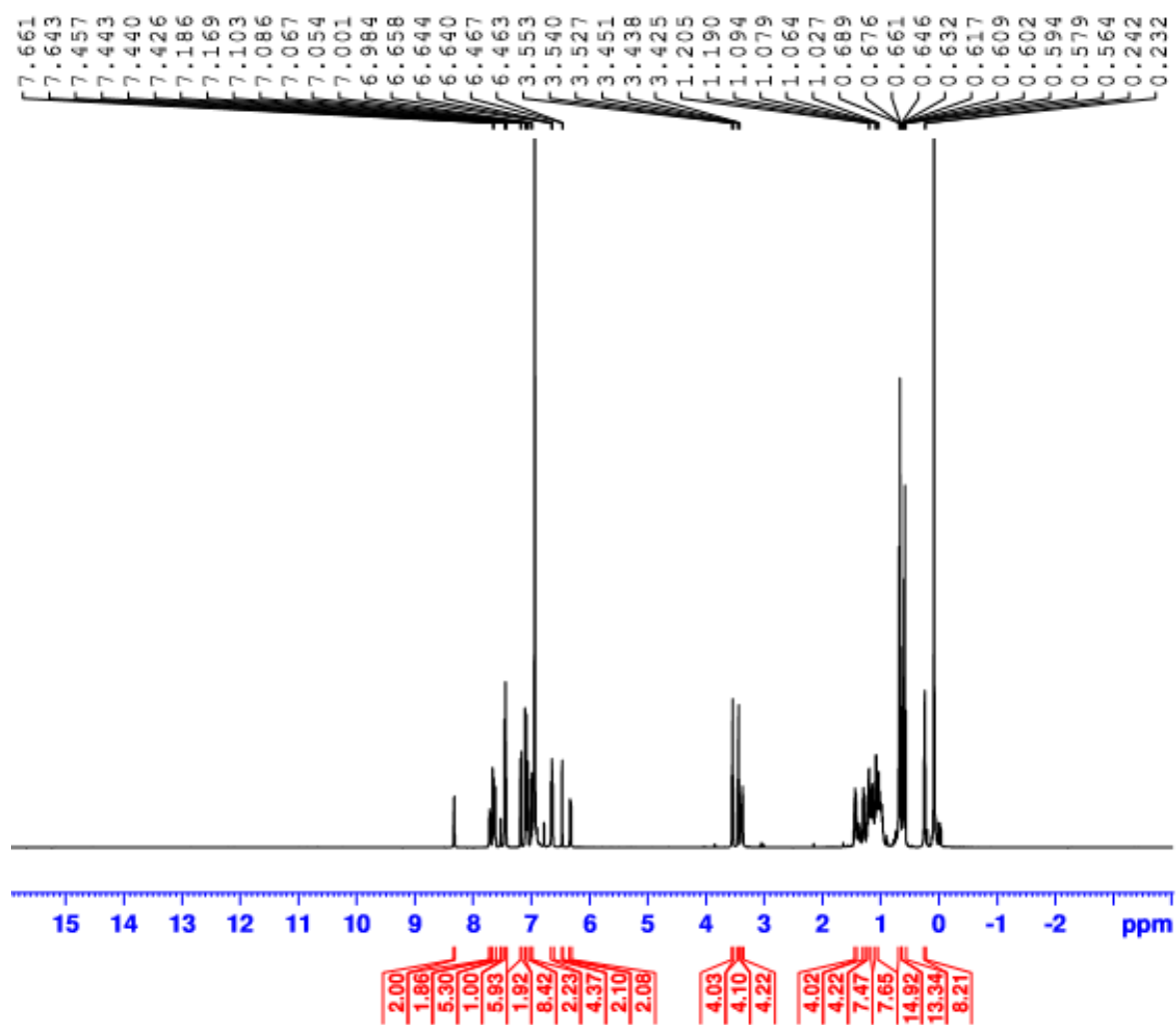
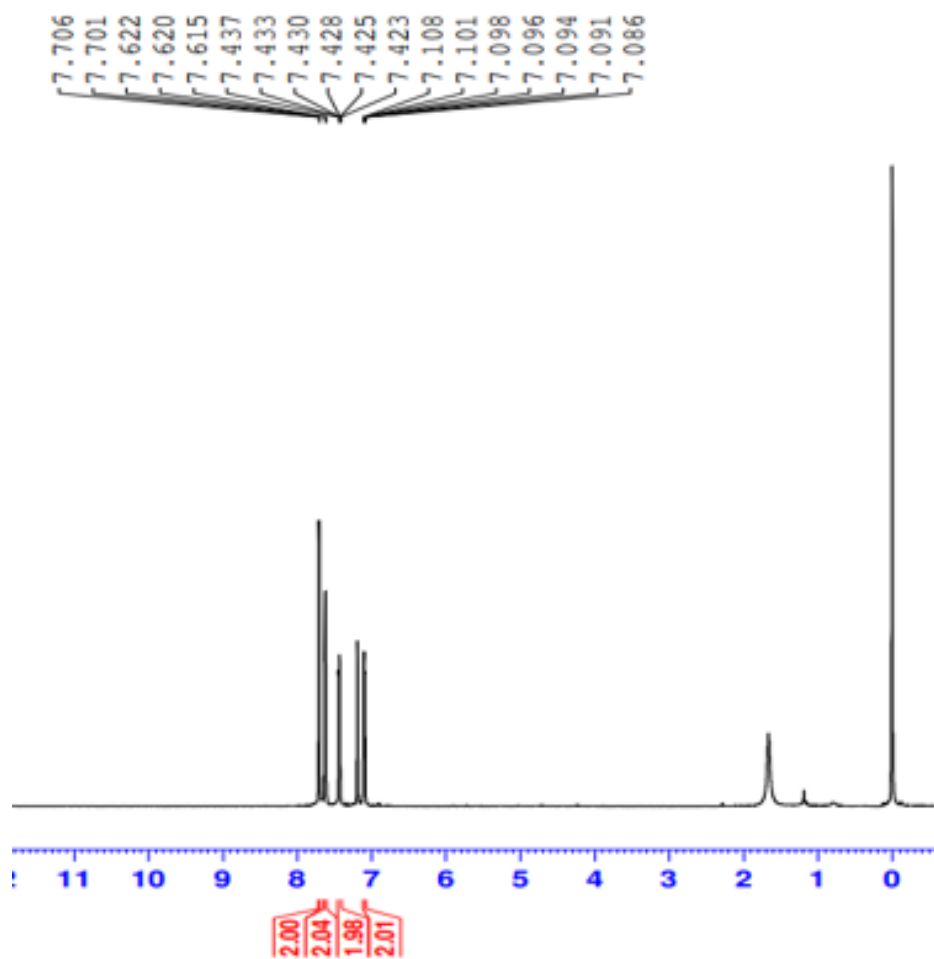
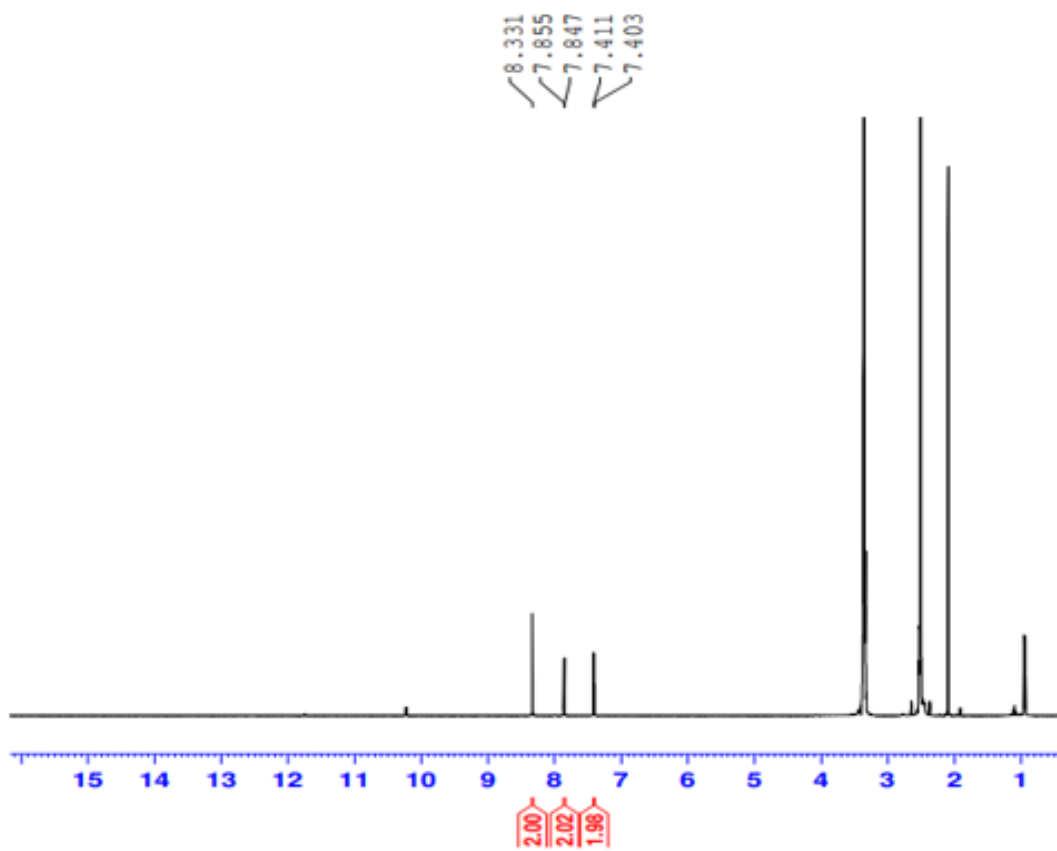


Figure 38S.  $^1\text{H}$ NMR of T200 in  $\text{C}_6\text{D}_6$  at 500 MHz





**Figure 39S.** <sup>1</sup>H NMR of 3,6-Di(thiophen-2-yl)pyridazine in CDCl<sub>3</sub> at 500 MHz



**Figure 40S.**  $^1\text{H}$ NMR of 3,6-Bis(5-bromo-2-thienyl)pyridazine in  $\text{CDCl}_3$  at 500 MHz

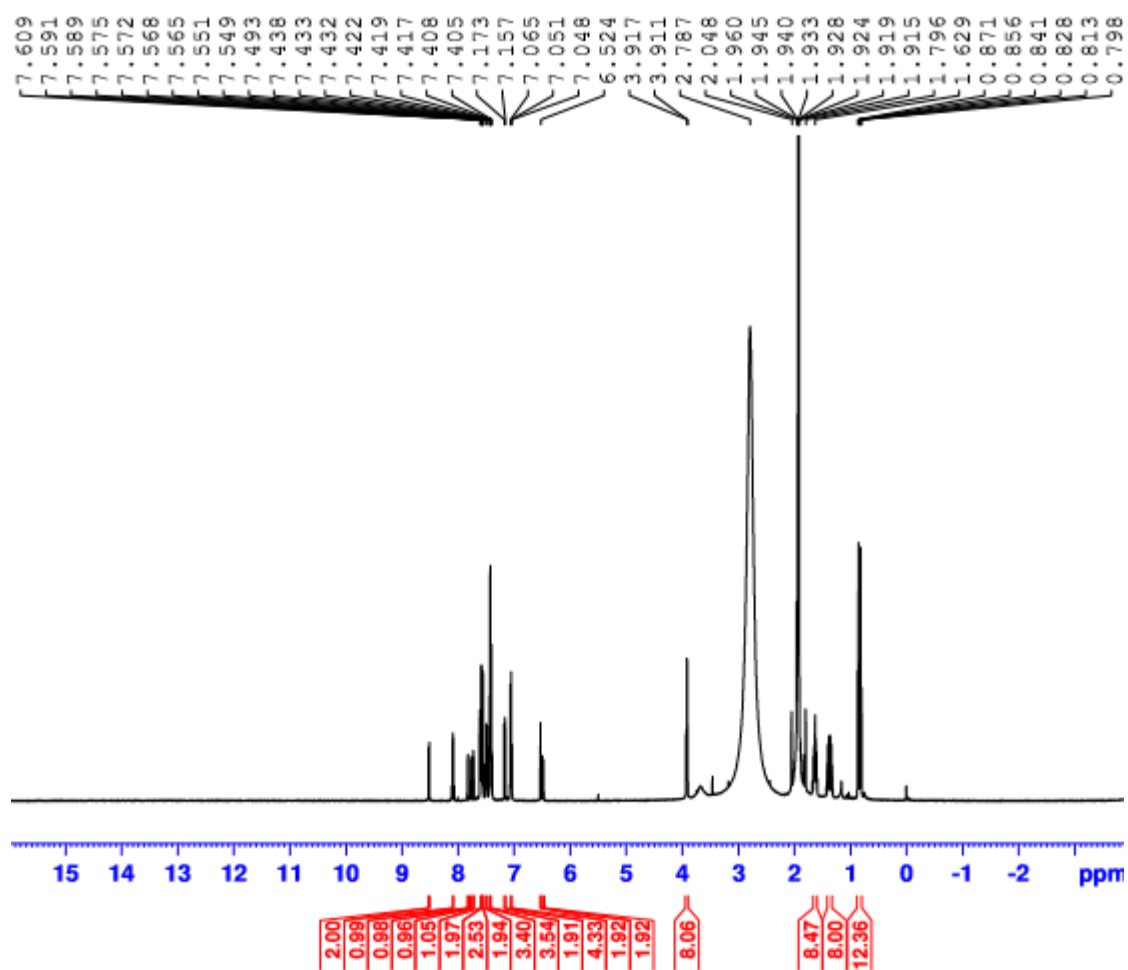


**Figure 41S.**  $^1\text{H}$ NMR of T201 in acetone- $d_6$  at 500 MHz

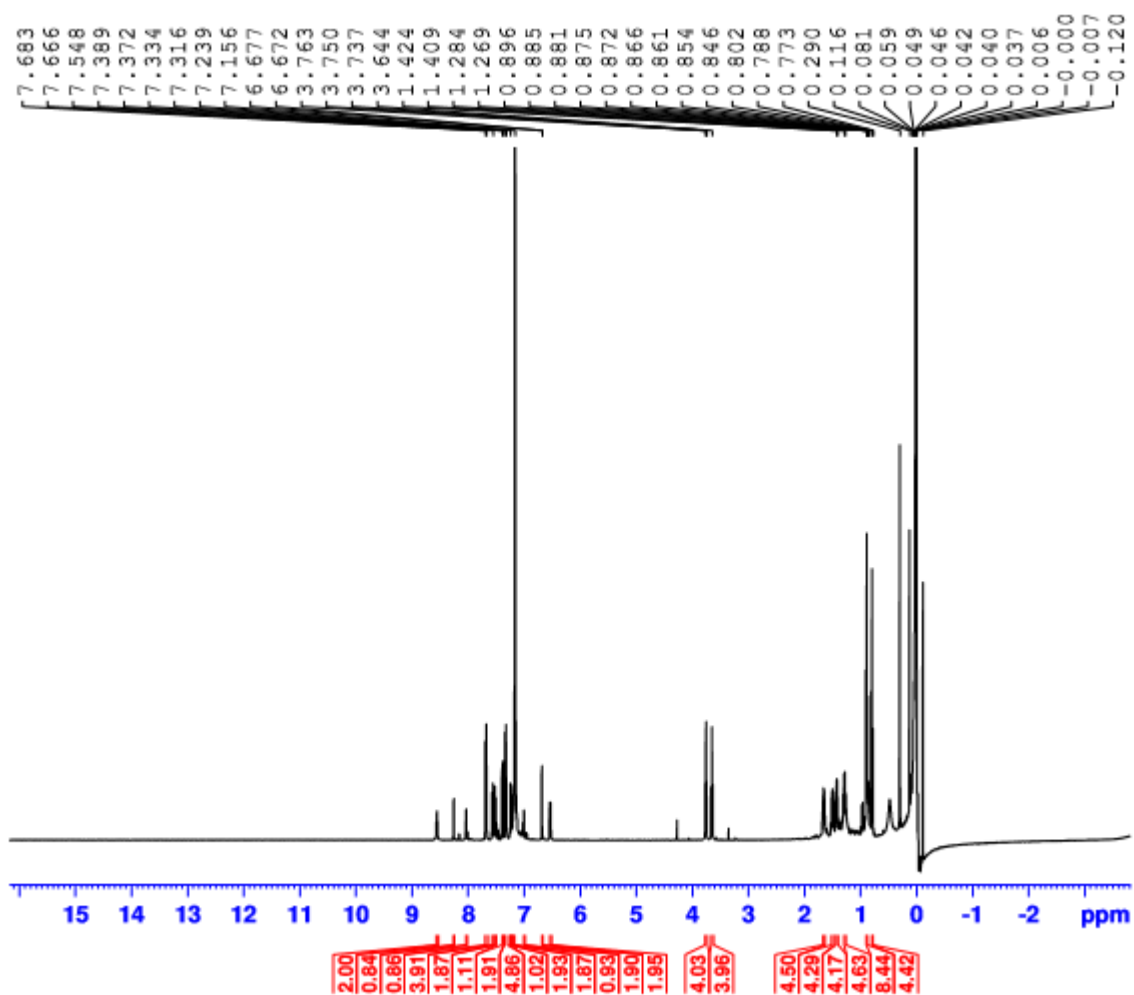


Figure 42S. <sup>1</sup>H NMR of T202 in benzene-d<sub>6</sub> at 500 MHz

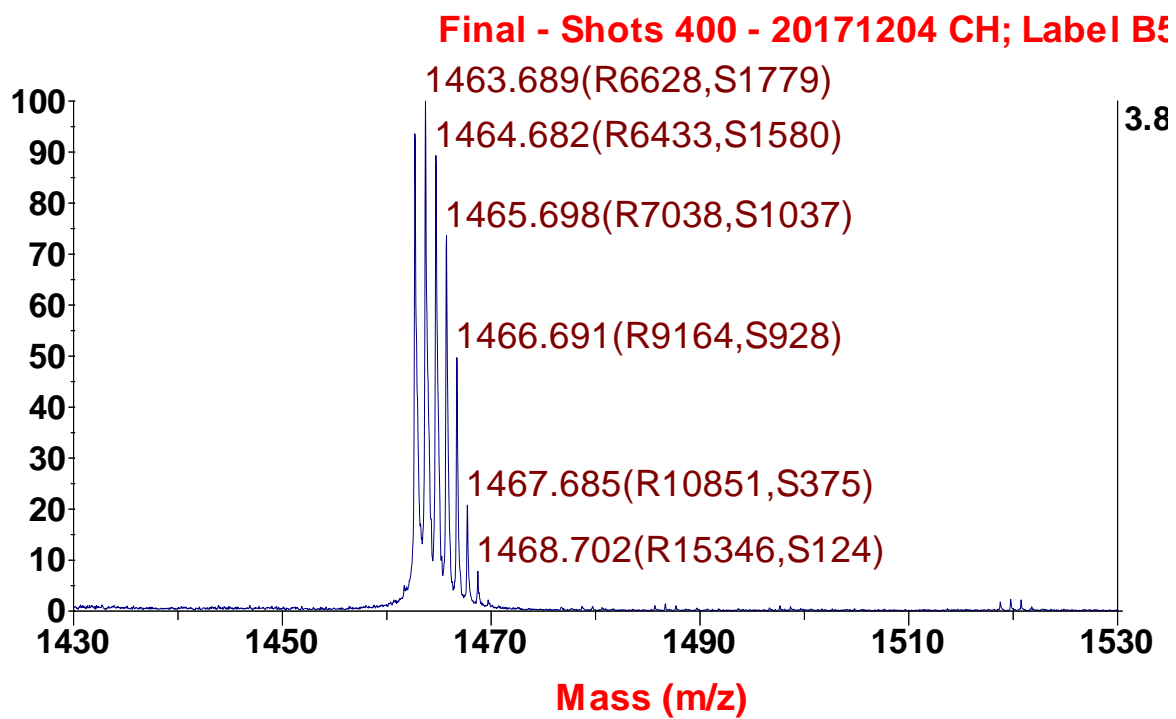


Figure 43S. Mass spectrometry of T200

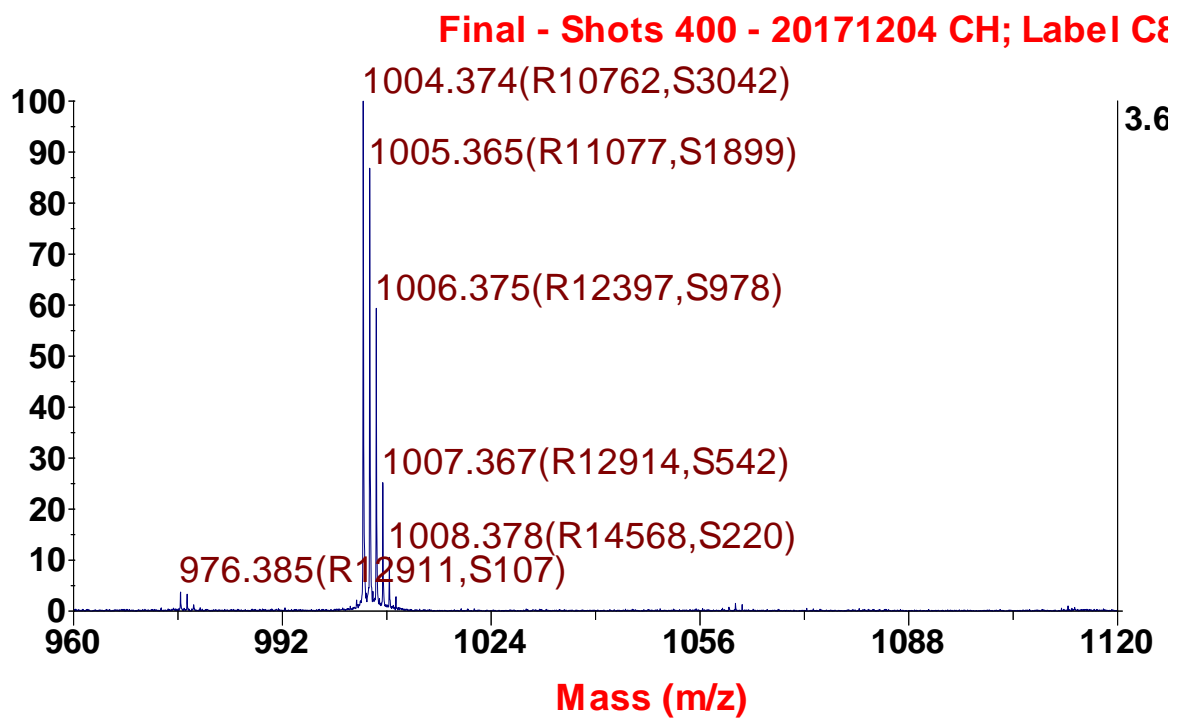


Figure 44S. Mass spectrometry of T201

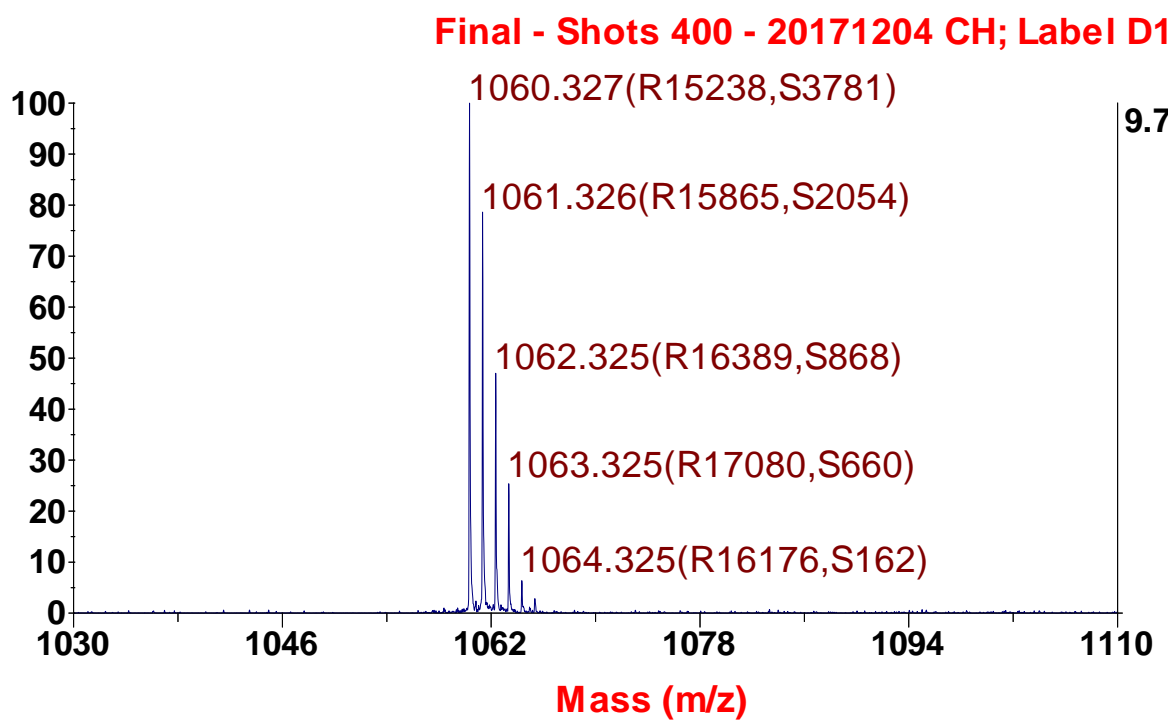


Figure 45S. Mass spectrometry of T202

## REFERENCES

1. Lewis, N. S.; Nocera, D. G., Powering the planet: Chemical challenges in solar energy utilization. *Proceedings of the National Academy of Sciences* **2006**, *103* (43), 15729-15735.
2. Ellabban, O.; Abu-Rub, H.; Blaabjerg, F., Renewable energy resources: Current status, future prospects and their enabling technology. *Renewable and Sustainable Energy Reviews* **2014**, *39*, 748-764.
3. Lund, H., Renewable energy strategies for sustainable development. *Energy* **2007**, *32* (6), 912-919.
4. Míguez, J.; López-González, L.; Sala, J.; Porteiro, J.; Granada, E.; Morán, J.; Juárez, M., Review of compliance with EU-2010 targets on renewable energy in Galicia (Spain). *Renewable and Sustainable Energy Reviews* **2006**, *10* (3), 225-247.
5. Panwar, N.; Kaushik, S.; Kothari, S., Role of renewable energy sources in environmental protection: a review. *Renewable and Sustainable Energy Reviews* **2011**, *15* (3), 1513-1524.
6. Philibert, C., The present and future use of solar thermal energy as a primary source of energy. *International Energy Agency, Paris, France* **2005**.
7. Shah, A.; Torres, P.; Tscharnner, R.; Wyrsh, N.; Keppner, H., Photovoltaic technology: the case for thin-film solar cells. *science* **1999**, *285* (5428), 692-698.
8. Chapin, D. M.; Fuller, C.; Pearson, G., A new silicon p-n junction photocell for converting solar radiation into electrical power. *Journal of Applied Physics* **1954**, *25* (5), 676-677.
9. Green, M. A.; Emery, K.; Hishikawa, Y.; Warta, W., Solar cell efficiency tables (version 37). *Progress in photovoltaics: research and applications* **2011**, *19* (1), 84-92.
10. Mortimer, R. J.; Worrall, D. R., Harnessing solar energy with Grätzel cells. **2007**.
11. Green, M. A., Third generation photovoltaics: solar cells for 2020 and beyond. *Physica E: Low-dimensional Systems and Nanostructures* **2002**, *14* (1-2), 65-70.
12. Chopra, K.; Paulson, P.; Dutta, V., Thin-film solar cells: an overview. *Progress in Photovoltaics: Research and applications* **2004**, *12* (2-3), 69-92.
13. Aberle, A. G., Thin-film solar cells. *Thin solid films* **2009**, *517* (17), 4706-4710.
14. Yan, J.; Saunders, B. R., Third-generation solar cells: a review and comparison of polymer: fullerene, hybrid polymer and perovskite solar cells. *Rsc Advances* **2014**, *4* (82), 43286-43314.
15. Gong, J.; Sumathy, K.; Qiao, Q.; Zhou, Z., Review on dye-sensitized solar cells (DSSCs): advanced techniques and research trends. *Renewable and Sustainable Energy Reviews* **2017**, *68*, 234-246.
16. O'regan, B.; Grätzel, M., A low-cost, high-efficiency solar cell based on dye-sensitized colloidal TiO<sub>2</sub> films. *Nature* **1991**, *353* (6346), 737.
17. Grätzel, M., Solar energy conversion by dye-sensitized photovoltaic cells. *Inorganic chemistry* **2005**, *44* (20), 6841-6851.



18. Nazeeruddin, M. K.; Kay, A.; Rodicio, I.; Humphry-Baker, R.; Müller, E.; Liska, P.; Vlachopoulos, N.; Grätzel, M., Conversion of light to electricity by cis-X<sub>2</sub>bis (2, 2'-bipyridyl-4, 4'-dicarboxylate) ruthenium (II) charge-transfer sensitizers (X= Cl<sup>-</sup>, Br<sup>-</sup>, I<sup>-</sup>, CN<sup>-</sup>, and SCN<sup>-</sup>) on nanocrystalline titanium dioxide electrodes. *Journal of the American Chemical Society* **1993**, *115* (14), 6382-6390.
19. Chiba, Y.; Islam, A.; Watanabe, Y.; Komiya, R.; Koide, N.; Han, L., Dye-sensitized solar cells with conversion efficiency of 11.1%. *Japanese journal of applied physics* **2006**, *45* (7L), L638.
20. Nazeeruddin, M. K.; Pechy, P.; Renouard, T.; Zakeeruddin, S. M.; Humphry-Baker, R.; Comte, P.; Liska, P.; Cevey, L.; Costa, E.; Shklover, V., Engineering of efficient panchromatic sensitizers for nanocrystalline TiO<sub>2</sub>-based solar cells. *Journal of the American Chemical Society* **2001**, *123* (8), 1613-1624.
21. Hagfeldt, A., Brief Overview of Dye-Sensitized Solar Cells. *Ambio* **2012**, *41* (Suppl 2), 151-155.
22. Kakiage, K.; Aoyama, Y.; Yano, T.; Oya, K.; Fujisawa, J.-i.; Hanaya, M., Highly-efficient dye-sensitized solar cells with collaborative sensitization by silyl-anchor and carboxy-anchor dyes. *Chemical Communications* **2015**, *51* (88), 15894-15897.
23. Wu, J.; Lan, Z.; Hao, S.; Li, P.; Lin, J.; Huang, M.; Fang, L.; Huang, Y., Progress on the electrolytes for dye-sensitized solar cells. *Pure and Applied Chemistry* **2008**, *80* (11), 2241-2258.
24. Grätzel, M., Dye-sensitized solar cells. *Journal of Photochemistry and Photobiology C: Photochemistry Reviews* **2003**, *4* (2), 145-153.
25. Grätzel, M., Photoelectrochemical cells. *Nature* **2001**, *414* (6861), 338.
26. Hagfeldt, A.; Boschloo, G.; Sun, L.; Kloo, L.; Pettersson, H., Dye-sensitized solar cells. *Chemical reviews* **2010**, *110* (11), 6595-6663.
27. Zhang, S.; Yang, X.; Numata, Y.; Han, L., Highly efficient dye-sensitized solar cells: progress and future challenges. *Energy & Environmental Science* **2013**, *6* (5), 1443-1464.
28. Nazeeruddin, M. K.; Baranoff, E.; Grätzel, M., Dye-sensitized solar cells: a brief overview. *Solar energy* **2011**, *85* (6), 1172-1178.
29. Jasim, K. E., Dye sensitized solar cells-working principles, challenges and opportunities. In *Solar Cells-Dye-Sensitized Devices*, InTech: 2011.
30. Marcus, R. A., On the theory of electron-transfer reactions. VI. Unified treatment for homogeneous and electrode reactions. *The Journal of Chemical Physics* **1965**, *43* (2), 679-701.
31. Gerischer, H.; Willig, F., Reaction of excited dye molecules at electrodes. In *Physical and Chemical Applications of Dyestuffs*, Springer: 1976; pp 31-84.
32. Hagfeldt, A.; Grätzel, M., Molecular photovoltaics. *Accounts of Chemical Research* **2000**, *33* (5), 269-277.
33. Listorti, A.; O'Regan, B.; Durrant, J. R., Electron transfer dynamics in dye-sensitized solar cells. *Chemistry of Materials* **2011**, *23* (15), 3381-3399.
34. Wang, H.; He, J.; Boschloo, G.; Lindström, H.; Hagfeldt, A.; Lindquist, S.-E., Electrochemical investigation of traps in a nanostructured TiO<sub>2</sub> film. *The Journal of Physical Chemistry B* **2001**, *105* (13), 2529-2533.

35. Cao, F.; Oskam, G.; Meyer, G. J.; Searson, P. C., Electron transport in porous nanocrystalline TiO<sub>2</sub> photoelectrochemical cells. *The Journal of Physical Chemistry* **1996**, *100* (42), 17021-17027.
36. Thompson, T. L.; Yates, J. T., Surface science studies of the photoactivation of TiO<sub>2</sub> new photochemical processes. *Chemical Reviews* **2006**, *106* (10), 4428-4453.
37. Feldt, S. M.; Lohse, P. W.; Kessler, F.; Nazeeruddin, M. K.; Grätzel, M.; Boschloo, G.; Hagfeldt, A., Regeneration and recombination kinetics in cobalt polypyridine based dye-sensitized solar cells, explained using Marcus theory. *Physical Chemistry Chemical Physics* **2013**, *15* (19), 7087-7097.
38. Upadhyaya, H. M.; Hirata, N.; Haque, S. A.; de Paoli, M.-A.; Durrant, J. R., Kinetic competition in flexible dye sensitised solar cells employing a series of polymer electrolytes. *Chemical Communications* **2006**, (8), 877-879.
39. Pelet, S.; Moser, J.-E.; Grätzel, M., Cooperative effect of adsorbed cations and iodide on the interception of back electron transfer in the dye sensitization of nanocrystalline TiO<sub>2</sub>. *The Journal of Physical Chemistry B* **2000**, *104* (8), 1791-1795.
40. Ooyama, Y.; Harima, Y., Photophysical and Electrochemical Properties, and Molecular Structures of Organic Dyes for Dye-Sensitized Solar Cells. *ChemPhysChem* **2012**, *13* (18), 4032-4080.
41. Bisquert, J.; Fabregat-Santiago, F.; Mora-Sero, I.; Garcia-Belmonte, G.; Gimenez, S., Electron lifetime in dye-sensitized solar cells: theory and interpretation of measurements. *The Journal of Physical Chemistry C* **2009**, *113* (40), 17278-17290.
42. Li, N.; Lassiter, B. E.; Lunt, R. R.; Wei, G.; Forrest, S. R., Open circuit voltage enhancement due to reduced dark current in small molecule photovoltaic cells. *Applied Physics Letters* **2009**, *94* (2), 13.
43. Macdonald, J. R., Impedance spectroscopy. *Annals of biomedical engineering* **1992**, *20* (3), 289-305.
44. Wang, Q.; Moser, J.-E.; Grätzel, M., Electrochemical impedance spectroscopic analysis of dye-sensitized solar cells. *The Journal of Physical Chemistry B* **2005**, *109* (31), 14945-14953.
45. Peng, B.; Jungmann, G.; Jäger, C.; Haarer, D.; Schmidt, H.-W.; Thelakkat, M., Systematic investigation of the role of compact TiO<sub>2</sub> layer in solid state dye-sensitized TiO<sub>2</sub> solar cells. *Coordination Chemistry Reviews* **2004**, *248* (13-14), 1479-1489.
46. Cameron, P. J.; Peter, L. M.; Zakeeruddin, S. M.; Grätzel, M., Electrochemical studies of the Co (III)/Co (II)(dbbip) 2 redox couple as a mediator for dye-sensitized nanocrystalline solar cells. *Coordination Chemistry Reviews* **2004**, *248* (13-14), 1447-1453.
47. Zhang, Z.; Ito, S.; O'Regan, B.; Kuang, D.; Zakeeruddin, S. M.; Liska, P.; Charvet, R.; Comte, P.; Nazeeruddin, M. K.; Péchy, P., The electronic role of the TiO<sub>2</sub> light-scattering layer in dye-sensitized solar cells. *Zeitschrift für physikalische chemie* **2007**, *221* (3), 319-327.
48. Ito, S.; Murakami, T. N.; Comte, P.; Liska, P.; Grätzel, C.; Nazeeruddin, M. K.; Grätzel, M., Fabrication of thin film dye sensitized solar cells with solar to electric power conversion efficiency over 10%. *Thin solid films* **2008**, *516* (14), 4613-4619.
49. Shankar, K.; Bandara, J.; Paulose, M.; Wietasch, H.; Varghese, O. K.; Mor, G. K.; LaTempa, T. J.; Thelakkat, M.; Grimes, C. A., Highly efficient solar cells using TiO<sub>2</sub> nanotube arrays sensitized with a donor-antenna dye. *Nano letters* **2008**, *8* (6), 1654-1659.

50. Kumara, G.; Deshapriya, U.; Ranasinghe, C.; Jayaweera, E.; Rajapakse, R., Efficient dye-sensitized solar cells from mesoporous zinc oxide nanostructures sensitized by N719 dye. *Journal of Semiconductors* **2018**, *39* (3), 033005.
51. Boschloo, G.; Hagfeldt, A., Characteristics of the iodide/triiodide redox mediator in dye-sensitized solar cells. *Accounts of chemical research* **2009**, *42* (11), 1819-1826.
52. Yella, A.; Lee, H.-W.; Tsao, H. N.; Yi, C.; Chandiran, A. K.; Nazeeruddin, M. K.; Diau, E. W.-G.; Yeh, C.-Y.; Zakeeruddin, S. M.; Grätzel, M., Porphyrin-sensitized solar cells with cobalt (II/III)-based redox electrolyte exceed 12 percent efficiency. *Science* **2011**, *334* (6056), 629-634.
53. Hamann, T. W.; Brunschwig, B. S.; Lewis, N. S., Comparison of the self-exchange and interfacial charge-transfer rate constants for methyl-versus tert-butyl-substituted Os (III) polypyridyl complexes. *The Journal of Physical Chemistry B* **2006**, *110* (50), 25514-25520.
54. Feldt, S. M.; Gibson, E. A.; Gabrielsson, E.; Sun, L.; Boschloo, G.; Hagfeldt, A., Design of organic dyes and cobalt polypyridine redox mediators for high-efficiency dye-sensitized solar cells. *Journal of the American Chemical Society* **2010**, *132* (46), 16714-16724.
55. Mathew, S.; Yella, A.; Gao, P.; Humphry-Baker, R.; Curchod, B. F.; Ashari-Astani, N.; Tavernelli, I.; Rothlisberger, U.; Nazeeruddin, M. K.; Grätzel, M., Dye-sensitized solar cells with 13% efficiency achieved through the molecular engineering of porphyrin sensitizers. *Nature chemistry* **2014**, *6* (3), 242-7.
56. Nelson, J. J.; Amick, T. J.; Elliott, C. M., Mass transport of polypyridyl cobalt complexes in dye-sensitized solar cells with mesoporous TiO<sub>2</sub> photoanodes. *The Journal of Physical Chemistry C* **2008**, *112* (46), 18255-18263.
57. Nusbaumer, H.; Zakeeruddin, S. M.; Moser, J. E.; Grätzel, M., An Alternative Efficient Redox Couple for the Dye-Sensitized Solar Cell System. *Chemistry—A European Journal* **2003**, *9* (16), 3756-3763.
58. Bai, Y.; Yu, Q.; Cai, N.; Wang, Y.; Zhang, M.; Wang, P., High-efficiency organic dye-sensitized mesoscopic solar cells with a copper redox shuttle. *Chemical Communications* **2011**, *47* (15), 4376-4378.
59. Daeneke, T.; Kwon, T.-H.; Holmes, A. B.; Duffy, N. W.; Bach, U.; Spiccia, L., High-efficiency dye-sensitized solar cells with ferrocene-based electrolytes. *Nature chemistry* **2011**, *3* (3), 211.
60. Wu, J.; Lan, Z.; Lin, J.; Huang, M.; Huang, Y.; Fan, L.; Luo, G., Electrolytes in dye-sensitized solar cells. *Chemical reviews* **2015**, *115* (5), 2136-2173.
61. Tributsch, H., Dye sensitization solar cells: a critical assessment of the learning curve. *Coordination Chemistry Reviews* **2004**, *248* (13-14), 1511-1530.
62. Hara, K.; Horiguchi, T.; Kinoshita, T.; Sayama, K.; Arakawa, H., Influence of electrolytes on the photovoltaic performance of organic dye-sensitized nanocrystalline TiO<sub>2</sub> solar cells. *Solar Energy Materials and Solar Cells* **2001**, *70* (2), 151-161.
63. Fukui, A.; Komiya, R.; Yamanaka, R.; Islam, A.; Han, L., Effect of a redox electrolyte in mixed solvents on the photovoltaic performance of a dye-sensitized solar cell. *Solar Energy Materials and Solar Cells* **2006**, *90* (5), 649-658.

64. Huang, S.; Schlichthörl, G.; Nozik, A.; Grätzel, M.; Frank, A., Charge recombination in dye-sensitized nanocrystalline TiO<sub>2</sub> solar cells. *The Journal of Physical Chemistry B* **1997**, *101* (14), 2576-2582.
65. Schlichthörl, G.; Huang, S.; Sprague, J.; Frank, A., Band edge movement and recombination kinetics in dye-sensitized nanocrystalline TiO<sub>2</sub> solar cells: a study by intensity modulated photovoltage spectroscopy. *The Journal of Physical Chemistry B* **1997**, *101* (41), 8141-8155.
66. Wang, Z.-S.; Cui, Y.; Dan-oh, Y.; Kasada, C.; Shinpo, A.; Hara, K., Thiophene-functionalized coumarin dye for efficient dye-sensitized solar cells: electron lifetime improved by coadsorption of deoxycholic acid. *The Journal of Physical Chemistry C* **2007**, *111* (19), 7224-7230.
67. Liu, Y.; Hagfeldt, A.; Xiao, X.-R.; Lindquist, S.-E., Investigation of influence of redox species on the interfacial energetics of a dye-sensitized nanoporous TiO<sub>2</sub> solar cell. *Solar Energy Materials and Solar Cells* **1998**, *55* (3), 267-281.
68. Kambe, S.; Nakade, S.; Kitamura, T.; Wada, Y.; Yanagida, S., Influence of the electrolytes on electron transport in mesoporous TiO<sub>2</sub>- electrolyte systems. *The Journal of Physical Chemistry B* **2002**, *106* (11), 2967-2972.
69. Grätzel, M., Conversion of sunlight to electric power by nanocrystalline dye-sensitized solar cells. *Journal of Photochemistry and Photobiology A: Chemistry* **2004**, *164* (1-3), 3-14.
70. Zhang, C.; Huang, Y.; Huo, Z.; Chen, S.; Dai, S., Photoelectrochemical effects of guanidinium thiocyanate on dye-sensitized solar cell performance and stability. *The Journal of Physical Chemistry C* **2009**, *113* (52), 21779-21783.
71. Haque, S. A.; Palomares, E.; Cho, B. M.; Green, A. N.; Hirata, N.; Klug, D. R.; Durrant, J. R., Charge separation versus recombination in dye-sensitized nanocrystalline solar cells: the minimization of kinetic redundancy. *Journal of the American Chemical Society* **2005**, *127* (10), 3456-3462.
72. Hauch, A.; Georg, A., Diffusion in the electrolyte and charge-transfer reaction at the platinum electrode in dye-sensitized solar cells. *Electrochimica Acta* **2001**, *46* (22), 3457-3466.
73. Thomas, S.; Deepak, T.; Anjusree, G.; Arun, T.; Nair, S. V.; Nair, A. S., A review on counter electrode materials in dye-sensitized solar cells. *Journal of Materials Chemistry A* **2014**, *2* (13), 4474-4490.
74. Papageorgiou, N.; Maier, W.; Grätzel, M., An iodine/triiodide reduction electrocatalyst for aqueous and organic media. *Journal of the electrochemical Society* **1997**, *144* (3), 876-884.
75. Kay, A.; Grätzel, M., Low cost photovoltaic modules based on dye sensitized nanocrystalline titanium dioxide and carbon powder. *Solar Energy Materials and Solar Cells* **1996**, *44* (1), 99-117.
76. Ahmad, S.; Bessho, T.; Kessler, F.; Baranoff, E.; Frey, J.; Yi, C.; Grätzel, M.; Nazeeruddin, M. K., A new generation of platinum and iodine free efficient dye-sensitized solar cells. *Physical Chemistry Chemical Physics* **2012**, *14* (30), 10631-10639.
77. Wang, M.; Anghel, A. M.; Marsan, B.; Cevey Ha, N.-L.; Pootrakulchote, N.; Zakeeruddin, S. M.; Grätzel, M., CoS supersedes Pt as efficient electrocatalyst for triiodide

- reduction in dye-sensitized solar cells. *Journal of the American Chemical Society* **2009**, *131* (44), 15976-15977.
78. Nazeeruddin, M. K.; Zakeeruddin, S.; Humphry-Baker, R.; Jirousek, M.; Liska, P.; Vlachopoulos, N.; Shklover, V.; Fischer, C.-H.; Grätzel, M., Acid– Base equilibria of (2, 2'-Bipyridyl-4, 4'-dicarboxylic acid) ruthenium (II) complexes and the effect of protonation on charge-transfer sensitization of nanocrystalline titania. *Inorganic Chemistry* **1999**, *38* (26), 6298-6305.
79. Mishra, A.; Fischer, M. K.; Bäuerle, P., Metal-free organic dyes for dye-sensitized solar cells: From structure: Property relationships to design rules. *Angewandte Chemie International Edition* **2009**, *48* (14), 2474-2499.
80. Liang, M.; Chen, J., Arylamine organic dyes for dye-sensitized solar cells. *Chemical Society Reviews* **2013**, *42* (8), 3453-3488.
81. Hagberg, D. P.; Jiang, X.; Gabrielsson, E.; Linder, M.; Marinado, T.; Brinck, T.; Hagfeldt, A.; Sun, L., Symmetric and unsymmetric donor functionalization. comparing structural and spectral benefits of chromophores for dye-sensitized solar cells. *Journal of Materials Chemistry* **2009**, *19* (39), 7232-7238.
82. Liang, M.; Xu, W.; Cai, F.; Chen, P.; Peng, B.; Chen, J.; Li, Z., New triphenylamine-based organic dyes for efficient dye-sensitized solar cells. *The Journal of Physical Chemistry C* **2007**, *111* (11), 4465-4472.
83. Kalyanasundaram, K.; Grätzel, M., Applications of functionalized transition metal complexes in photonic and optoelectronic devices. *Coordination chemistry reviews* **1998**, *177* (1), 347-414.
84. Chen, C.; Yang, X.; Cheng, M.; Zhang, F.; Sun, L., Degradation of Cyanoacrylic Acid-Based Organic Sensitizers in Dye-Sensitized Solar Cells. *ChemSusChem* **2013**, *6* (7), 1270-1275.
85. Zietz, B.; Gabrielsson, E.; Johansson, V.; El-Zohry, A. M.; Sun, L.; Kloo, L., Photoisomerization of the cyanoacrylic acid acceptor group—a potential problem for organic dyes in solar cells. *Physical Chemistry Chemical Physics* **2014**, *16* (6), 2251-2255.
86. Ooyama, Y.; Inoue, S.; Nagano, T.; Kushimoto, K.; Ohshita, J.; Imae, I.; Komaguchi, K.; Harima, Y., Dye-Sensitized Solar Cells Based On Donor–Acceptor  $\pi$ -Conjugated Fluorescent Dyes with a Pyridine Ring as an Electron-Withdrawing Anchoring Group. *Angewandte Chemie International Edition* **2011**, *50* (32), 7429-7433.
87. Ooyama, Y.; Yamaguchi, N.; Imae, I.; Komaguchi, K.; Ohshita, J.; Harima, Y., Dye-sensitized solar cells based on D– $\pi$ –A fluorescent dyes with two pyridyl groups as an electron-withdrawing–injecting anchoring group. *Chemical Communications* **2013**, *49* (25), 2548-2550.
88. Mai, C.-L.; Moehl, T.; Hsieh, C.-H.; Décoppet, J.-D.; Zakeeruddin, S. M.; Grätzel, M.; Yeh, C.-Y., Porphyrin sensitizers bearing a pyridine-type anchoring group for dye-sensitized solar cells. *ACS applied materials & interfaces* **2015**, *7* (27), 14975-14982.
89. Zhang, L.; Cole, J. M., Anchoring groups for dye-sensitized solar cells. *ACS applied materials & interfaces* **2015**, *7* (6), 3427-3455.
90. Wang, L.; Yang, X.; Li, S.; Cheng, M.; Sun, L., A new type of organic sensitizers with pyridine-N-oxide as the anchoring group for dye-sensitized solar cells. *RSC Advances* **2013**, *3* (33), 13677-13680.

91. McNamara, W. R.; Snoeberger III, R. C.; Li, G.; Richter, C.; Allen, L. J.; Milot, R. L.; Schmuttenmaer, C. A.; Crabtree, R. H.; Brudvig, G. W.; Batista, V. S., Hydroxamate anchors for water-stable attachment to TiO<sub>2</sub> nanoparticles. *Energy & Environmental Science* **2009**, 2 (11), 1173-1175.
92. Zhang, L.; Cole, J. M.; Dai, C., Variation in optoelectronic properties of azo dye-sensitized TiO<sub>2</sub> semiconductor interfaces with different adsorption anchors: carboxylate, sulfonate, hydroxyl and pyridyl groups. *ACS applied materials & interfaces* **2014**, 6 (10), 7535-7546.
93. Ogura, R. Y.; Nakane, S.; Morooka, M.; Orihashi, M.; Suzuki, Y.; Noda, K., High-performance dye-sensitized solar cell with a multiple dye system. *Applied Physics Letters* **2009**, 94 (7), 54.
94. Shibayama, N.; Ozawa, H.; Abe, M.; Ooyama, Y.; Arakawa, H., A new cosensitization method using the Lewis acid sites of a TiO<sub>2</sub> photoelectrode for dye-sensitized solar cells. *Chemical Communications* **2014**, 50 (48), 6398-6401.
95. Ooyama, Y.; Uenaka, K.; Sato, T.; Shibayama, N.; Ohshita, J., Effective co-sensitization using D- $\pi$ -A dyes with a pyridyl group adsorbing at Brønsted acid sites and Lewis acid sites on a TiO<sub>2</sub> surface for dye-sensitized solar cells. *RSC Advances* **2015**, 5 (4), 2531-2535.
96. Ooyama, Y.; Uenaka, K.; Kanda, M.; Yamada, T.; Shibayama, N.; Ohshita, J., A new co-sensitization method employing D- $\pi$ -A dye with pyridyl group and D- $\pi$ -Cat dye with catechol unit for dye-sensitized solar cells. *Dyes and Pigments* **2015**, 122, 40-45.
97. Jia, H.-L.; Zhang, M.-D.; Ju, Z.-M.; Zheng, H.-G.; Ju, X.-H., Picolinic acid as an efficient tridentate anchoring group adsorbing at Lewis acid sites and Brønsted acid sites of the TiO<sub>2</sub> surface in dye-sensitized solar cells. *Journal of Materials Chemistry A* **2015**, 3 (28), 14809-14816.
98. Wang, Z.; Fang, Y.; Tao, X.; Wang, Y.; Quan, Y.; Zhang, S.; Cheng, Y., Deep red aggregation-induced CPL emission behavior of four-component tunable AIE-active chiral polymers via two FRET pairs mechanism. *Polymer* **2017**, 130, 61-67.
99. Amininasab, S. M.; Esmaili, S.; Taghavi, M.; Shami, Z., Fabrication and characterization of novel high-performance fluorinated polyimides with xanthene pendent architecture: Study of thermal, photophysical, antibacterial and heavy metal ion adsorption behavior. *Journal of Fluorine Chemistry* **2016**, 192, 48-57.
100. Bui, T.-T.; Garreau-de Bonneval, B.; Ching, K. I. M.-C., Synthesis and preliminary physical properties of new neutral tetraalkoxy-substituted nickel bis (1, 2-dithiolene) complexes. *New Journal of Chemistry* **2010**, 34 (2), 337-347.
101. Zhang, L.-P.; Jiang, K.-J.; Li, G.; Zhang, Q.-Q.; Yang, L.-M., Pyrazino [2, 3-g] quinoxaline dyes for solar cell applications. *Journal of Materials Chemistry A* **2014**, 2 (36), 14852-14857.
102. Wang, M.; Ma, D.; Shi, K.; Shi, S.; Chen, S.; Huang, C.; Qiao, Z.; Zhang, Z.-G.; Li, Y.; Li, X., The role of conjugated side chains in high performance photovoltaic polymers. *Journal of Materials Chemistry A* **2015**, 3 (6), 2802-2814.
103. Wang, W.; Meng, W.; Du, H., B (C 6 F 5) 3-catalyzed metal-free hydrogenation of 3, 6-diarylpyridazines. *Dalton Transactions* **2016**, 45 (14), 5945-5948.

104. Qin, H.-m.; Shi, W.; Rukiya, M.; Han, Y.; Li, W.-l.; Ismayil, N., Synthesis and characterization of dithiophene-pyridazine-containing poly(aryleneethynylene) derivatives. *Gongneng Cailiao* **2010**, *41* (8), 1406-1409, 1413.
105. Murto, P.; Tang, S.; Larsen, C.; Xu, X.; Sandström, A.; Pietarinen, J.; Bagemihl, B.; Abdulahi, B. A.; Mammo, W.; Andersson, M. R., Incorporation of Designed Donor–Acceptor–Donor Segments in a Host Polymer for Strong Near-Infrared Emission from a Large-Area Light-Emitting Electrochemical Cell. *ACS Applied Energy Materials* **2018**, *1* (4), 1753-1761.
106. Hilal, H. M.; El Bitar Nehme, M. A.; Ghaddar, T. H., Large Enhancement of Dye Sensitized Solar Cell Efficiency by co-Sensitizing Pyridyl-with Carboxylic Acid-based Dyes. *ACS Applied Energy Materials* **2018**.
107. Su, J.; Zhu, S.; Chen, R.; An, Z.; Chen, X.; Chen, P., Study on dye-loading mode on TiO<sub>2</sub> films and impact of co-sensitizers on highly efficient co-sensitized solar cells. *Journal of Materials Science: Materials in Electronics* **2017**, *28* (5), 3962-3969.
108. Mosconi, E.; Yum, J.-H.; Kessler, F.; Gómez García, C. J.; Zuccaccia, C.; Cinti, A.; Nazeeruddin, M. K.; Grätzel, M.; De Angelis, F., Cobalt electrolyte/dye interactions in dye-sensitized solar cells: a combined computational and experimental study. *Journal of the American Chemical Society* **2012**, *134* (47), 19438-19453.
109. Pazoki, M.; Lohse, P. W.; Taghavinia, N.; Hagfeldt, A.; Boschloo, G., The effect of dye coverage on the performance of dye-sensitized solar cells with a cobalt-based electrolyte. *Phys Chem Chem Phys* **2014**, *16* (18), 8503-8.